

Dissertation
submitted to the
Combined Faculties for the Natural Sciences and for
Mathematics
of the Ruperto-Carola University of Heidelberg, Germany
for the degree of
Doctor of Natural Sciences

Put forward by

Diplom-Physiker Patrick Hoyer
Born in Weiden i. d. OPf.

Oral examination: December 17, 2014

RESOLFT Light-sheet Microscopy

Referees:

Prof. Dr. Stefan W. Hell

Prof. Dr. Wolfgang Petrich

«φύσις κρύπτεσθαι φιλεῖ.»

(“*Nature loves to hide.*”)

Heraklit, Fragmentum, B 123.

Abstract

The concept of RESOLFT was introduced to break the resolution limit in fluorescence microscopy, which is set by the physical phenomenon of diffraction. It enables the separation of fluorophores inside a focal volume by driving reversible optical transitions between two discernible states. The family of reversibly switchable fluorescent proteins (RSFPs) with long-lived on- and off-states allows for RESOLFT imaging at low light levels. Up to now, RESOLFT involving RSFPs as fluorescent markers has been exclusively demonstrated to enhance the resolution in the lateral dimension. In this work, a novel RSFP-based RESOLFT microscope is presented, that, for the first time, breaks the diffraction barrier in the axial direction by switching fluorophores in the volume of a light-sheet. It is realized with the optical arrangement of a selective plane illumination microscope (SPIM), that illuminates only a thin section of a sample perpendicular to the detection axis and thus reduces the overall light exposure in volume recordings. The symbiotic combination of RSFP-based RESOLFT and SPIM, the so called RESOLFT-SPIM nanoscope, offers highly parallelized, fast imaging of living biological specimens with low light doses and sub-diffraction axial resolution. Compared to the diffraction-limited SPIM analogue an improvement in axial resolution by more than a factor of 12 is demonstrated.

Zusammenfassung

Das RESOLFT Konzept wurde entwickelt, um die physikalische Grenze der Auflösung in der Fluoreszenzmikroskopie zu überwinden. Es ermöglicht die Trennung von Fluoreszenzfarbstoffen in einem beugungsbegrenzten Volumen durch reversible licht-induzierte Übergänge zwischen unterscheidbaren Zuständen. Reversibel schaltbare fluoreszente Proteine (RSFPs) mit langlebigen An- und Aus-Zuständen erlauben RESOLFT Aufnahmen bei geringen Lichtintensitäten. Bisher haben RESOLFT Mikroskope, die RSFPs als Fluoreszenzmarker verwenden, ausschließlich die laterale Auflösung erhöht. In dieser Arbeit wird nun zum ersten Mal ein RSFP-basiertes RESOLFT Mikroskop gezeigt, das eine axiale Auflösung unterhalb der Beugungsgrenze erzielt, indem Farbstoffe im Volumen eines Lichtblatts an- und ausgeschaltet werden. Es besitzt die optische Anordnung eines SPIM Mikroskops, das nur dünne Schnitte einer Probe senkrecht zur Detektionsachse beleuchtet und dadurch die Gesamtlichtdosis bei Aufnahmen eines Volumens reduziert. Die

Kombination eines RSFP-basierten RESOLFT Nanoskops mit einem Lichtblatt-Mikroskop, im Folgenden RESOLFT-SPIM genannt, bietet hochgradig parallelisierte schnelle Aufnahmen von lebenden biologischen Proben mit geringer Lichtdosis und einer axialen Auflösung unterhalb der Beugungsgrenze. RESOLFT-SPIM ermöglicht eine 12-fache Verbesserung der axialen Auflösung im Vergleich zu einem beugungsbegrenzten SPIM.

Contents

List of Figures	xi
List of Acronyms	xiii
1 Introduction	1
2 Far-field fluorescence microscopy	5
2.1 Fluorescence and labeling	5
2.1.1 Basics of fluorescence	6
2.1.2 Fluorescent labels	9
2.2 Wide-field microscopy	12
2.2.1 Imaging with a lens	14
2.2.2 Resolution of wide-field microscopes	16
2.3 Confocal microscopy	17
2.4 Light-sheet fluorescence microscopy	19
2.4.1 The use of light-sheets in light microscopy	21
2.4.2 Selective plane illumination microscopy (SPIM)	22
2.5 Optical nanoscopy	26
2.5.1 The concept of breaking the diffraction barrier	27
2.5.2 Single marker switching techniques	27
2.5.3 RESOLFT techniques	28
3 RESOLFT-SPIM	37
3.1 Basic concept	37
3.2 Optical implementation	39
3.2.1 Optical layout	39
3.2.2 Hardware control	47
3.2.3 Alignment strategies	48
3.3 RESOLFT-SPIM imaging	52
3.3.1 Imaging strategy	53
3.3.2 Image representation	54
3.4 Characterization of the setup	57
3.4.1 Light-sheet parameters	57
3.4.2 Quality of the zero-intensity region	60
3.4.3 Resolving power	61
3.4.4 Validation of the square root law	65
3.4.5 Rayleigh range of the RESOLFT light-sheet	66
3.4.6 Resolution in a dense sample	68
3.5 Biological applications	70
3.5.1 HIV-1 assembly in living HeLa cells	70

3.5.2	Nuclear pore complexes of living U2OS cells	72
3.5.3	Cytoskeleton of living HeLa cells	75
4	Summary and discussion	79
5	Outlook	83
A	Appendix	85
A.1	Afterglow effect	85
A.2	Sample preparation	86
A.3	HIV-1 enclosing rsEGFP2	89
A.4	Imaging media for RESOLFT-SPIM	90
	Bibliography	91

List of Figures

Figure 2.1	Jablonski diagram	6
Figure 2.2	Fluorescence absorption and emission spectra of EGFP and mCherry	8
Figure 2.3	Schematic drawing of a wide-field microscope	13
Figure 2.4	The concept of image formation with a lens and the Rayleigh criterion	14
Figure 2.5	Simulated convolution of an object with a point spread function (PSF)	16
Figure 2.6	Schematic drawing of a confocal microscope	18
Figure 2.7	Schematic drawing of a fluorescence light-sheet microscope	20
Figure 2.8	Sketch of a light-sheet and its dimensions	24
Figure 2.9	RESOLFT phase plates and the resulting light intensity pattern	30
Figure 2.10	Two-state model with a signaling state <i>A</i> and a non-signaling state <i>B</i>	33
Figure 3.1	The RESOLFT-SPIM concept	38
Figure 3.2	Diagram of the RESOLFT-SPIM setup	40
Figure 3.3	Mounting and positioning of the half-moon phase plate	42
Figure 3.4	Possible combinations of objective lenses for RESOLFT-SPIM	43
Figure 3.5	Monolithic objective mount unit for RESOLFT-SPIM	44
Figure 3.6	Specimen chamber for RESOLFT-SPIM	46
Figure 3.7	Block diagram of the hardware in the RESOLFT-SPIM setup	48
Figure 3.8	Tool for collinearity alignment of RESOLFT-SPIM lasers	49
Figure 3.9	Tool for the alignment of light-sheets to the focal plane of detection	51
Figure 3.10	Light-sheet alignment to the FOV of detection	52
Figure 3.11	Signal sequence for RESOLFT-SPIM images	54
Figure 3.12	Representation of RESOLFT-SPIM images	55
Figure 3.13	Measurement of light-sheet parameters	58
Figure 3.14	Measurement of the system's PSF and analysis of the zero-intensity region	60
Figure 3.15	The resolving power of RESOLFT-SPIM measured on single HIV-1 particles.	62

Figure 3.16	Distribution of axial and lateral FWHMs of Gaussian fits to HIV-1 particles imaged in RESOLFT-SPIM and conventional SPIM mode.	64
Figure 3.17	Validation of the square root law in RESOLFT-SPIM . . .	65
Figure 3.18	The Rayleigh range of the RESOLFT light-sheet measured on HIV-1 particles.	67
Figure 3.19	Resolving power of RESOLFT-SPIM in a dense sample . .	69
Figure 3.20	Live-cell RESOLFT-SPIM imaging of individual HIV-1 assembly sites	71
Figure 3.21	Improved lateral contrast in a biological sample by RESOLFT-SPIM	73
Figure 3.22	Live-cell imaging capabilities of RESOLFT-SPIM demonstrated on nuclear pore complexes	74
Figure 3.23	RESOLFT-SPIM images of the keratin-19 network in living HeLa cells	76
Figure A.1	Characterization of the afterglow effect.	85
Figure A.2	Sketch of a HIV-1 particle	89
Figure A.3	Comparison of imaging media for RESOLFT-SPIM . . .	90

List of Acronyms

2D	two-dimensional
3D	three-dimensional
APD	avalanche photodiode
DMEM	Dulbecco's modified Eagle's medium
DSLIM	digital scanned laser light-sheet fluorescence microscopy
dSTORM	direct STORM
FOV	field of view
FP	fluorescent protein
FWHM	full width at half maximum
GFP	green fluorescent protein
GSDIM	ground state depletion followed by individual molecule return
HIV	human immunodeficiency virus
LSFM	light-sheet fluorescence microscope
mEGFP	monomeric EGFP
NA	numerical aperture
NPC	nuclear pore complex
OPFOS	orthogonal-plane fluorescence optical sectioning
OTF	optical transfer function
PA-GFP	photoactivatable GFP
PALM	photoactivated localization microscopy
PBS	phosphate buffered saline
PMT	photomultiplier tube
PSF	point spread function
RESOLFT	reversible saturable optical fluorescence transitions
RSFP	reversibly switchable fluorescent protein
sCMOS	scientific complementary metal-oxide-semiconductor
SIM	structured illumination microscopy
SMS	single marker switching
SPIM	selective plane illumination microscopy
STED	stimulated emission depletion
STORM	stochastic optical reconstruction microscopy
UV	ultraviolet

Introduction

The beauty and diversity of nature is present in a wide range of physical dimensions. It is found in the minute movements of atoms as well as in the orbital courses of planets. However, only a fraction of these phenomena can be directly captured by our visual senses, whereas the majority is hidden to the naked eye. Since the early age in history the strong desire to extend the visual range to unseen dimensions has pushed forward the development of new optical instruments.

Especially the invention of the light microscope in the 17th century has provided completely new insights in the world of the small. A light microscope uses a lens or a combination of lenses to generate a magnified image of an object. Further advances in optics have directed science on new courses. Today, the light microscope is an indispensable tool in many fields of research including biology and medicine. It enables the direct visualization and investigation of internal structural components of living cells, tissues and whole animals together with their function.

The ability to distinguish and separate similar neighboring objects in a sample is a characteristic property of a microscope and is called its resolution. In order to visualize nanometer-sized constituents of a cell, also a spatial resolution in this range is needed. Many developments in optical microscopy hence aim for higher resolution, ideally in all three spatial dimensions. In this course, the theoretical description of image formation in the second half of the 19th century is regarded as a major contribution. The German physicist Ernst Abbe first pointed out that any two infinitesimally small objects located closer than the resolution limit of the lens-based system appear in the image as a single blurred entity with a finite size rather than two separable spots [1]. It is the phenomenon of diffraction that affects the propagating light waves and sets a physical limit for the resolution. The size of the blurred spot is, besides other parameters, proportional to the wavelength of the incident light.

An obvious approach to higher resolution is hence the use of electromagnetic waves with shorter wavelengths for far-field imaging. In fact, the invention of X-ray microscopy enabled resolutions below 20 nm [92, 19]. A modern electron microscope even offers spatial resolutions in the range of 0.05 nm [95, 31]. In addition to a comparably complex sample preparation, a major drawback of these techniques is the high-energy radiation, which is inherently destructive to biological specimens and renders live-cell imaging impossible. Other approaches use non-propagating evanescent light fields instead of a lens and thus achieve resolutions unlimited by diffraction [9, 14].

These near-field techniques resolve structures on the sub-100 nm scale, but their applications are bound to the surface of the sample.

Although the enormous gain in resolution with these techniques offered many new insights in life sciences, optical microscopy has kept its central role in this field. The reason is found in an advantage that is exclusively valid for light microscopy: It enables non-invasive investigation of fundamental processes that occur inside of living samples. In addition, the highly specific and sensitive detection by tagging the objects of interest with fluorescent markers has led to increased attention and use of this technique. Today numerous types of fluorescence far-field light microscopes can be found in laboratories all over the world.

A property in which many of these types differ is the ability to resolve features along the axis of detection, which is called optical sectioning. Multi-photon excitation [25] or confocal detection [108] have increased the optical sectioning capabilities of a wide-field microscope. A major drawback however remained: All of these techniques use a single lens system for coaxial illumination and detection of the sample. As a consequence, when multiple sections of a thick specimen are imaged, all sample planes are illuminated although only a small volume around a single plane is detected at a time. A solution to this issue has been found by the invention of selective plane illumination microscopy (SPIM) in 2004, where an orthogonal arrangement of lenses enabled optical sectioning with minimal light exposure of the sample throughout the experiment [77]. This technique is of particular interest since a parallelized readout allows for fast observation of biological specimens in their natural setting [89, 88]. Despite the inherent increase in optical sectioning by this objective arrangement, the axial resolution of conventional SPIM is, as in all aforementioned lens-based light microscopy techniques, still limited by diffraction.

Up to now, only one principle exists that lifts the limiting role of diffraction and enables an at least conceptual increase in resolution to the molecular scale or even beyond. It makes use of the inherent properties of a fluorophore. Successively turning some of the fluorophores in a diffraction-limited spot detectable while leaving others undetectable enables sequential readout of their signals [68]. This way, objects can be separated even at distances below the diffraction limit. This concept was first realized in a stimulated emission depletion (STED) microscope [93], which is a member of the RESOLFT family [61, 64], with the acronym RESOLFT standing for reversible saturable optical fluorescence transitions. In recent years, several other super-resolution techniques have been invented that only differ in the way the on-off switching is performed [13, 11, 36, 56].

Despite the success of STED, it typically requires high light intensities for substantial improvement in resolution [54]. Especially when imaging delicate samples where photoinduced changes need to be avoided, RESOLFT techniques are preferably realized with fluorophores that lead to the same factor in

resolution improvement at much lower light intensities. The class of reversibly switchable fluorescent proteins (RSFPs) poses a highly suitable species of fluorophores for this purpose [70]. The transition between the long-lived on- and off-state of these markers requires a saturation intensity I_{sat} of about five orders of magnitude lower than the typical on-off transition used in STED. The imaging capabilities of RSFP-based RESOLFT have been demonstrated in various biological applications [45, 15, 145, 46]. However, none of them could so far benefit from an increased axial resolution below the diffraction limit.

In this work a novel microscopy technique called RESOLFT-SPIM is presented that makes use of the advantages of far-field fluorescence microscopy in general and combines the advantages of SPIM and RSFP-based RESOLFT in particular. It is shown that a RESOLFT-SPIM microscope can acquire 3D information of a cell with optical sections thinner than the limit set by diffraction. At the same time, the RESOLFT light-sheet microscope, for the first time, offers sub-diffraction axial resolution in a RSFP-based RESOLFT nanoscope.

The thesis itself is structured as follows: Subsequent to this introduction, chapter 2 is intended to give an overview of the far-field fluorescence microscopy techniques that are applied in the course of this thesis. A main focus is set on the properties of RSFPs and their potential as fluorescent labels in RESOLFT nanoscopy, the advantages of light-sheets in light microscopy and the RESOLFT concept to overcome the diffraction barrier. Chapter 3 describes the novel work on RESOLFT-SPIM. The optical implementation and alignment strategies are presented. A description of the imaging strategy is followed by a detailed characterization of the setup. The imaging capabilities of RESOLFT-SPIM are demonstrated on biological samples. The results are summarized and discussed in chapter 4. An outlook to potential future upgrades of RESOLFT-SPIM is presented in chapter 5.

Far-field fluorescence microscopy

In the course of the past decades, far-field fluorescence microscopy has become a gold-standard tool in modern life sciences and especially in biology [78]. This chapter is intended to give an overview of its general principles starting with the basics of fluorescence and labeling. The second section introduces the concept of image formation in the far-field and describes the conventional diffraction-limited techniques of wide-field, confocal and light-sheet microscopy. The principle of non-diffraction-limited microscopy with a focus on the RESOLFT technique is explained in the last section of this chapter.

2.1 Fluorescence and labeling

An average biological cell contains about 10 billion proteins [107]. Great efforts have been made to understand their role in intracellular processes and the dynamics of their interactions. A quantitative understanding of these processes still poses a challenge for modern research. In order to investigate a single protein species in a cell, it needs to be discriminated from others in its surroundings. For this purpose, fluorescence microscopy makes use of selective fluorescent markers, so called *fluorophores*. They can be efficiently attached to the target molecules with high specificity. Only signals originating from these differentiated markers are captured, unlabeled molecules remain dark. Thus, single proteins, intracellular structures or entire cells can be observed over time with excellent signal-to-noise ratio and visibility. Different proteins or structures inside a specimen can be tagged with markers featuring distinguishable properties, which enables multi-color imaging and thus allows, for example, to monitor protein-protein interactions. Advances in biochemistry have led to excellent fluorophores suitable for applications in conventional far-field fluorescence microscopy as well as in non-diffraction-limited techniques. In particular, the RESOLFT-SPIM technique presented in this thesis makes use of the inherent properties of fluorescent markers to overcome the diffraction barrier. Therefore, a short overview of the general fluorescence process and the most common types of fluorophores is given in this section.

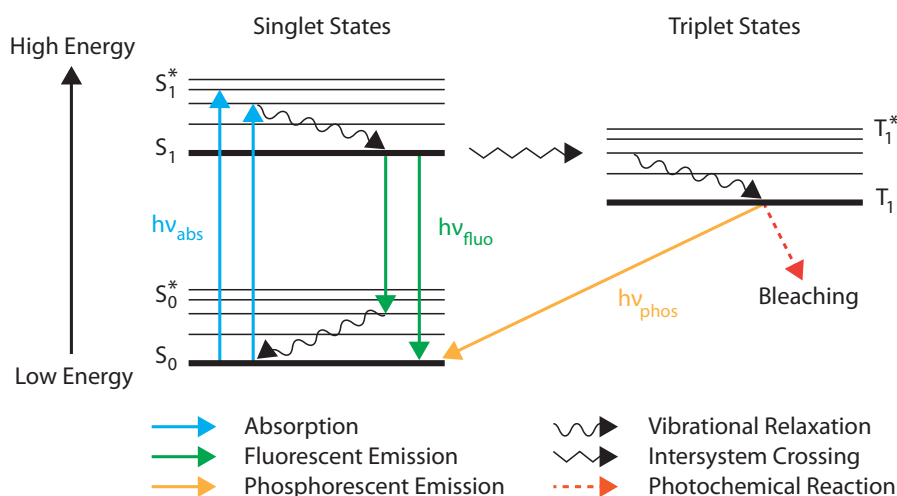


Figure 2.1: The Jablonski diagram illustrates the most important energetic states of a fluorescent dye and the most probable transitions between them. Absorption of a photon excites the molecule instantaneously from the ground state S_0 to energetically higher singlet states, e.g. S_1^* . Within picoseconds, the fluorophore relaxes in a radiationless transition to the lowest vibrational state. It remains there for the lifetime of few nanoseconds. With a high probability, the fluorescent dye then emits energy in form of a photon (fluorescence) while relaxing to the ground state or one of its vibrational states S_0^* . The alternate radiationless transition from S_1 to the triplet state T_1^* , for example, is called intersystem crossing. Transitions to a state of different multiplicity requires a spin-flip and are thus less probable. For this reason, the triplet state T_1 features an approximately 1000 times longer lifetime than S_1 . Photon emission from its lowest vibrational state is called phosphorescence. Photochemical reactions can ultimately damage the fluorophore and prevent it from signaling (photobleaching).

2.1.1 Basics of fluorescence

Fluorescence is the property of an atom or a molecule to emit electromagnetic radiation in the form of light after it has absorbed light with a shorter wavelength from another source. The processes involved in the absorption and emission of light by a fluorophore can be explained in a semi-classical model depicted by a Jablonski energy diagram in figure 2.1. The diagram illustrates the distinct electronic and vibrational energetic states that a fluorescent molecule can populate as well as the transitions between them. The vibrational states are illustrated as thin horizontal lines on top of thicker lines representing the electronic states. Rotational states are left out for clarity. A fluorophore in its equilibrium electronic ground state has spin-paired electrons and is thus in a singlet state S_0 . Absorption of a photon with an energy equal or higher than the band gap energy ΔE excites the fluorophore to an

energetically higher electronic orbital. ΔE is proportional to its frequency ν and inversely proportional to its wavelength in vacuum λ :

$$\Delta E = h\nu = \frac{hc}{\lambda}, \quad (2.1)$$

where h is the Planck constant and c is the speed of light in vacuum. The process of absorption happens on a time scale of roughly 10^{-15} seconds, which is too fast to permit significant motion of the nuclei in the fluorophore and accounts for a vertical transition (*Franck-Condon principle*). If the absorbed photon contains energy higher than ΔE , the molecule is excited to a higher vibrational state of S_1 , in the diagram denoted as S_1^* . From this state the fluorophore can release its energy on several different pathways. With a high probability, the excess energy of S_1^* is turned into heat without emitting radiation and the fluorophore relaxes to the lowest vibrational state. This process is called radiationless *internal conversion*. With an average delay in the order of nanoseconds, called the lifetime of S_1 , the molecule emits energy in form of a photon and fluoresces. By that, it directly populates the ground state S_0 or any vibrational state S_0^* from where it subsequently relaxes radiationlessly to S_0 . The photon emitted during fluorescence has less energy and thus a longer wavelength than the absorbed photon which results in a red-shift in the wavelength spectrum. This phenomenon, known as *Stokes shift*, can be experimentally used to separate the emitted fluorescent light from the incoming excitation light. With the help of appropriate spectral filters, the fluorescent signal is distinguished from scattered or reflected light and contributes to an image with excellent contrast.

The described absorption and emission process is only one example of a pool of possible transitions between the vibrational (and rotational) sub-states of the electronic states. From the perspective of quantum mechanics, the intensity of such a transition is proportional to the squared overlap integral between the vibrational wavefunctions of the two states involved in the transition. The intensity of all possible radiative transitions in a fluorophore can be plotted as a function of wavelength resulting in the *absorption* and *emission spectrum* specific for the fluorophore. For typical fluorophores used in optical microscopy, they both continuously span a broad band (cf. figure 2.2). Moreover, the spectra might be influenced by the surrounding media of the fluorophores in solution (inhomogeneous broadening in solvents).

In many cases, excitation of a fluorophore occurs without a change in electron spin-pairing which results in an excited state in the singlet system. Other state transitions including a process called *intersystem crossing* compete with the standard fluorescence emission pathway. A possible transition is the intersystem crossing from S_1 to the lowest excited electronic triplet state T_1 . In this state, the electron spins are unpaired leading to a non-zero total angular momentum. The reason for the low probability of these transitions stems from the fact that a spin flip is needed to produce the unfavorable process of

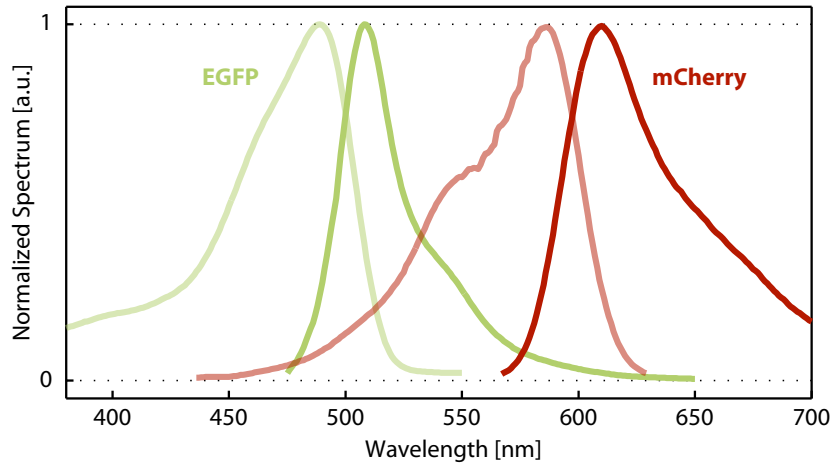


Figure 2.2: The absorption (light curves) and emission (dark curves) spectra of the well-known classical fluorescent proteins EGFP (green) and mCherry (red) are shown [79]. Fluorescent proteins are widely used markers in light-sheet microscopy. Their reversibly photoswitchable variants rsEGFP and rsCherryRev, have very recently been used in RESOLFT nanoscopy.

unpaired electrons. The direct transition from T_1 back to the ground state S_0 also requires a spin flip which leads to a comparatively long lifetime of the triplet state in the range of microseconds to milliseconds. Typically, the transition from T_1 to S_0 is radiationless. Only in rare cases a photon is emitted. This process is called *phosphorescence* and happens in the time range from milliseconds to hours. Fluorophores in a triplet state often react chemically with the molecules in their local environment, especially oxygen radicals. As a possible negative consequence, physiological processes in living specimen may be disturbed which can finally lead to cell death. Also, the fluorophores may be irreversibly destroyed resulting in a lower signal. These two processes are known as *phototoxicity* and *photobleaching*, respectively, and are regarded as major challenges in fluorescence microscopy of biological samples. Especially for live imaging of cells, the phototoxic effects can limit fluorescence imaging [91]. Numerous fluorescent markers are known and the number is increasing rapidly. The following section introduces the most common types of fluorophores and highlights their spectral properties. A particular focus is set on fluorophores that are used as markers in SPIM and RESOLFT techniques as well as the combined technique presented in this thesis.

2.1.2 Fluorescent labels

Synthetic Fluorescent Dyes

The importance of staining to enhance the contrast in light microscopy was recognized in the 19th century. In 1858, Joseph von Gerlach reported that the nucleus in brain tissue cells could be well differentiated from the cytoplasm and intercellular substances when it is stained with carmine, a reddish substance extracted from insects [137]. Other early dyes, such as malachite green and methylene blue were used in histology at that time. The probes provided contrast mainly by changing the light absorption properties of different cellular structures, but they were hardly fluorescent. In 1871, the German chemist Adolph von Baeyer synthesized the first fluorescent dye, which he named *fluorescein* and since then became one of the most popular fluorochromes ever designed. It has a very high quantum yield, but it is one of the least photostable dyes [101].

In the early 20th century, after the development of the first fluorescence microscope, fluorescent dyes were applied to enhance the autofluorescence of cells and tissues. A breakthrough in labeling was the development of the *immunostaining* technique by Albert Coons in 1942. He was the first who used labeled antibodies to identify pneumococcal antigens in infected tissue. Since then, this technique has been further improved and is today a routine tool in fluorescence microscopy and diagnostics.

In recent years, new species of fluorophores with several improved features, such as higher quantum yield, higher photostability, and enhanced water solubility have been developed. Prominent examples are the Alexa Fluor and the cyanine dyes. Fluorescence excitation and emission wavelength maxima of synthetic dyes are tuned specifically to match the wavelength of available laser sources. The number of today's dyes is estimated to lay in the range of hundreds covering the spectral range from ultraviolet (UV) to near-infrared. Although the RESOLFT concept is in principal applicable to any fluorescent molecule, the contrast in super-resolved images can be further improved by optimized labels. Outstanding results have been shown with numerous synthetic fluorescent dyes especially tuned for this purpose [156, 96]. Other realizations of the RESOLFT idea as well as light-sheet microscopy make use of fluorescent proteins (FPs), another species of fluorescent markers, introduced in the following.

Classical Fluorescent Proteins

Fluorescent proteins (FPs) are widely used fluorophores for in-vivo imaging in fluorescence microscopy [100]. In contrast to synthetic dyes that are introduced in the specimen from outside via fixation and permeabilization of the cell membrane, FPs can be encoded genetically and expressed directly inside

the specimen. All FPs have a highly fluorescent group, the chromophore, that is constrained and protected by a relatively large¹ β -barrel scaffold [138]. The barrel structure stabilizes the chromophore and shields it from the chemical environment. FPs do not require the assistance of specimen specific enzymes or cofactors. In fact, the chromophore is autocatalytically formed out of three aminoacids. Once the FP coding gene is introduced into a living organism, the cells can express the FP by themselves. To tag proteins, the FP coding sequence can be fused to their genes. The resulting fusion protein expressed by the specimen is then inherently tagged with an FP. Observing the fusion protein gives hint to the underlying labeled structure, localization, dynamics and interactions of the protein, ideally with little or no influence on the physiological environment.

The first fluorescent protein that has been purified, cloned and fully characterized was *green fluorescent protein (GFP)*. It was discovered by Shimomura and coworkers in 1962 as a companion protein to aequorin, a chemiluminescent protein in the northern-pacific jellyfish *Aequorea victoria* [133]. Purified wild-type GFP, has two absorption peaks that result from the protonation states of the chromophore: a major peak at a wavelength of 395 nm and a minor peak at 475 nm. Its emission exhibits a peak in the lower green region of the visible spectrum at 509 nm. The fluorescence quantum yield of wild-type GFP is 0.79 [110]. For the discovery and the development of GFP, Osamu Shimomura, Martin Chalfie and Roger Y. Tsien were honored with the Nobel Prize in Chemistry in 2008 [129].

Changes of the first amino acid of the chromophore or in the fluorophore environment modifies a variety of its physical properties [24, 131]. Via mutation of non-conserved residuals a multitude of different variants of naturally expressed FPs have been developed in recent years. Most commonly, new and improved derivatives are enhanced in their brightness, protein stability, photostability, pH stability, maturation kinetics, folding kinetics, and reduced oligomerization [131]. So far over a hundred fluorescent proteins are known whose emission spectra span the range from blue to far-red. Prominent examples besides the most widely used wild-type GFP derivate mEGFP are BFP, CFP, YFP, RFP, and DsRed [57, 109, 148, 130]. Advances in this field catalyzed several technical improvements on the microscope side, including the development of light-sheet microscopy [77] that will be introduced in section 2.4. In many super-resolution microscopy techniques the subgroup of photoswitchable fluorescent proteins is applied as labels.

Photoactivatable and Photoconvertible Fluorescent Proteins

Photoactivatable fluorescent proteins are initially in a non-fluorescent state. They can be turned active by absorption of light that triggers structural chan-

¹ The β -barrel has a size of about 25 kD, which is relatively large compared to the average size of organic fluorophores of around 1 kD.

ges of the fluorophore [102]. Only in this state, the FPs are able to be excited and fluoresce. The wavelength of activation differs from the excitation wavelength and is typically shorter. For example, *photoactivatable GFP (PA-GFP)* is switched by UV light to a fluorescent state, in which it can be stimulated with light around 488 nm for green fluorescence emission [111]. Photoconvertible FPs have the ability to irreversibly switch from one fluorescence color to another upon irradiation with light [3, 49]. One example is the photoactivatable FP named *Kaede* that fluoresces in the green spectral range after excitation at 480 nm. UV light induces a photoconversion that leads to emission of red fluorescence with a maximum at 582 nm and a shoulder at 627 nm [3]. Photoactivatable and photoconvertible FPs are mainly used to track proteins over time [111, 22] or for single molecule switching methods in super-resolution microscopy introduced in section 2.5.

Reversibly Switchable Fluorescent Proteins

The group of reversibly switchable fluorescent proteins (RSFPs) has been developed recently [103]. These FPs can be reversibly switched between a fluorescent and a non-fluorescent state upon exposure to light of different wavelengths. The switching process in modern RSFPs can be repeated multiple times. The structural basis of switching in conventional RSFPs is a cis-trans isomerization of the chromophore [7, 6, 140, 44], mostly accompanied with a change of the chromophores protonation state [127, 124].

The first protein with these properties found in the sea anemone *Anemone sulcata* was named *asFP595* [103]. It exhibits a so called positive switching behavior, meaning that with the same wavelength, the protein can be both, activated and excited. In the case of *asFP595*, a wavelength around 480 nm is used for this purpose. The emission is in the red range of the spectrum. With a maximum efficiency at 450 nm the protein can be reversibly photoswitched back to the non-fluorescent state. The fluorescent protein *Dronpa*, extracted from pectinidae corals, is an example for an RSFP featuring a negative switching behavior [4, 53]. After activation with light of 405 nm wavelength, *Dronpa* can be excited with light of 488 nm and fluoresces green peaking at 518 nm. In a competing process, 488 nm light also switches the protein back into the off-state. *Dronpa* variants with improved properties have been developed via mutagenesis. *Dronpa-M159T*, for example, exhibits a 50 times faster off-switching kinetics compared to the original version of *Dronpa* [140].

In 2008, the first monomeric red emitting RSFPs with positive (*rsCherry*) and negative switching modes (*rsCherryRev*) have been reported [139]. Very recently, the further improved variant *rsCherryRev1.4* has been developed and applied in microscopy [99].

Via mutagenesis, a modified version of monomeric EGFP (mEGFP) has very recently been turned into an RSFP, that was called *rsEGFP* (=EGFP(Q69L, V150, V163S, S205N, A206K)) [44]. *rsEGFP* provides optimal photophysi-

Table 2.1: Comparison of EGFP, rsEGFP, rsEGFP2, and rsEGFP(N205S) in terms of their absorption maximum in the off-state λ_{ab}^{max} , the excitation maximum in the on-state λ_{ex}^{max} , the emission maximum λ_{em}^{max} , the fluorescence quantum yield QY, the extinction coefficient EC, and the residual fluorescence in the off-state R_{fl} . The values are taken from [20, 46, 110].

Fluorescent protein	λ_{ab}^{max} [nm]	λ_{ex}^{max} [nm]	λ_{em}^{max} [nm]	QY [norm.]	EC [$M^{-1}cm^{-1}$]	R_{fl} [%]
EGFP	n/a	489	509	0.60	53.000	n/a
rsEGFP	396	493	510	0.36	47.000	1-2
rsEGFP2	408	478	503	0.30	61.300	3-4
rsEGFP(N205S)	407	491	510	0.45	57.000	2-3

cal properties for RESOLFT microscopy such as high brightness, fast switching, high photostability, and hardly any residual fluorescence in the off-state. One of its variants, the monomer *rsEGFP(N205S)*, switches to the off-state 2–5 times slower than rsEGFP at the same light intensities, but in consequence emits about twice as many photons per cycle [20]. It thus provides an improved signal-to-noise ratio in RESOLFT images. A 6.5 times² faster off-switching rate with otherwise similar properties compared to rsEGFP has been shown for *rsEGFP2*, which was developed by mutating the switchable mEGFP variant mEGFP(T65A) [44, 46]. In table 2.1 the spectral and physical properties of the reversibly switchable mEGFP variants are summarized and compared to the standard non-switchable EGFP.

RSFPs have already been used as rewritable data storage media, where the two different fluorescent states represent the zeros and ones of the binary code [45]. Moreover, the invention of RSFPs had an extraordinary impact in the field of super-resolution microscopy discussed in section 2.5. As markers in single marker switching (SMS) techniques, for example, RSFPs can be switched and imaged multiple times without the need for subsequent bleaching. In this terms, RSFPs outperform photoactivatable and photoconvertible FPs [37, 5, 139]. In RESOLFT nanoscopy, RSFPs can be effectively switched at low light intensities. This minimizes the risk of phototoxic effects. Thus, RSFPs are ideally suited for live cell applications [45, 20, 99].

2.2 Wide-field microscopy

Wide-field microscopy, often also referred to as epifluorescence microscopy is a traditional technique in fluorescence microscopy. Figure 2.3 shows a sketch

² The difference of the off-switching rates of rsEGFP and rsEGFP2 is reduced for higher intensities.

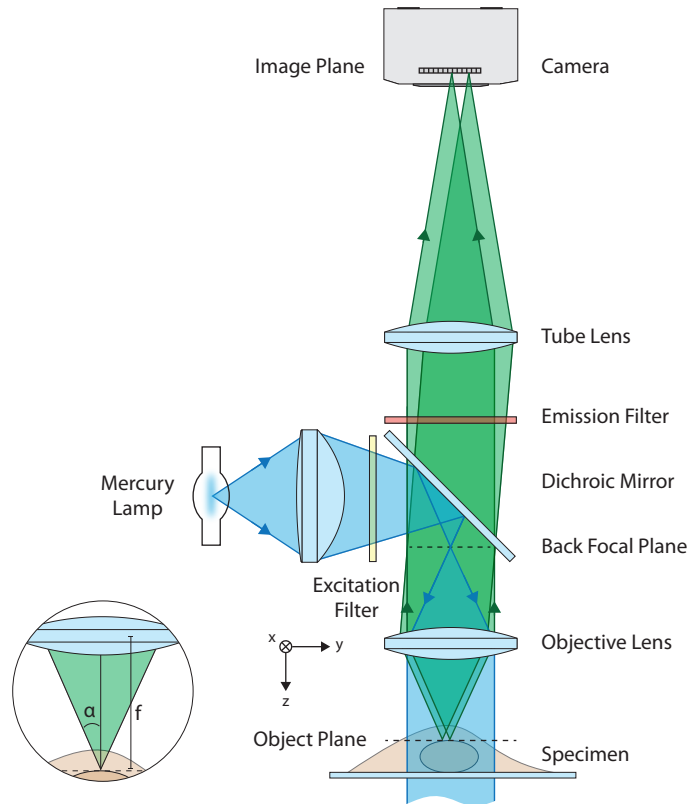


Figure 2.3: Schematic drawing of a wide-field microscope. The essential parts of a standard wide-field fluorescence microscope are depicted together with the illumination (blue) and detection (green) beam paths. A broadband light source illuminates an area of the specimen, which is imaged via the objective lens onto a camera.

of a typical wide-field setup. The region of interest of a sample marked with fluorophores is placed in the focal plane of the imaging lens, i.e. the objective lens, and is illuminated homogeneously throughout the field of view (FOV). Either a broadband lamp or a laser serves as light source, which is focused into the back-focal plane of the objective. Fluorescence is collected by the same objective lens, separated from the excitation light by a dichroic long pass filter, and imaged on a sensitive camera in a single exposure. The image contrast can be further improved if additional excitation and emission filters are placed in the beam path. Typically, a combination of an objective lens and a tube lens is used to form the image. The magnification M of this system is defined by the ratio of the focal distances of the tube lens f_{tub} and of the objective lens f_{obj} . The numerical aperture (NA) is defined as

$$NA = n \sin \alpha, \quad (2.2)$$

with n being the refractive index between sample and the objective lens and α the half opening angle of the objective lens (cf. figure 2.3). The readout

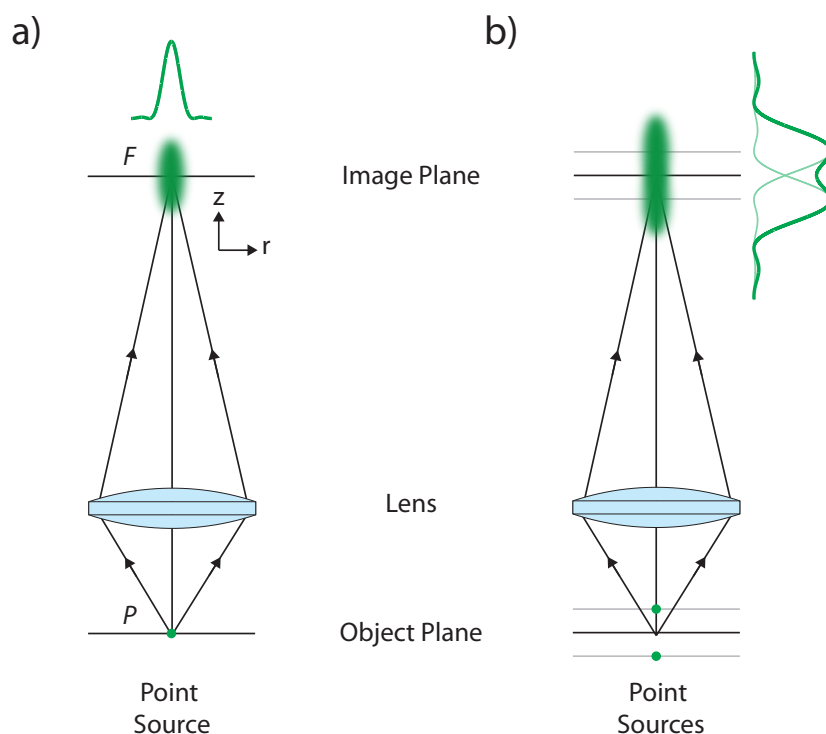


Figure 2.4: The concept of image formation with a lens and the Rayleigh criterion. a) A point source at point P is imaged by a lens onto the image plane. Due to diffraction, the light is spread around F and forms a three-dimensional (3D) intensity distribution, which is called the intensity PSF of the system. b) According to Rayleigh, two point sources, e.g. above and below the object focal plane, can still be discerned in the image space if the maximum of the intensity PSF in axial direction falls into the first minimum of the second.

of the fluorescence signal from the sample in such an imaging system is intrinsically parallelized and thus faster than microscopy techniques based on point-scanning.

2.2.1 Imaging with a lens

Although a wide-field microscope consists of several lenses, we can reduce the concept of image formation to that of an aberration-free single lens system, illustrated in figure 2.4. Let us assume a point-like source of light, e.g. an emitting single fluorophore in a specimen, placed at position P . It is imaged by an ideal thin lens to F , e.g. a planar detector on the optical axis. Due to diffraction of light at the circular aperture of the lens, the light is spread around F and forms a 3D intensity distribution [105], which is called *intensity point spread function (PSF)*. It is an important feature of an imaging system and helps defining its lateral and axial resolution. In the scalar theory of

diffraction, where polarization effects are neglected, the function describing the intensity PSF is derived as

$$H(u, v) = C_0 \left| \int_0^1 J_0(vr) e^{-i\frac{1}{2}ur^2} r dr \right|^2. \quad (2.3)$$

C_0 is a constant that normalizes $H(u, v)$ to unity and J_0 is the zero order Bessel-function of the first kind. The normalized variables u and v are so called *optical coordinates* and relate to the spatial coordinates along the optical axis (z), and in the lateral direction (x, y), respectively [132], as

$$\begin{aligned} u &= \frac{8\pi n \Delta z}{\lambda} \sin^2 \left(\frac{\alpha}{2} \right), \\ v &= \frac{2\pi n \Delta r}{\lambda} \sin \alpha, \quad \text{where } r = \sqrt{x^2 + y^2}. \end{aligned} \quad (2.4)$$

Here, n denotes the refractive index, λ is the wavelength of light and α is the half opening angle of a lens as defined in figure 2.3. Several assumptions have been made to end up with equation 2.3. First, the lens is illuminated uniformly by a plane wave. Second, F is a position in the far-field of the lens meaning that its distance to the lens along the optical axis is much larger than the maximal distance of the field amplitude from the optical axis. Third, the magnification is set to $M = 1$. The three-dimensional PSF has a cylindrical symmetry and is elongated along the optical axis. It is worth mentioning that the intensity PSF in optical coordinates is fully determined by the NA and the wavelength of light.

A more visualized image of a PSF is given by a photon optics interpretation. Often, the intensity PSF is seen as the probability density that a photon that originates from P arrives at a certain point (u, v) near F . Another explanation makes use of the fact that the image formation model is space invariant and sees $H(u, v)$ as the probability that a photon emitted at a point near F reaches point P . The distribution of probabilities in the focal plane leads to

$$H(u = 0, v) = C_0 \left| \int_0^1 J_0(vr) r dr \right|^2 = \left(2 \frac{J_1(v)}{v} \right)^2, \quad (2.5)$$

where J_1 is the first order Bessel-function of the first kind. The two-dimensional distribution features a central disk that includes the main maximum and is surrounded by less pronounced concentric rings. The first zero position is found at $v = 3.83$, which in combination with equation 2.4 gives the radius of the central disk, also known as the Airy disk:

$$\Delta r = \frac{3.83}{2\pi} \frac{\lambda}{NA} = 0.61 \frac{\lambda}{NA}. \quad (2.6)$$

The distribution along the optical axis expressed in optical coordinates can be obtained from equation 2.3 by setting $v = 0$:

$$H(u, v = 0) = C_0 \left(\frac{\sin \frac{u}{4}}{\frac{u}{4}} \right)^2. \quad (2.7)$$

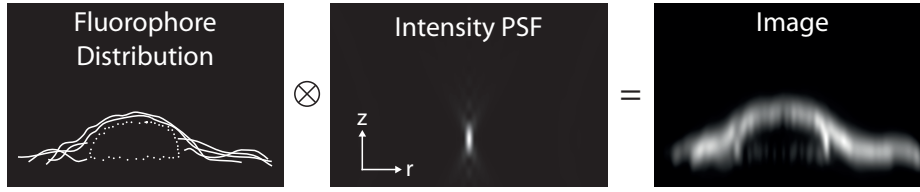


Figure 2.5: An r - z cross-section of a simulated specimen (left) is convolved with an anisotropic PSF (center) to yield the image (right). The extent of the PSF in z is larger than in r which results in a severe blur in the z -direction. Features that have an actual axial distance of less than the axial resolution cannot be discerned.

The first zero of $H(u, v = 0)$ is found at $u = 4\pi$ yielding:

$$\Delta z = \frac{2n\lambda}{NA^2}. \quad (2.8)$$

In a biological sample the structures or proteins of interest are densely labeled with fluorophores, so that their distribution resembles the distribution of fluorescent molecules. An extended image I obtained in a light microscope is thus a 3D convolution of an object O consisting of a multitude of single fluorescent emitters with the imaging PSF H defined by the detection light path:

$$I(u, v) = O(u, v) * H(u, v). \quad (2.9)$$

For the same reasons a single light source is blurred in the image, an extended object is similarly affected (Figure 2.5). Simultaneously stimulating the fluorescence of markers in a 3D volume results in an image on the detector, e.g. a camera that is severely deteriorated by out-of-focus light.

2.2.2 Resolution of wide-field microscopes

According to the definition of Lord Rayleigh [117], two emitters in the object space can still be discerned in the image space if the maximum of one falls into the first minimum of the second. The resolution along the axial direction is always lower than along the lateral directions. In practice, the Airy disk is often approximated by a two-dimensional Gaussian function. The error in fitting the maximum as well as in neglecting the intensity in the side lobes is marginal. Often, the full width at half maximum (FWHM) of the Gaussian approximation is used to characterize the optical resolution of a microscope.

The counterpart of the PSF in the Fourier domain is called optical transfer function (OTF), which is related to the PSF via a simple Fourier transform. The OTF gives a measure of the transmittance of the optical system as a function of spatial frequency. High spatial frequencies are required to resolve small features. However, for these frequencies the amplitude of the OTF is re-

duced e.g. by the circular aperture of the objective lens, which poses the most fundamental resolution limiting factor of an optical microscope [48, 105].

Besides the diffraction-limited resolution, wide-field microscopy suffers from another severe drawback. Illumination is not limited to the focal plane, but spans the axial range of the entire sample. As a consequence, any two-dimensional (2D) image of a thick specimen captured with this technique contains the fluorescence signals from fluorophores located in the focal plane and from those located in planes above and below. Often the out-of-focus light greatly reduces the contrast of the image and can, in the worst case, completely obscure the in-focus details [23]. This in fact limits the broad range usage of wide-field microscopy in studies of specimens with even moderate thickness. In the last few decades, novel optical setups emerged that are able to separate signals from small volumes around the focal plane against background light. Among all these optical sectioning techniques, confocal microscopy and SPIM appear to be the most powerful. They are introduced and discussed in the following.

2.3 Confocal microscopy

Whereas a conventional wide-field microscope uniformly illuminates an area of a specimen, scanning fluorescence microscopes excite the fluorophores in the sample point-by-point. A *confocal scanning microscope* is the most widely used variant of a scanning microscope. Originally patented by Minsky in 1957 [108], it has become a standard technique for biological imaging and reconstruction of three dimensional structures [113] in fixed and living samples.

The principle of confocal microscopy can be explained with the schematic drawing shown in figure 2.6. An initially collimated laser beam is focused by an objective lens to a single focal illumination intensity PSF inside the specimen. Fluorescence is collected by the same objective lens using the inverted excitation light path to the dichroic long pass filter. Subsequently, a tube lens focuses the transmitted fluorescence light onto a pinhole exactly located in the imaging plane. The diameter of the pinhole is typically set to the diameter of the detection Airy disk in that plane. The pinhole blocks light originating from fluorophores outside the focal volume, that are not sharply imaged on the focal plane of the tube lens. An avalanche photodiode (APD) or a photomultiplier tube (PMT) on the optical axis detects the light that passes through the opening of the pinhole. Scanning the laser beam point-by-point across and inside the sample while simultaneously recording the collected fluorescent light at each scan position sequentially reconstructs a 3D image. Scanning is typically performed by changing the angle of the incident beam in the back-focal plane of the objective lens with one galvanometric mirror or by translating the focal spot in the first image plane with two galvanometric

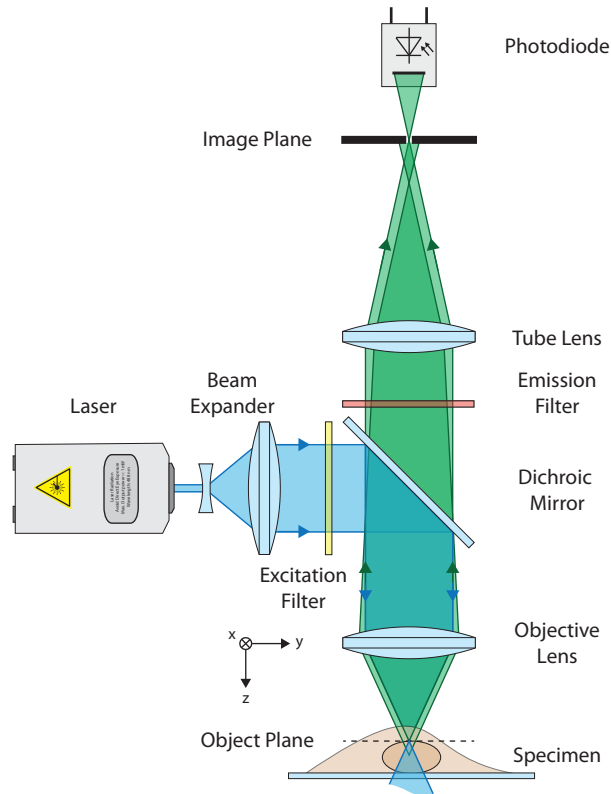


Figure 2.6: Schematic drawing of a confocal microscope. The main components and the excitation (blue) and detection (green) beam paths of a typical confocal fluorescence microscope are illustrated. The sample is illuminated with a focused laser beam. Moving the specimen through a stationary beam or the laser beam across and inside the sample results in a sequential reconstruction of the 3D structure. The scanner is not shown for simplicity. A pinhole effectively blocks out-of-focus light to achieve optical sectioning.

mirrors per scan dimension. Alternatively, the specimen can be mounted on a piezoelectric stage that moves through the stationary focal spot.

In a standard confocal microscope, the probability that a fluorophore at a point $P(u, v)$ in the specimen contributes to the signal on the detector depends on the probability that an illuminating photon arrives at $P(u, v)$ and the probability that a photon emitted at $P(u, v)$ hits the detector. Since the illumination and detection are independent events, the resulting intensity PSF of the confocal microscope H^{conf} can be calculated by the product of the excitation intensity PSF (H_{ill}) and the detection intensity PSF (H_{det}) at this point:

$$H^{conf}(u, v) = H_{ill}(u, v) \cdot H_{det}(u, v) \quad (2.10)$$

For a small pinhole, $H_{ill}(u, v)$ and $H_{det}(u, v)$ only differ in the wavelength of illuminating and detected light. They can be regarded as almost identical

since the Stokes shift for most fluorophores is in the range of only few tens of nanometers. Therefore, the confocal intensity PSF is well approximated by the square of a single lens PSF. Theoretically the lateral resolution is thus a $\sqrt{2}$ better than in a wide-field microscope. In addition, the photon energy density in an x - y plane is dependent on the position along the optical z -axis. Fluorophores outside the central region of the confocal PSF are very unlikely to contribute to the signal. Optical sectioning is achieved by scanning the axially confined intensity PSF through a thick specimen.

Over the years, several variants of confocal microscopes have been developed that differ mostly in the way lasers interact with the sample. However, all these point-scanning setups and also conventional wide-field microscopes suffer from a severe drawback: When acquiring an image stack along the optical z -axis, these techniques conceptually illuminate the entire sample at each scanning step. Laser light for fluorescence excitation passes through the whole specimen, although only a single section is observed at a time. As a result, photobleaching of fluorophores and phototoxic changes in the specimen often occur, which also constrains the potential of these techniques for live cell imaging [89, 149].

2.4 Light-sheet fluorescence microscopy

In-vivo imaging of three-dimensional specimens requires careful tuning of the imaging parameters, such as speed, spatial resolution, contrast and photosensitivity. In recent years, an imaging technique called *light-sheet fluorescence microscopy* stands out by balancing most of these parameters. The basic concept can be explained with the sketch shown in figure 2.7. In simple terms, in a conventional light-sheet fluorescence microscope (LSFM) the excitation light illuminates a single slice of the specimen from the side while the emitted fluorescence light is detected from the top. Typically a laser beam is focused only in one direction to create a thin sheet of light inside the specimen. Fluorescence is detected orthogonally to the illuminated plane in a standard wide-field setup. The focal plane of the detection objective lens has to coincide with the illuminated volume. Only fluorescent molecules that are excited within a volume around the focal plane contribute to the signal. Fluorophores above and below the light-sheet are by design not illuminated and thus not stimulated for fluorescence. As a result, optical sections of living or fixed specimen are obtained in a direct and nondestructive manner without spatial filtering. The sections are suitable to reconstruct a three-dimensional volume of the imaged specimen. A light-sheet microscope is able to record samples ranging from a single cell to a whole organism with outstanding contrast. The latter is even increased for thinner sections [72].

Due to the intrinsic parallel readout of fluorescence over an entire section of the specimen, the acquisition time is drastically reduced as compared to

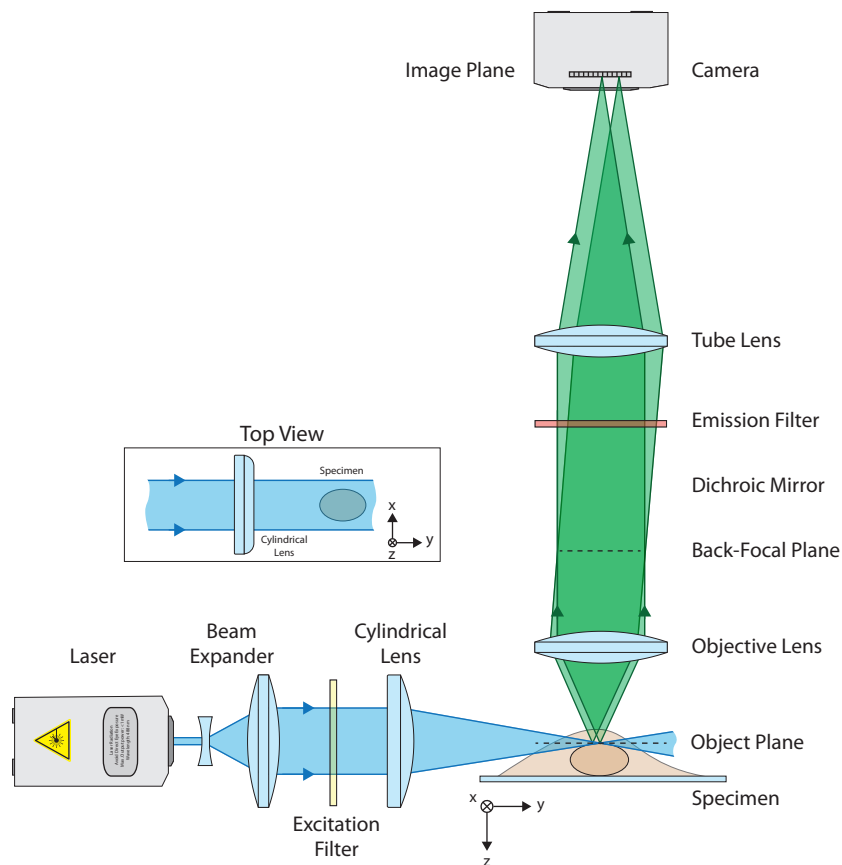


Figure 2.7: The essential parts of a fluorescence light-sheet microscope. Fluorescence excitation (blue) and detection (green) are divided into two distinct beam paths. The specimen is illuminated in a plane perpendicular to the detection axis. An objective lens and standard wide-field optics image the labeled features in the sample onto a camera. Illumination optics are chosen such that only a thin volume around the focal plane of the detection objective is illuminated. This concept has been technically realized in many different ways. The most common implementation creates a sheet of laser light with the help of a cylindrical lens.

sequential readout in point-scanning techniques. Data acquisition in light-sheet microscopy can be extremely fast and efficient. Due to the ongoing development of sensitive pixel-based detectors and piezoelectric stage scanners, the advantage in imaging speed is becoming even more pronounced. Current scientific complementary metal-oxide-semiconductor (sCMOS) cameras allow for acquisition of 4-5 megapixel images at speeds of up to 100 frames per second. A recording rate of 175 million voxels/s has been reported on living specimens [97, 147].

A light-sheet microscope provides images with a signal-to-noise ratio that is typically one or two orders of magnitude higher than in images taken with a 2D point-scanning microscope [90, 142]. This stems from the fact that only thin sections of a sample are illuminated which reduces out-of-focus light. It has a positive consequence on the imaging strategy: The photo-exposure of the sample can be minimized without reducing the contrast in the image. Lowering unfavorable side effects of high laser intensities such as irreversible modifications of the sample and photobleaching of the fluorescent markers allows for continuous imaging over a long period of time. In fact, phototoxicity has been shown to be very low in light-sheet microscopy and significantly less than in confocal or wide-field microscopy [115, 120, 122].

2.4.1 The use of light-sheets in light microscopy

Because of the aforementioned advantages, LSFM has gained popularity over the past few years. The basic idea, however, and the first realization of a very simple version of a light-sheet based microscope, called *ultramicroscope*, has been published over 100 years ago. In 1902, Heinrich Siedentopf and Richard Zsigmondy visualized colloidal nanometer-sized gold particles dispersed in solution. The light-sheet was generated by illuminating a thin slit with sunlight. It was imaged in the object plane by an objective lens at a right angle to the direction of observation [135]. By that, the scientists were able to visualize and count moving particles in a given volume and derive their sizes. For his advances in colloid chemistry research, including the invention of the ultramicroscope, Zsigmondy was awarded the Nobel Prize in Chemistry in 1925.

The invention of fluorescence microscopy, the laser and lenses with the ability to generate light-sheets, stimulated the development of more light-sheet based techniques. However, none of them answered a biological question at this time. It took until 1993 that the first laser-based light-sheet was generated to excite fluorescence in biological samples [150]. Following the example of ultramicroscopy, a technique called *orthogonal-plane fluorescence optical sectioning (OPFOS)* was developed to study the anatomy of whole fluorophore-stained and cleared guinea pig cochleas in optical sections. Although several articles about LSFMs have been published in well-respected journals at that time, all the developed methods were not considered as a real break-

through. However, their invention laid the foundation of the most prominent version of an LSFM developed in 2004: *selective plane illumination microscopy (SPIM)* [77]. The full live imaging potential of LSFM could be harvested with genetically encoded FPs, which also accelerated the development of new LSFM techniques since then.

2.4.2 Selective plane illumination microscopy (SPIM)

This subsection gives a short overview of the principles, recent applications and challenges of the SPIM technique. It serves as a basis for improvements such as the super-resolution light-sheet technique presented in this thesis.

2.4.2.1 Generic SPIM setup

A generic SPIM setup consists of four fundamental parts: an illumination beam path, a detection beam path, a specimen chamber, and a specimen mount. A typical illumination beam path contains a continuous wave laser, a beam expander and optics that produce a light-sheet. In modern SPIM microscopes, light-sheets are generated on two different ways: The one uses a *cylindrical lens* that focuses an expanded laser beam in only one direction into the specimen chamber or the back-focal plane of the illumination objective [77, 42]. The light-sheet and the detection objective are stationary while the sample is moved step-wise through the focal plane. The entire field of view is illuminated and imaged at once. Thus, the laser power of the exciting beam that passes the rear pupil of the objective lens is distributed over the entire sheet. A cylindrical lens is easy to place in the beam path and does not require moving components and additional electronics. The other option uses a single or multiple beams that are moved across one specimen section within the exposure time of the detector and thereby generate a so called *virtual sheet of light*. The technique is called digital scanned laser light-sheet fluorescence microscopy (DSLIM)[90]. A DSLM applies the same energy load to the specimen as LSFMs with illumination through a cylindrical lens. However, their peak illumination power is typically up to 100 times higher [90]. Potential saturation effects increase the probability of photo-bleaching and broaden the light-sheet.

The detection beam path is typically designed as a standard wide-field microscope including an objective lens, an emission filter, and a tube lens. For more details see section 2.2. The samples studied in LSFM are generally living organisms such as embryos, cell colonies or individual cells. Therefore, they need to be immobilized in front of the objectives in a way that is compatible with both acquisition of high quality images with the necessary spatial and temporal resolution and normal development of the specimen. In a standard SPIM, large biological specimen are stably embedded in a cylinder of agarose or other optically clear, non-toxic mounting gel, that are immersed

in water-based medium [77]. The gel protects the organism and keeps it in position during image acquisition. In some chambers, temperature and CO₂ concentration is controlled to match the natural environmental conditions of the specimen. During typical image acquisition, a piezoelectric stage step-wise moves the mounted specimen through the focal plane of the detection objective. A three-dimensional stack of recorded images is thus built up layer-by-layer.

2.4.2.2 Recent applications and technical advances of SPIM

Practical realizations of SPIM are diverse and are adapted to the sample of interest, its size, the desired magnification, and the immersion medium [76]. Since 2004, SPIM and its variants have systematically tackled a variety of biological questions. Their applications cover a wide range on the scale of time and specimen size. Complex dynamic processes in comparatively small structures such as nuclei in single cells, in growing cell colonies or in entire animals can be recorded within a fraction of a second and over a time period of hours. In the first years after the invention of SPIM, many applications mainly focused on embryonic development. In zebrafish larvae, for example, fast developing single neurons [87, 2] or cell movements in the early stages [89, 86, 123, 141] could be monitored at fast rates in three dimensions over a long period of time. Furthermore, entire *Drosophila* embryos that develop despite continuous laser irradiation were imaged at 30 second intervals over a period of 24 hours [147]. Moreover, SPIM enables imaging of highly photosensitive samples, such as the vasculature and neuroanatomy in mice [81, 12]. Parallelized SPIM variants that use multiple illumination and detection arms speed up the acquisition procedure and reduce image artifacts generated by light absorption, refraction and scattering [75, 143, 125]. Thus, individual nuclei inside a large specimen can be precisely tracked [97, 147]. If rotation is not needed, especially when imaging sub-cellular structures, other optical realizations of the SPIM concept can be more favorable. In an implementation, the water-dipping illumination and detection objectives were tilted by 45° with respect to the scanner for single cell imaging and diffusion measurements [17] and for studies of larger specimens [155]. A similar objective arrangement is used in the RESOLFT-SPIM setup presented in this thesis.

2.4.2.3 Spatial resolution of SPIM

The PSF of a SPIM is described by the product of the illumination and detection PSF. The lateral extent of the PSF of a conventional SPIM is mainly given by the detection optics and thus equivalent to a wide-field microscope. According to equation 2.6 the spot size of a single emitter on the camera is inversely proportional to the NA of the detection objective. It ranges between 240 and 1000 nm for water-dipping objectives [30].

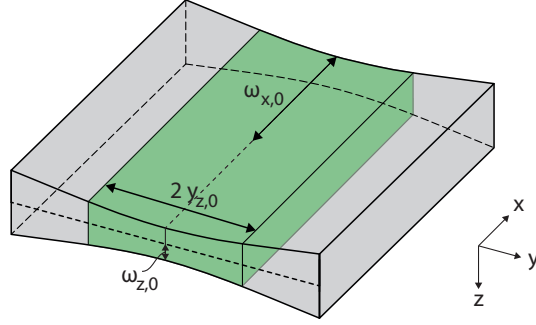


Figure 2.8: Sketch of a light-sheet and its dimensions. Along the optical axis of illumination, y , the light-sheet features a hyperbolic shape in the x - and z -direction. The position of minimal waist in each direction is typically set to the center of the FOV of detection. The boundaries of the FOV are defined by the Rayleigh-range distance from the center where the light-sheet is approximately $\sqrt{2}$ thicker than in the middle. Because of a comparably large Rayleigh range in the x -axis, the FOV in this direction is almost homogeneously illuminated. The FOV in the y -axis is mainly determined by the illumination NA and is typically shorter for thin light-sheets in a conventional SPIM. The volume highlighted in green marks the effective detection volume.

Since illumination and detection are separated in SPIM and oriented perpendicularly, the extent of the PSF along the detection axis is dominated by the lateral extent of the illumination PSF, i.e. the light sheet thickness. If the light-sheet is thicker than the axial extent of the detection PSF, the axial resolution is determined by the NA of the detection objective. An ideal light-sheet is as thin as possible and excites fluorescent molecules only in the focal plane of the detection objective.

In the following, some of the optical parameters of a SPIM setup including its resolution are derived from the paraxial Helmholtz equation,

$$\nabla_T^2 U(x, y, z) - ik \frac{\partial U(x, y, z)}{\partial y} = 0. \quad (2.11)$$

Here, it is assumed that light propagates along the y -axis. Furthermore, $\nabla_T^2 = \partial^2/\partial x^2 + \partial^2/\partial z^2$ is the transverse part of the Laplace operator, $U(x, y, z)$ is the complex amplitude of a paraxial wave, $k = 2\pi n/\lambda$ is the wave vector, λ is the wavelength of light in vacuum, and n is the refractive index. Besides the simple Gaussian beam solution, another eigenfunction of this partial differential equation is the elliptical Gaussian-beam:

$$U(x, y, z) = A_0 \cdot \sqrt{\frac{\omega_{x,0}}{\omega_x(y)}} \sqrt{\frac{\omega_{z,0}}{\omega_z(y)}} \cdot e^{-\left(\frac{x^2}{\omega_x^2(y)} + \frac{z^2}{\omega_z^2(y)} + i\varphi(x, y, z)\right)}, \quad (2.12)$$

where A_0 is the amplitude of the paraxial wave and φ is the phase part of the wavefunction. The parameters $\omega_{x,0}$ and $\omega_{z,0}$ denote the beam radii at the

thinnest position of the Gaussian beam profile along the x - and z -axis, respectively. In the following they are referred to as the beam waists in x - and z -direction. Along the illumination axis y , the radii of the beam diverge in a hyperbolic shape and can be expressed as a function of the distance from the beam waist:

$$\omega_x(y) = \omega_{x,0} \sqrt{1 + \left(\frac{y}{y_{x,0}}\right)^2} \quad \text{and} \quad \omega_z(y) = \omega_{z,0} \sqrt{1 + \left(\frac{y}{y_{z,0}}\right)^2}. \quad (2.13)$$

The distance to the center at which the beam waist is increased by a $\sqrt{2}$ is called the Rayleigh range. In x - and z -direction it is denoted as $y_{x,0}$ and $y_{z,0}$, respectively, and connected to the corresponding beam waist radii by:

$$y_{x,0} = \frac{\pi n \omega_{x,0}^2}{\lambda} \quad \text{and} \quad y_{z,0} = \frac{\pi n \omega_{z,0}^2}{\lambda}. \quad (2.14)$$

The light intensity of an elliptical Gaussian beam at a particular position in the sample is described by:

$$\begin{aligned} I(x, y, z) &= U(x, y, z) \cdot U^*(x, y, z) \\ &= |A_0|^2 \cdot \frac{\omega_{x,0}}{\omega_x(y)} \cdot \frac{\omega_{z,0}}{\omega_z(y)} \cdot e^{-2\left(\frac{x^2}{\omega_x^2(y)} + \frac{z^2}{\omega_z^2(y)}\right)}. \end{aligned} \quad (2.15)$$

Such elliptic Gaussian beams are used for light-sheet illumination in SPIM. An example is sketched in figure 2.8. The minimal light-sheet thickness $\omega_{z,0}$ gives a measure for the maximal axial resolution of a SPIM microscope according to the Rayleigh criterion. It can be expressed in terms of the NA of an illumination objective by

$$\omega_{z,0} = \frac{2}{\pi} \frac{\lambda}{\text{NA}}. \quad (2.16)$$

In the course of this thesis, $\omega_{z,0}$ is often converted to a FWHM value by $\Delta z = \sqrt{2 \ln 2} \omega_{z,0}$. The position of minimal waist is typically aligned with the center of the FOV of detection. The boundaries of the FOV of detection are defined by the Rayleigh range distances in either direction from the center. The effective FOV of the microscope thus depends on the width of the elliptical Gaussian beam in x - and z -direction along the optical axis:

$$\begin{aligned} \text{FOV}_x &= 2y_{x,0} = \frac{2\pi n \omega_{x,0}^2}{\lambda} \\ \text{FOV}_y &= 2y_{z,0} = \frac{2\pi n \omega_{z,0}^2}{\lambda} = \frac{8n}{\pi} \frac{\lambda}{\text{NA}^2}. \end{aligned} \quad (2.17)$$

The FOV in the x -direction can be controlled by the focal length of the cylindrical lens. It is typically larger than the physical size of the camera chip projected in the system of the sample. The FOV in the y -direction is strongly dependent on the illumination NA.

Towards higher resolution in SPIM

The resolution of SPIM is pushed to the diffraction limit by using the full aperture of the implemented illumination objective. An illumination NA of 0.8, for example, was reported to generate a Gaussian beam light-sheet with an axial FWHM of 410 ± 10 nm [17]. The main drawback of using high NA illumination in SPIM is the limited FOV in y -direction, which was derived in equation 2.17. In fact, the thin light-sheet in the example has a reported Rayleigh range as short as $1.9 \mu\text{m}$ and thus a FOV limited to $3.8 \mu\text{m}$. For most biological structures a larger FOV is required, which in turn lowers the axial resolution of the conventional SPIM setup.

An approach to overcome the compromise between a large FOV and axial resolution in SPIM makes use of scanned Bessel beams for diffraction-limited excitation with a thin virtual light-sheet. Bessel beams are so called self-reconstructing beams [40] and known for many decades [27]. In contrast to the hyperbolic shape of Gaussian beams, the width of the central spot of a single Bessel beam cross section can be regarded as constant over a relatively large distance along the optical axis. For this reason, Bessel beams have been successfully applied in SPIM setups for homogeneous light-sheet illumination over a large FOV [33, 32, 114, 39]. Bessel-beam light-sheets generated with an illumination NA of 0.34 that feature a Rayleigh range of $50 \mu\text{m}$ have been reported [33]. The main drawback of Bessel beam excitation is the energy the beam disposes by its side lobes [26]. These add up during the scan and broaden the light-sheet in the axial direction. As a consequence, fluorescent markers are illuminated not only within the central part of the light-sheet cross-section, but also away from the focal plane. The additional light dose contributes to photobleaching and phototoxic effects outside of the focal plane of detection. In fact, scanned Gaussian beams are reported to be superior to scanned Bessel beams in terms of photobleaching caused by the excitation light [114]. Two-photon Bessel-beam excitation for reduced side lobes in combination with a structured illumination-based approach was reported to result in a near-isotropic, diffraction-limited resolution of about 300 nm [114]. The main disadvantage of this method is the longer data acquisition time and the reduced contrast due to the background fluorescence generated by the remaining side lobes. The combination of Bessel-beam light-sheet excitation and a method called super-resolution structured illumination microscopy (SR-SIM) [52] improved the contrast in images of thick biological samples [39]. The axial resolution, however, was not further increased.

2.5 Optical nanoscopy

All the aforementioned techniques are, due to diffraction, limited in their ability to spatially resolve features that are located at a distance closer than about

half the wavelength of the utilized light. In 1994, for the first time, a fundamental idea and practicable concept was introduced that describes how the diffraction limit in fluorescence microscopy can be broken with propagating light using standard lenses [68]. Five years later, the first realization of this concept in form of a STED microscope has finally proven that a spatial resolution beyond the diffraction barrier can indeed be achieved also in the far-field [93]. Since then, multiple super-resolution methods have emerged which all base on the same concept and mainly differ in their theoretical and experimental complexity, the achievable resolution, and biocompatibility. They are called optical nanoscopes. This section gives an overview of the basic principle that enables an at least conceptual increase in resolution of a lens-based light microscope to the molecular scale or even beyond. A focus is set on the RESOLFT instruments relevant for this thesis.

2.5.1 The concept of breaking the diffraction barrier

All optical nanoscopy techniques that have been realized up to now separate otherwise indistinguishable fluorophores by *switching* them in a light-controlled manner between two discernible states, i.e. a signaling on-state and a non-signaling off-state. The switching process is used to separate signals originating from on-state fluorophores in time. As a consequence, they can be sequentially recorded. If their coordinate is known, the recorded signals can be assembled to an image with a resolution below the limit set by diffraction.

The pool of possible states and their transitions is large [65, 63, 61, 64]. Exploiting transitions between the basic electronic states, such as the singlet ground S_0 and excited state S_1 and the triplet state T_1 , but also between charged states, chemical states, and conformational states has led to numerous realizations of the described concept. Multiple powerful optical nanoscopy techniques have been developed in the last two decades. According to the way the switching and readout it performed, these techniques can be classified in RESOLFT microscopy and SMS microscopy. For completeness a short overview of the later is given. Then, the RESOLFT techniques are discussed in detail.

2.5.2 Single marker switching techniques

Stochastic SMS microscopes, switch a small subset of fluorescent markers between a signaling and a non-signaling state in a stochastic manner and thus randomly in space. Having recorded the signals originating from the active subset, the fluorophores are switched off again or bleached and the next randomly distributed subset is activated in the sample and readout. The separation and localization procedure is repeated many times. The image ac-

quisition ends when ideally all fluorescent markers in the sample have been switched on at least once and have contributed to the final image [73]. If the subset of on-state markers is sparse enough to clearly separate their diffraction-limited fluorescence spots on the detector, their actual position is then estimated by mathematical post-processing, typically, by fitting a 2D Gaussian function to the intensity distribution of each single spot [136, 116]. The localization precision is dependent on the number of photons detected from a fluorophore during the exposure time of the detector and the background signal of the image [146]. The super-resolution image in the stochastic switching and readout regime is obtained by plotting a histogram of estimated positions on a sampling grid. The first realizations of SMS microscopy were photoactivated localization microscopy (PALM) [13] and stochastic optical reconstruction microscopy (STORM) [121]. These techniques only work with a limited number of fluorophore species such as photoactivatable or photoswitchable proteins or photochromic compounds. ground state depletion followed by individual molecule return (GSDIM) [36] or direct STORM (dSTORM) [56] extend the concept to conventional organic fluorescent markers. Also quantum dots have been used as markers in SMS microscopes [71]. Typical SMS microscopes routinely achieve lateral resolutions in the focal plane of 30 nm, which is approximately a 8-fold improvement as compared to wide-field microscopes. Recently, the position of a single emitter has been estimated with an accuracy below 10 nm in all spatial directions [134]. One of the major drawbacks of all SMS techniques is their very low throughput since molecules are likely to be excited several times. Long data-collection times limit their application for fast developing living specimen.

2.5.3 RESOLFT techniques

In RESOLFT techniques the center of the region where a detectable signal is generated is known at any time during image acquisition. It is predefined at coordinate z_0 by applying an appropriate light pattern that features one or multiple intensity zeros. Typically, the peak of the excitation intensity distribution overlaps with the intensity zero of the off-switching light pattern. This pattern then switches the fluorophores in the surrounding of z_0 to a non-signaling state and keeps them in this state during the time of readout at z_0 , even if they are still illuminated with excitation light. Only few fluorescent markers within a small region around z_0 remain in the signaling on-state and contribute to the signal.

The concept of RESOLFT has been realized in numerous microscopy techniques, which mainly differ in the reversible optical transitions they use [61, 66, 70]. The first and most prominent example is STED[68], which uses the most basic transition between the fluorescent singlet state S_1 and the ground state S_0 to achieve sub-diffraction resolution. SPEM[59], also called SSIM[50],

employs the same basic states. GSD[67] makes use of transitions between the singlet state and a long-lived non-signaling triplet state.

The main advantage of RESOLFT is that the acquired raw data already contains sub-diffraction spatial information. As a consequence, super-resolution images are obtained without any mathematical post-processing such as filtering, fitting and plotting. Moreover, in multicolor RESOLFT imaging, signals originating from the same zero-intensity position of the illumination light pattern are aligned by design. This is especially interesting for experiments where colocalization of various objects is studied. Another advantageous aspect of the RESOLFT concept is the broad range of fluorescent markers that can be used. In principle there are no restrictions in the selection of fluorophore species. A significant improvement of resolution has been achieved with synthetic dye markers as well as FPs. A RESOLFT technique that uses members of the RFP family as fluorescent markers is presented in this thesis.

2.5.3.1 Creation of off-switching patterns by phase modulation

In RESOLFT nanoscopes, the light pattern featuring at least one intensity-zero can be generated by a standing wave [59, 70] or by manipulating the phase of the wavefront of the switch-off laser beam before it hits the back-focal plane of the illumination objective lens [85, 84]. In a majority of current RESOLFT setups phase plates are implemented to manipulate the incoming beam. Depending on the optical realization of the RESOLFT concept, different phase plate types can be inserted into the beam path. Figure 2.9 shows the sketch of two prominent examples together with their orthogonal cross-sections through the center of the resulting light distribution.

In RESOLFT setups that aim for a resolution improvement in one dimension, the zero-intensity profile is generated with a so called half-moon phase plate. It is often implemented with two 10 mm thick glass flats mounted side-by-side with one flat being tilted about an axis perpendicular to the touching faces. This assembly as a whole can be tilted about the same axis. The off-switching beam passes through the optic axis which passes both the touching faces and the axis of tilt. For a fixed relative angle of the flats, a particular common tilt angle can be found such that the phase of one half of the incident beam is retarded by π relative to the other half as depicted in figure 2.9a. During focusing each radial position of the beam cross section interferes destructively with its mirror-counterpart on the other half of the beam. Linearly polarized light in the direction parallel to the mid-line of the phase plate halves theoretically results in a absolute zero-intensity line. Light polarized perpendicular to the mid-line fills up the zero-intensity region and reduces the brightness of the image by switching off fluorophores that are supposed to contribute to the signal. As shown in the orthogonal slices through the resulting PSF, the zero-pattern is not limited to the focal plane but rather ranges to infinity along the axial direction.

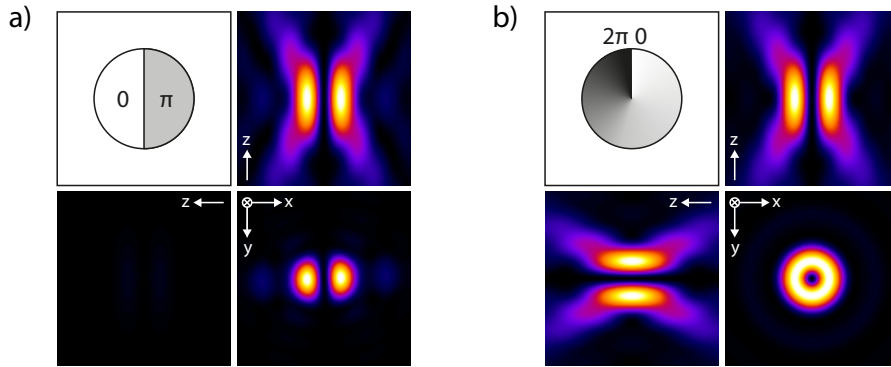


Figure 2.9: Two well-established RESOLFT phase plates and the simulation of the resulting light intensity pattern. a) A half-moon phase plate retards the phase of one half of the incident beam by π relative to the other half. In the focal plane an illumination pattern with a zero-intensity line is created that leads to a resolution improvement in one dimension. b) RESOLFT setups aiming for improved resolution in both lateral dimensions typically use a toroidal shaped illumination pattern that is created in the focal plane by transmission through a vortex phase plate.

Point-scanning RESOLFT techniques typically use a 2D switch-off pattern in the object focal plane to achieve resolution enhancement in both lateral dimensions [66, 64]. The most practical shape of such a pattern has a radial symmetry in the x - y plane and is extended in the axial direction. It can be generated by shifting the phase of a circularly polarized incident wavefront in a full helical turn continuously from 0 to 2π , e.g. with a vortex phase plate depicted in figure 2.9b. Due to destructive interference of all radial mirror-parts of the beam cross-section, the focal spot has a central zero-region. It is surrounded by a toroidal intensity distribution that resembles a doughnut. Vortex phase plates are typically made of a glass substrate that is coated with a polymer or MgF_2 . The thickness of the coating defines the phase difference that is applied to the transmitted beam.

The switch-off light patterns applied in RESOLFT nanoscopy so far have a zero- or one-dimensional intensity zero region. In this thesis, a technique is presented that makes use of a pattern with a 2D zero-intensity area.

2.5.3.2 Theory based on a two-state model

In the following, a general expression for the resolution of RESOLFT microscopes is derived on the basis of a two-state model [65, 61, 152, 54]. Let us imagine a fluorophore with two distinct states, a bright signaling state A and a dark non-signaling state B , as depicted in figure 2.10a. The transition from A to B is driven by light and occurs with a rate $k_{AB} = \gamma \sigma_{AB} I_{AB}$, where σ_{AB} is the cross-section of the transition process, $\gamma = \lambda/hc$ is the inverse photon energy with the wavelength λ , the vacuum speed of light c and the Planck's

constant h , and I_{AB} is the light intensity that drives the transition. The reverse transition from B to A with a rate k_{BA} can also be induced by light or by any other process such as a chemical or thermal reaction. The relative population of A and B , in the following referred to as N_A and N_B , change over time t and can be expressed in a differential equation by

$$\frac{dN_A}{dt} = -\frac{dN_B}{dt} = -k_{AB} N_A + k_{BA} N_B. \quad (2.18)$$

Because of particle conservation, the relative populations add up to one, i.e. $N_A + N_B = 1$. Without loss of generality, we can assume that all fluorophores are initially in the signaling state A . The solution of equation 2.18 is then

$$N_A(t) = \frac{k_{BA}}{k_{AB} + k_{BA}} + \frac{k_{AB}}{k_{AB} + k_{BA}} e^{-(k_{AB} + k_{BA})t}. \quad (2.19)$$

This general equation can be simplified by approximations suitable for the applied mechanism of molecular switching. In the case of RESOLFT experiments with RSFPs as shown in this thesis, states A and B are long-lived states. The transition from B to A is thus mainly light-driven so that its rate can be well approximated by $k_{BA} = \gamma \sigma_{BA} I_{AB}$. Equation 2.19 is rewritten using the definitions of the transition rates k_{AB} and k_{BA} leading to

$$N_A(t) = \frac{\sigma_{BA}}{\sigma_{AB} + \sigma_{BA}} + \frac{\sigma_{AB}}{\sigma_{AB} + \sigma_{BA}} e^{-\gamma(\sigma_{AB} + \sigma_{BA}) I_{AB} t}. \quad (2.20)$$

One can see that for an applied light energy $\gamma I_{AB} t \gg (\sigma_{AB} + \sigma_{BA})^{-1}$, the relative population N_A reaches an equilibrium state $N_A^\infty = \sigma_{BA} (\sigma_{AB} + \sigma_{BA})^{-1}$. The efficiency of the off-switching process thus solely depends on the ratio of the cross-sections. Ideally, the wavelength of the continuous wave light that drives the transition from A to B is chosen such that the wavelength-dependent cross-sections relate as $\sigma_{AB} \gg \sigma_{BA}$. In this case, the residual fluorescence of the equilibrium state can be neglected. The relative population of state A is then given by

$$N_A = e^{-k_{AB} t} = e^{-\gamma \sigma_{AB} I_{AB} t}. \quad (2.21)$$

It can be deduced from this equation that principally all on-state fluorophores can be switched to their off-state. For a certain fixed illumination time $t = t_{off}$, the remaining fraction of on-state fluorophores only depends on the applied light intensity I_{AB} . A characteristic light intensity can be defined at which one half of the on-state population N_A is switched to the off-state B . This intensity is called the saturation intensity I_{sat} and is here expressed as

$$I_{sat} := \frac{\ln 2}{\gamma \sigma_{AB} t_{off}}. \quad (2.22)$$

I_{sat} can be considered as the intensity that is required to outperform the competing reverse transition to the on-state. Inserting definition 2.22 in equation 2.21 leads to the expression

$$N_A(I_{AB}(z)) = e^{-\ln 2 \frac{I_{AB}(z)}{I_{sat}}}. \quad (2.23)$$

For a fixed t_{off} , the ratio between the driving intensity distribution I_{AB} with its maximum intensity I and I_{sat} influences N_A and N_B as shown in figure 2.10b. For $I \gg I_{sat}$ virtually all fluorophores are switched to state B .

In the RESOLFT-SPIM setup presented in this thesis, the fluorophores are switched to state B with an off-switching pattern featuring an intensity zero at z_0 that is centrally aligned to an excitation light distribution. The remaining distribution of on-state fluorophores at time t_{off} forms the so-called effective PSF h_{eff} with a peak position at z_0 . It is calculated by the point-wise product of the normalized diffraction-limited excitation PSF h_{exc} and the relative on-state population at a time t_{off} :

$$h_{eff}(z, I) = h_{exc}(z) \cdot N_A(h_{off}(z) I t_{off}), \quad (2.24)$$

where $h_{off}(z)$ is the normalized off-switching intensity distribution. The axial resolution of the RESOLFT-SPIM microscope is defined as the FWHM Δz of the effective PSF. In order to derive an expression for Δz , the excitation PSF is approximated by a Gaussian with a FWHM d_z along the z -axis in the illumination focal plane:

$$h_{exc}(z) = e^{-4 \ln 2 \left(\frac{z}{d_z}\right)^2}. \quad (2.25)$$

The relative on-state population at a position z in the sample depends on the off-switching intensity distribution at this position, which can be well approximated by a parabola at regions close to z_0 [35]:

$$h_{off}(z) = 4 a^2 z^2. \quad (2.26)$$

Here a is a parameter that depends on the NA and the wavelength used for illumination. Together with equations 2.23, 2.25, and 2.26 we can calculate the effective PSF in equation 2.24 as

$$\begin{aligned} h_{eff}(z, I) &= e^{-4 \ln 2 \left(\frac{z}{d_z}\right)^2} \cdot e^{-4 \ln 2 a^2 \frac{I}{I_{sat}} z^2} \\ &= e^{-4 \ln 2 \left(\frac{1}{d_z^2} + a^2 \frac{I}{I_{sat}}\right) z^2}. \end{aligned} \quad (2.27)$$

As it can be seen from this equation, the effective PSF has again a Gaussian shape. Its FWHM is then derived to

$$\Delta z = \left(\frac{1}{d_z^2} + a^2 \frac{I}{I_{sat}} \right)^{-1/2} = \frac{d_z}{\sqrt{1 + d_z^2 a^2 I / I_{sat}}}. \quad (2.28)$$

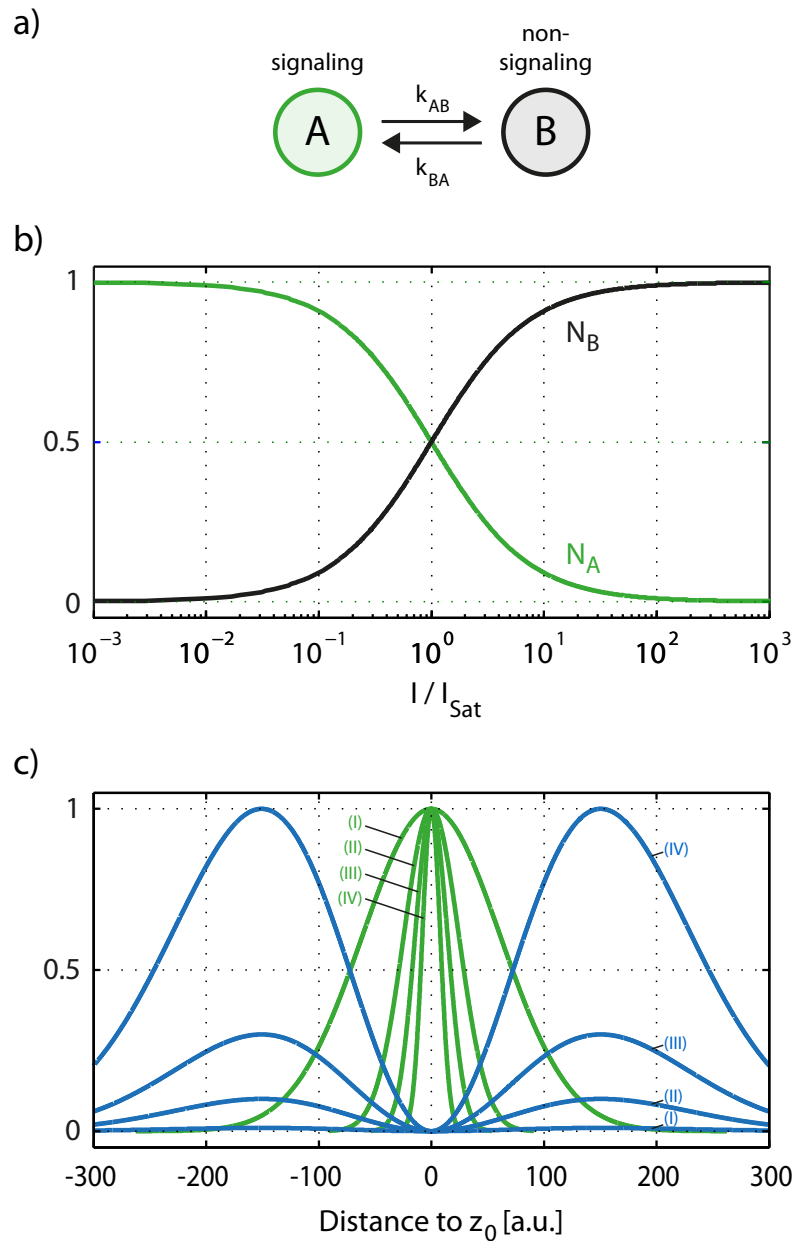


Figure 2.10: Simple two-state model with a signaling state A and a non-signaling state B . a) Initially all molecules are in state A . The transition from A to B is driven by light. b) The relative population of state A (N_A) and B (N_B) depends on the applied light intensity that drives the transition from A to B . c) The resolution of a RESOLFT microscope is increased by spatially limiting the number of fluorophores in state A with light. The FWHM of the remaining spot can be controlled by changing the ratio of I and I_{sat} . Here, curves with the following parameters are shown: (I) $I = I_{sat}$, (II) $I = 10 I_{sat}$, (III) $I = 30 I_{sat}$, (IV) $I = 100 I_{sat}$. Some parts of the figure have been redrawn from reference [69].

In figure 2.10c the dependency of Δz on the ratio of I and I_{sat} is illustrated. The FWHM of the effective PSF clearly reaches sub-diffraction dimensions for intensities $I \gg I_{sat}$.

According to equation 2.28, infinitely high resolution can be obtained in theory. In practice, however, the achievable resolution critically depends on the photophysical and photochemical properties of the fluorophores used. While the number of required photons for a super-resolution image based on RESOLFT can theoretically be as low as one, the number of switching cycles the fluorophores undergo without contributing to the imaging signal during image acquisition is high. For an m -fold resolution improvement in one dimension, a fluorophore needs to cycle approximately m times. The number of cycles is raised to a higher power when more dimensions with increased resolution are required. In the worst case, fluorophores suffer from switching fatigue and cannot contribute to the signal anymore. Typically, the lateral resolution in images of biological structures resolved with a standard STED microscope, the prototype of a RESOLFT microscope, ranges from 20 to 40 nm [47, 43, 21]. The highest lateral resolution of just a few nanometers has been reported for individual diamond nitrogen vacancy centers inside a solid immersion lens [154].

2.5.3.3 RESOLFT with switchable proteins

Light-structuring techniques like STED and saturated structured illumination microscopy (SSIM) [50] typically apply light intensities in the range of MW/cm² to GW/cm² to effectively switch off a large region. Especially when imaging delicate samples where photoinduced changes need to be avoided, these techniques are preferably realized with fluorophores that lead to the same factor in resolution improvement at much lower light intensities. The class of reversibly switchable fluorescent proteins introduced in section 2.1.2 poses a highly suitable species of fluorophores for this purpose. The transition between the metastable on- and off-state of these markers requires a saturation intensity I_{sat} of about 5 orders of magnitude lower than the typical on-off transition used in SSIM or STED. Moreover, the suitable spectral properties, fast switching kinetics, and high photostability of recently developed yellow-green emitting RSFPs like rsEGFP [45], rsEGFP2 [46], Dronpa M159T [145, 140] and Dreiklang [15] compared to early RSFPs have enabled RESOLFT nanoscopy in living cells or tissues. In order to further reduce the imaging time, methods have been reported which parallelize the conventional point-scanning RSFP-based RESOLFT technique. An approach using a one-dimensional standing-wave pattern [128, 118] could achieve a lateral resolution of less than 50 nm but requires additional rotation of the pattern [118], which slows down the imaging speed. Parallelization of the RSFP RESOLFT concept with an illumination pattern having more than 100,000 intensity minima enabled imaging of large fields (up to 150 μm) within a few

seconds and in principle unlimited lateral resolution [20]. In this example, the slower switching variant of rsEGFP has been used. Novel red-emitting RSFPs enabled multi-channel RESOLFT images and colocalisation studies by using two spectrally distinct RSFPs [99]. A two-color RESOLFT approach with the novel RSFP rsCherryRev1.4 in combination with yellow-green emitting RSFPs has been demonstrated in a point-scanning and a parallelized manner.

2.5.4 Imaging with sub-diffraction axial resolution

In their first implementation, most of the imaging techniques discussed in the previous sections have provided resolution improvements mainly in the lateral direction. Setups that push the axial resolution below the diffraction limit have been developed more recently. One example is the 4Pi microscope that coherently uses two opposing lenses [62, 51, 10, 28, 29]. It requires external control of the phase of the counter propagating waves and data post-processing to remove interference effects. 4Pi microscopy can be combined with STED [126] or SMS microscopes [134, 8, 157] to further improve the resolution [60]. In a single lens 3D STED approach, an annular phase plate creates a relatively low-intensity toroidal lateral pattern with additional high-intensity lobes above and below the central minimum [94]. To get a more balanced intensity distribution, the annular phase plate is often implemented in combination with a vortex phase plate [58, 55, 153]. Recently, a three-dimensional segmented wave plate has been developed mainly for the reason of compactness of the setup [119]. Stochastic methods make use of multi-focal planes [74, 82] or additional optics that break the axial symmetry of the detection PSF [83, 74, 112]. A 3D structured illumination microscopy (SIM) method which doubles the lateral and axial resolution with true optical sectioning has been presented in 2008 [52]. So far, no approach increasing the axial resolution of a RSFP-based RESOLFT setup has been reported, yet.

In general, super-resolution methods that improve the axial resolution of a microscope are often limited in their routine application in biological research. The main reasons are found in the technical complexity and increased photobleaching, especially for single lens based imaging techniques.

The RESOLFT concept in form of a STED-based realization has been used to break the diffraction barrier along a light-sheet's detection axis. In 2011, a Gaussian excitation beam was overlapped with a double-sheet depleting laser beam on either side of the focal plane to perform on/off switching [38]. Due to scattering and possibly additional aberrations caused by the difference between excitation and STED lasers wavelength, the maximal achievable resolution in biological specimen was limited even in fixed samples. The stained actin network of a fixed zebrafish was imaged at a relatively slow rate of 2 Hz with an increase in resolution by 30% axially and 17% laterally compared to the conventional light-sheet mode. A successful application of STED-SPIM to live cells or living organisms has not been reported.

In a very recent and only theoretical approach the combination of STED-SPIM with Bessel-beam illumination was proposed [158]. According to the reported simulations an increase in axial resolution by a factor of 4.8 compared to the conventional SPIM microscope is achievable with an average depletion power of 1 W. However, if highly sensitive cellular structures and their subtle changes are to be examined, then any potential disturbances of the structure and its physiological environment should be avoided. The high average STED laser power required for substantial sub-diffraction resolution with this technique provides strong incentives for developing a coordinate-targeted approach for low-power operation. A solution is presented in the following.

RESOLFT-SPIM

In this chapter, a new far-field fluorescence microscopy technique is presented, that combines the advantages of RSFP-based RESOLFT nanoscopy and SPIM. It offers sub-diffraction axial resolution for a RESOLFT nanoscope employing RSFPs as fluorescent markers. At the same time, it improves the axial resolution with respect to conventional light-sheet microscopy by reducing the light-sheet thickness below the diffraction limit. The basic concept of RESOLFT-SPIM is explained in the first section of this chapter. Then, the optical setup is described in detail along with setup-specific alignment strategies. Thereafter, the setup is characterized especially in terms of its resolving power, the available FOV and the resolution in dense samples. Finally, the imaging capabilities of RESOLFT-SPIM are demonstrated in biological applications in comparison to conventional SPIM.

3.1 Basic concept

In this thesis a new far-field fluorescence microscopy technique is presented. It exploits the super-resolution imaging capabilities of RSFP-based RESOLFT together with the optical sectioning properties of SPIM, and is therefore called RESOLFT-SPIM. It makes use of long-lived dark and fluorescent states provided by reversibly switchable fluorophores to gain sub-diffraction axial resolution with light intensities of several orders of magnitude lower than in STED. In combination with SPIM, a light-sheet with an effective thickness below the diffraction limit enables detailed non-invasive imaging of living specimens in three dimensions without disturbing their physiological environment.

The new RESOLFT-SPIM concept is illustrated in figure 3.1. Let us assume a living specimen, for example a cell, that grows on a coverslip attached to a movable platform in the RESOLFT-SPIM microscope. The specimen expresses fusion proteins composed of at least one RSFP and a target protein. The illumination of the sample is placed at a right angle to the detection as it is usually implemented in SPIM setups. A Gaussian activation laser is focused by a cylindrical lens into the back-aperture of an illumination objective. As a consequence, a light-sheet is formed which ideally coincides with the focal plane of the detection objective. The laser light activates RSFPs in a small volume around this focal plane. In the sketch, these RSFPs are marked with white dots. The thickness of the activated area is dependent on the NA of

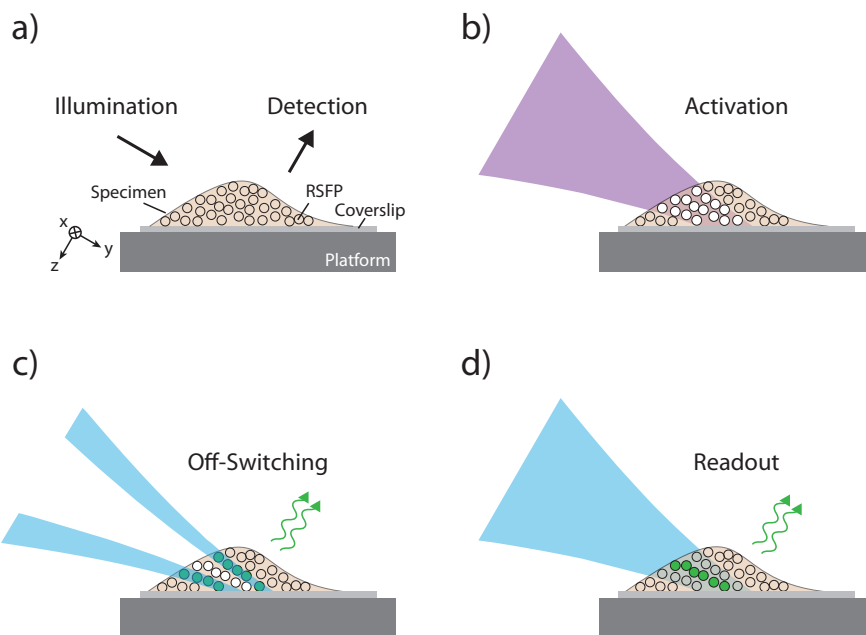


Figure 3.1: The RESOLFT-SPIM concept. a) A living specimen expressing RSFPs is grown on a coverslip, which was mounted on a movable platform. The specimen is illuminated perpendicular to the detection axis. b) RSFPs in a thin section of the sample are switched from their initial off-state to the on-state by an activation light-sheet. None of the fluorophores outside the illuminated volume is affected by the laser light. c) A light-sheet featuring a central zero-intensity plane effectively switches off activated RSFPs above and below the detection focal plane. For negative switching RSFPs, this is a competing process to fluorescence (green arrows). Applying off-switching light intensities above the saturation intensity of the RSFPs, only fluorophores within a slice of sub-diffraction thickness remain activated. d) They can be readout by a third light-sheet and contribute to the RESOLFT-SPIM image. Then, the platform is moved to the next scan position for another illumination cycle.

the illumination objective. Regions outside the illuminated volume above and below the focal plane are not activated. After a short exposure with the first laser, a second Gaussian laser beam with a slightly red-shifted wavelength is focused by the same cylindrical and objective lens into the sample. With a half-moon phase plate, the second order transversal Gaussian mode is generated. Consequently, the light-sheet features a two-dimensional zero-intensity area. Ideally, both laser beams exactly overlap so that the plane of maximal exposure with the activation laser coincides with the intensity minimum of the second laser. At positions in the sample where the off-switching intensity is larger than the saturation intensity of the RSFPs, it is most likely that activated RSFPs are switched to the deactivated state. In a negative switching mode, fluorescence is stimulated by the same wavelength which also deactivates the RSFPs. Since this emitted light mainly originates from out-of-focus

regions it is ideally not detected by the wide-field setup. After the deactivation process, only a thin layer around the focal plane remains activated. Its thickness is dependent on the off-switching laser intensity applied to the sample according to the considerations in section 2.5. In a third illumination step, the remaining activated RSFPs are readout by a Gaussian TEM₀₀ light-sheet with a photon energy that excites the fluorophores, i.e. equal or similar to that of the second laser. Fluorophores in a volume with an axial extent below the diffraction limit emit fluorescence light and contribute to the image-forming signal. Ideally, after several excitation and emission cycles leading to a high signal to noise ratio in the image, the fluorophores are switched back to the deactivated state. These illumination processes are repeated for each plane of the sample, that is stepwise moved through the stationary light-sheets. An image stack is built up containing detailed 3D information about the specimen with in principle diffraction-unlimited resolution.

3.2 Optical implementation

This section describes the technical realization of the RESOLFT-SPIM concept. First, the optical layout is shown and explained. Then, the control of the electronic devices in the setup is described. At the end of this section, the alignment strategies together with new setup specific alignment tools are presented.

3.2.1 Optical layout

The concept of RESOLFT-SPIM has been realized in a novel optical setup. It consists of four essential parts: an illumination unit, a detection unit, a specimen chamber and a stage scanner. In the following, each of these parts is described in detail. In addition, the objective arrangement is motivated. Figure 3.2 shows a schematic drawing of the essential optical components and the beam paths of the new setup.

3.2.1.1 Illumination unit

For illumination, three fast switching¹ continuous-wave diode lasers are implemented. Their wavelengths are adapted to the spectral properties of the recent RSFPs called rsEGFP, rsEGFP2, rsEGFP(N205S), and Dronpa-M159T. For activation a UV laser (iBeam Smart 405-60, Toptica, Germany) with a wavelength of 405 nm and a maximal power of 60 mW is used. In the following this laser is referred to as the activation laser. The second diode laser emits at a wavelength of 488 nm (iBeam Smart PT488-50, Toptica Photonics, Gräfelfing, Germany). It is implemented to generate the off-switching

¹ The rise- and falltime of the laser enable signal is below 1 μ s.

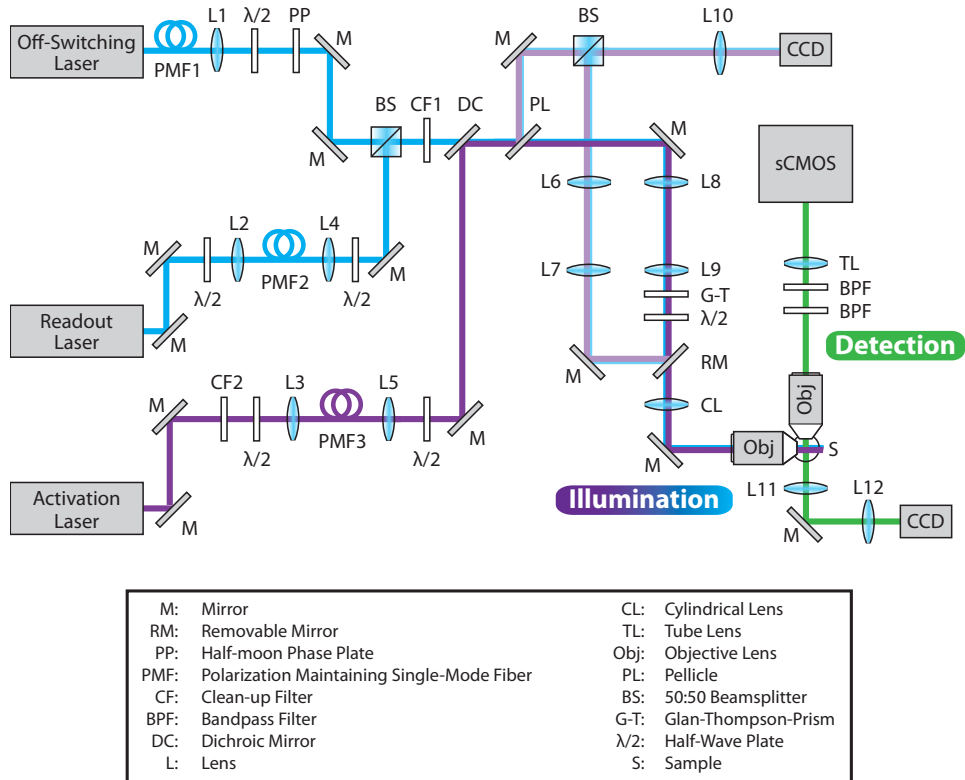


Figure 3.2: Diagram of the optical components and the beam paths of the RESOLFT-SPIM setup. Three fiber-coupled continuous-wave diode lasers are used for activation (purple), off-switching, and readout (both blue) of RSFPs. The off-switching light pattern is generated by a half-moon phase plate (PP) in the beam path of the off-switching laser. A cylindrical lens (CL) focuses the combined and extended laser beams into the back-focal plane of the illumination objective. Light sheets are formed and illuminate the sample (S). Fluorescence (green) is collected by an objective lens perpendicular to the illumination axis, filtered by two bandpass filters (BPF) and imaged with a tube lens (TL) onto an sCMOS camera. A CCD camera records the cross-sections of the laser beams if a pellicle (PL) and a removable mirror (RM) are inserted in the beam path. Another CCD camera images the light-sheets perpendicular to both objective axes.

light pattern in the sample and is in the following called the off-switching laser. It has a maximal output power of 50 mW. After the off-switching process, the remaining activated RSFPs are read out with a third laser (LuxX 488-60, Omicron-Laserage, Rodgau, Germany), in the following referred to as the readout laser with a nominal wavelength of 488 nm and a maximal power of 60 mW. The lasers are spectrally cleaned with narrow bandpass filters (CF1: FF02-482/18-25, CF2: FF01-406/15-25, Semrock, Rochester, NY). For distortion-free Gaussian light-sheets, the beam profiles of all three lasers are cleaned up by sending the light through single-mode fibers. Only the off-switching laser has been directly fiber coupled by the manufacturer. The activation and the readout lasers are coupled into polarization maintaining single-mode fibers (PMF2, PMF3: PM460-HP, Thorlabs, Newton, NJ) with achromatic lenses ($f_{L2}, f_{L3} = 10$ mm). The coupling efficiency was about 60% for either laser. Half-wave plates adjust the polarization of each laser to the fast axis of the utilized fiber.

At the fiber output, the beam diameter of each laser is independently controlled with achromatic lenses ($f_{L1} = 13$ mm, $f_{L4} = 13$ mm, $f_{L5} = 16$ mm). Potential longitudinal chromatic aberrations in the focal plane can thus be compensated by slight defocussing of these lenses. The off-switching intensity pattern is generated by a half-moon phase plate that is placed in the path of the collimated off-switching laser beam (cf. figure 3.3). It consists of two quartz blocks mounted in parallel on a multi-axis positioner (LP-1A, Newport Corporation, Irvine, CA). The blocks are tilted with respect to each other to generate a phase difference between the beam halves. Figure 3.3b illustrates their implementation in the setup. The modified beam is subsequently combined with the beam path of the readout laser by a 50:50 beam splitting cube (BS013, Thorlabs, Newton, NJ). A dichroic mirror (Di02-R442, Semrock, Rochester, NY) merges the expanded UV beam with the readout and the off-switching laser. A common home-built beam expander consisting of two achromatic lenses ($f_{L8} = 60$ mm, $f_{L9} = 200$ mm) adjusts the beam widths to the pupil diameter of the water-dipping illumination objective.

The polarization state of the laser beams is controlled by a Glan-Thompson prism (G-T: PGT 1.10, B. Halle, Berlin, Germany) and a half-wave plate ($\lambda/2$). Additional half-wave plates are placed at each fiber output in order to maximize the transmission of the laser lines through the Glan-Thompson prism. In the setup, the polarization is oriented parallel to the focal plane of the detection since the zero-intensity area of the off-switching pattern is very sensitive to polarization. Vector components oriented perpendicular to the light-sheet fill up the zero-intensity area. Also the polarization of the activation and the readout lasers are adjusted to the light-sheet plane in order to increase the probability that the same similarly oriented dipoles are addressed. As a bonus, light-sheets that are linearly polarized parallel to the focal plane are up to 5% thinner.

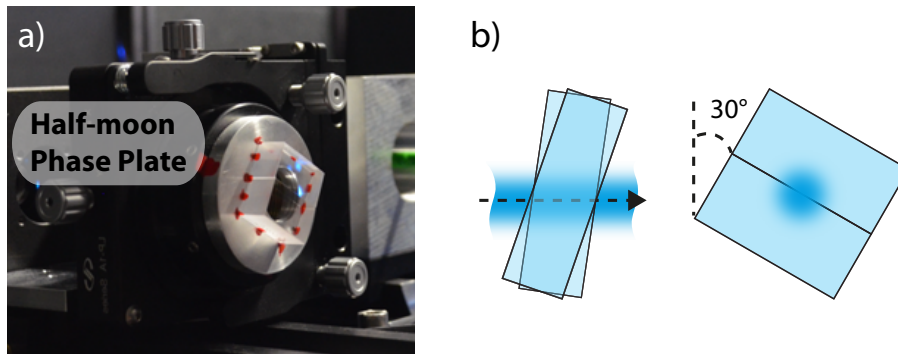


Figure 3.3: Mounting and positioning of the half-moon phase plate. a) The half-moon phase plate consisting of two glass flats mounted side-by-side with one flat being tilted about an axis perpendicular to the touching faces. This assembly as a whole can be tilted about the same axis. b) The off-switching beam passes through the optic axis which passes both the touching faces and the axis of tilt. For a fixed relative angle of the flats, a particular common tilt angle can be found such that the phase of one half of the incident beam is retarded by π relative to the other half. The phase plate is rotated by 30° to account for the angle of the illumination objective.

A cylindrical lens ($f_{CL} = 150$ mm) focuses the collinear beams into the back-aperture of the illumination objective, which then generates a light-sheet at an angle of $\beta = 30^\circ$ with respect to the horizontal plane. Additional beam paths for alignment are shown in the diagram in figure 3.2. They can be accessed with a removable mirror (RM) and a pellicle (PL: BP145B1, Thorlabs, Newton, NJ). Their purpose is explained in section 3.2.3.

3.2.1.2 Arrangement of objective lenses

As described before, the illumination objective generates a light-sheet that encloses an angle of 30° with the horizontal plane. The detection objective is oriented perpendicular to the x - y plane of the light-sheet and consequently has an angle of 60° with respect to the specimen. The angle has been chosen such that for any commercially available water-dipping detection objective lens the maximum aperture can be used for collection of fluorescence light. Also, undesired artifacts potentially caused by direct reflections of the illumination laser light on the surface of the coverslip are reduced.

Figure 3.4 illustrates the geometric arrangements of potential illumination and detection objectives for RESOLFT-SPIM. All objective lenses considered here are made for water-dipping applications. Their internal optics are corrected for aberration-free light transition in water-based medium with a refractive index close to 1.333. If a biological specimen requires a comparably large FOV, a 10x illumination objective lens with an NA of 0.3 is preferred. In the RESOLFT-SPIM setup, it can be combined with any other water-dipping detection objective lens with an NA of less or equal to 0.8 without further

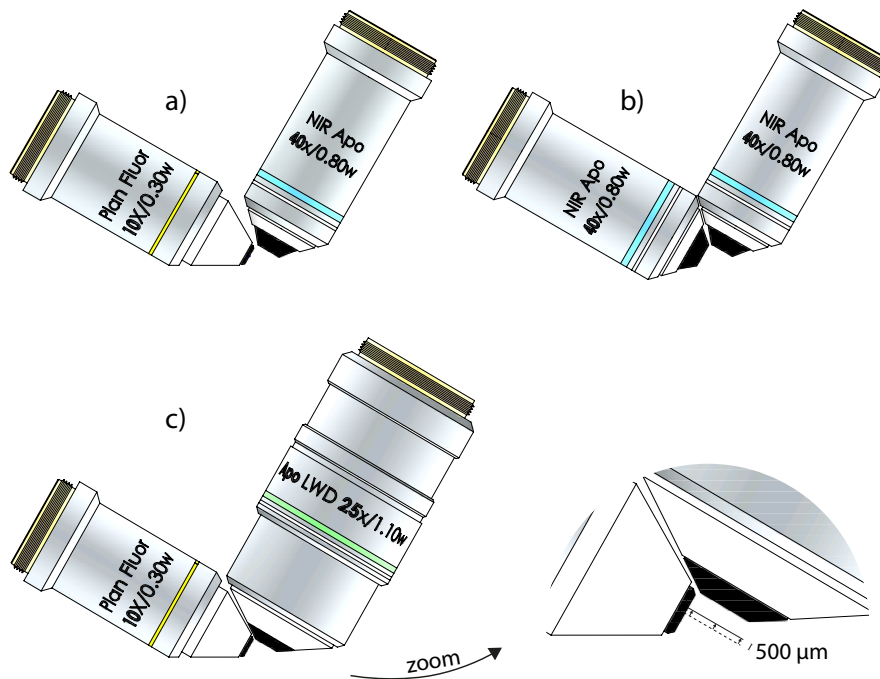


Figure 3.4: Possible combinations of objective lenses for RESOLFT-SPIM. a) A 10x/0.3 NA illumination objective lens generates a light-sheet with a comparably large FOV. In this thesis, it is used in combination with a 40x/0.8 NA objective lens for biological applications. b) A combination of two 40x/0.8 NA objective lenses is preferably used for alignment and the characterization of the setup. It creates the thinnest diffraction-limited light-sheet for reasonably high detection NA. c) A 25x/1.1 NA detection objective lens can in principle be used in combination with low NA illumination. Due to geometry constraints, an offset of the light-sheet is needed so that it coincides with the detection focal plane.

considerations (cf. figure 3.4a). Due to geometry constraints, the highest possible NA for illumination is set to 0.8 for a reasonably high detection NA of 0.8. Figure 3.4b shows a simulation of this objective arrangement. For an illumination focal point in the center of the detection focal plane, the objectives are almost touching. This arrangement is advantageous over low NA illumination, if samples in a small volume need to be imaged with high intensities. Even in the conventional SPIM mode this combination provides higher axial and (in some cases) lateral resolution than a confocal microscope [30]. Both combinations are used in this thesis. Recently, a 25x/1.1 NA detection objective has become available. If this objective lens is positioned as close as possible to any illumination objective, a light-sheet created on axis does not coincide with the detection focal plane. In order to still use this high NA objective in combination with a 10x/0.3 NA illumination objective lens in the RESOLFT-SPIM setup, the detection objective needs to be moved upwards

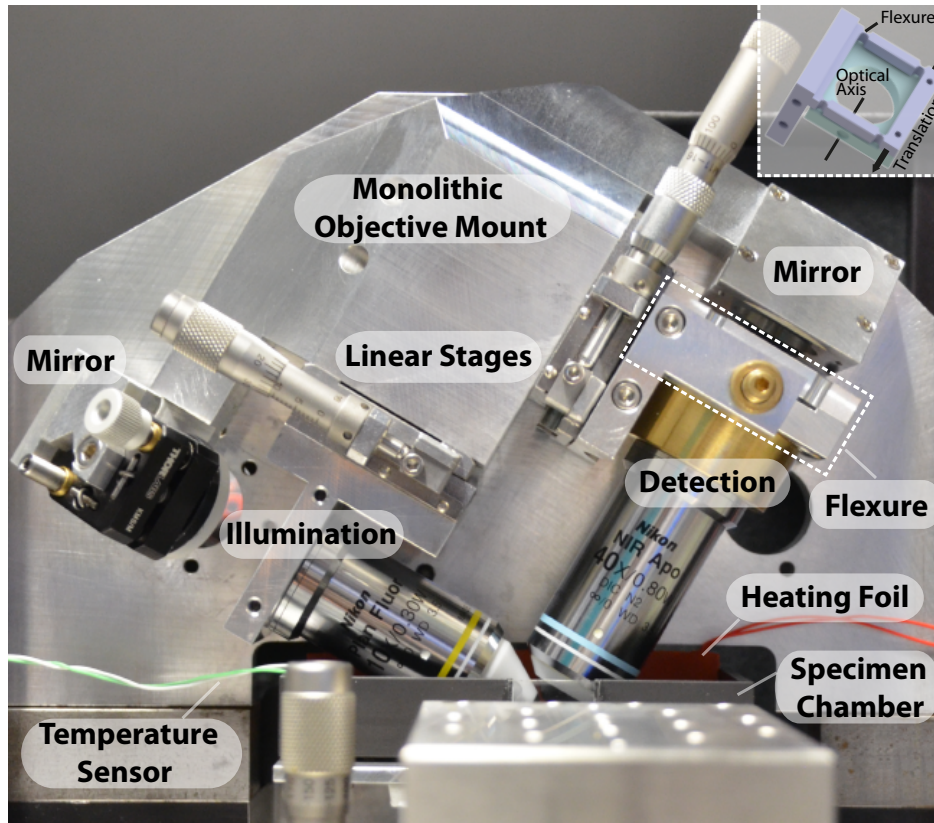


Figure 3.5: Monolithic objective mount unit for RESOLFT-SPIM. The illumination objective lens creates a light-sheet that hits the sample in the specimen chamber at an angle of 30° . Fluorescence is collected by a detection objective lens perpendicular to the illumination axis. Both lenses are mounted on the same aluminum block to reduce thermal drifts. They are translated along their optical axis with linear stages. For lateral positioning of the objective lenses a flexure is used (highlighted by a white dashed frame). The inset shows a CAD drawing and the translation axis of the flexure. The imaging medium can be heated with a silicon coated foil, that is placed in the specimen chamber. The temperature is controlled by a sensor in the medium.

along its optical axis. In addition, the light-sheets require an offset of about $500\ \mu\text{m}$ towards the front lens of the $25\times/1.1$ NA objective.

The illumination and detection objectives are held by a monolithic objective mount unit that is connected to the breadboard by a kinematic mount consisting of a system of balls, vee-grooves and magnets and can be lifted for conveniently replacing the sample or the objectives (cf. figure 3.5). The objective lenses can be moved along their optical axis by linear stages (M-SDS40 Precision, Newport Corporation, Irvine, CA). The relative lateral position of the objectives can be precisely adjusted with a home-build flexure design. A fine adjustment screw presses laterally on an aluminum piece holding the detection objective. As a consequence, this piece which is connected to a mono-

lithic flexure only translates in the desired lateral direction. The chosen design ensures a pure translation without rotation of the objective lens.

3.2.1.3 Detection unit

The detection objective is part of a wide-field microscope consisting of two identical emission band-pass filters (FF03-525/50-25, Semrock, Rochester, NY) and a tube lens ($f_{TL} = 300$ mm, Nikon, Tokyo, Japan) focusing the fluorescence onto one of two tested fast sCMOS cameras (Neo sCMOS, Andor, Belfast, UK and ORCA-Flash4.0 V2, Hamamatsu, Herrsching, Germany). The implemented camera chips contain 2560×2160 and 2048×2048 pixels, respectively, each with a pixel size of $6.5 \mu\text{m}$. The ORCA-Flash camera used for the biological applications presented in this thesis is a prototype of the commercial version. It was characterized in terms of gain, offset and dark counts of each pixel by the manufacturer. The resulting correction tables for each pixel are considered in the post-processing of the recorded image stack.

In the rolling shutter mode of the camera, the readout time of the camera chip is proportional to the number of readout lines. For an optimal RESOLFT-SPIM imaging speed, the implemented camera is rotated by β so that the readout lines of the sensor are aligned along the x -direction. A cropped FOV along the y -direction thus considerably shortens the required readout time and increases the overall frame rate. The setup is designed in a fashion that no kinematic mirror or lens mounts are needed in the detection path for aligning the fluorescence to the center of the camera FOV.

3.2.1.4 Specimen chamber

In this thesis, the concept of RESOLFT-SPIM is demonstrated on small biological specimens like single cells or cell colonies. The sample is usually attached to the surface of a standard round glass coverslip with a diameter² of 5 mm. For imaging it is clipped onto a platform on the bottom of a water-filled specimen chamber with a total volume of 40 ml. Figure 3.6a shows a CAD drawing of the cuboid-shaped chamber. The platform and the chamber itself is made of polyetheretherketone (PEEK). PEEK is a strong and stiff plastic material with a linear thermal expansion coefficient of $47 \cdot 10^{-6}/\text{K}$. It is often used in applications where stable performance at elevated temperatures is required. In addition, PEEK exhibits excellent resistance to a wide range of chemicals, i.e. ethanol and acetone as well as resistance to hot water-based liquids. Moreover, this highly biocompatible material is used for orthopedic and spinal implants [98]. In one side of the chamber, a glass window is inserted through which the light-sheets can be imaged from the side. This is particularly useful for alignment of the setup, as described in section 3.2.3.

² The maximal diameter of the coverslip is limited by the distance between the front lenses of the objectives in the sample region.

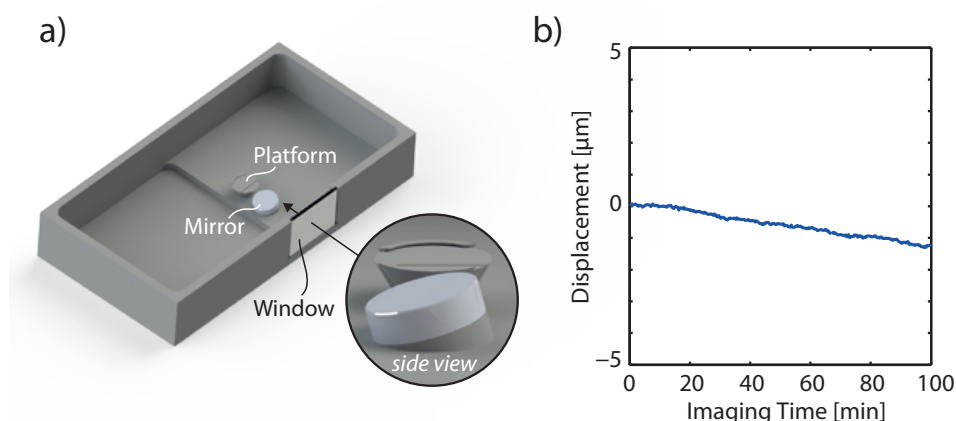


Figure 3.6: Specimen chamber for RESOLFT-SPIM. a) A standard round coverslip ($\varnothing = 5$ mm) with the sample is placed on a platform in the center of the cuboid-shaped specimen chamber made of PEEK. An imaging medium containing essential non-fluorescent additives for cell growth and HEPES buffer, and a temperature control adapt the conditions in the chamber to the physiological environment of living specimens. A glass window on one side is used for alignment described in section 3.2.3. b) The light-sheet reflection on a tiny mirror placed at 15° with respect to the horizontal plane is used to measure the stability of the chamber. A displacement of less than $0.7 \mu\text{m}$ in 60 minutes is extracted from the plot.

To accurately and reproducibly align the longer horizontal axis of the specimen chamber relative to scan direction, its lateral movement is kinematically constrained by a system of balls and vee-grooves. Tiny magnets on the bottom plate of the chamber keep it on top of an aluminum plate attached to the stage scanner but at the same time allow an easy removal of the chamber to exchange the specimen. To compensate tilts of the coverslip with respect to the horizontal plane, the entire chamber can be elevated by a fine adjustment screw in the aluminum plate on one side.

For measurements testing the stability of the microscope and further analysis and adjustment of the light-sheet parameters (cf. section 3.2.3), a second platform has been added to the chamber. It has a ramp of 15° with respect to the horizontal plane and thus 45° with respect to each of the objectives. A mirror was attached to the ramp with biocompatible silicon glue. The attenuated excitation light-sheet was reflected by the mirror and imaged by the detection objective and the tube lens onto the camera. One image per minute was recorded. The peak position of the light-sheet x-z cross-section was fitted by a Gaussian function. Its distance to the position measured in the first image was plotted versus time in figure 3.6b. A displacement of less than $0.7 \mu\text{m}$ in 60 minutes is in the reported range of many commercially available microscopes without drift correction.

The specimen chamber is ideally adapted to the physiological conditions of the cell samples. For this reason, the biochemical environment of the speci-

men in the chamber is controlled by appropriate imaging media, e.g. a cell culture medium optimized for cell growth. However, these media often contain additives such as pH indicators or serum components that are fluorescent in the RESOLFT-SPIM setup and potentially obscure the desired fluorescence signal. To find the optimal medium for the new technique, the background fluorescence generated by various liquids has been measured and compared (cf. figure A.3). For the biological applications shown in this thesis, FluoroBrite DMEM (Invitrogen, Carlsbad, CA) mixed with HEPES offers an acceptable compromise between background fluorescence and viability of the specimen. In addition, the imaging medium is heated to temperatures up to 35°C by placing a heating foil (HR5269, Minco, Minneapolis, MN) covered with silicon rubber in the specimen chamber. The temperature is manually monitored by an external sensor shown in figure 3.5. Mineral oil (M5310, Sigma-Aldrich, St. Louis, MO) prevents vaporization of the imaging medium during long term measurements.

3.2.1.5 Stage scanner

A piezoelectric stage (P-625.1CL, PIHera Piezo Linear Stage, Physik Instrumente, Karlsruhe, Germany) with a minimal step size of 10 nm and a total range of 500 μm scans the sample in steps through the static light-sheets. A step response time of 102 ms/ μm was preset by the manufacturer. It assures a stable scan throughout the measurement. The scanner is attached to a multi-axis positioning stage (562 ULTRAlign Precision, Newport Corporation, Irvine, CA) with which the sample is centered to the detection focal plane.

3.2.2 Hardware control

All electronic devices in the setup, i.e. lasers, camera and the stage scanner are controlled by software composed in LabVIEW. The lasers have a digital enabling and disabling channel and an analogue channel for the control of their output power. The stage only requires a constant analogue signal, whereas the camera only needs a digital external trigger signal. For imaging, a sequence of signals is fed into an FPGA, which then simultaneously sends the signals to the devices. This procedure, illustrated in figure 3.7, allows for synchronization of the scanning process and the image acquisition. The continuous repetition of a sequence of signals generates a real-time image at a static scan position which is used to select the region of interest in the sample prior to imaging. The RESOLFT-SPIM images acquired by the sCMOS camera and the images recorded by the CCD cameras for alignment (cf. section 3.2.3) are stored on the camera PC.

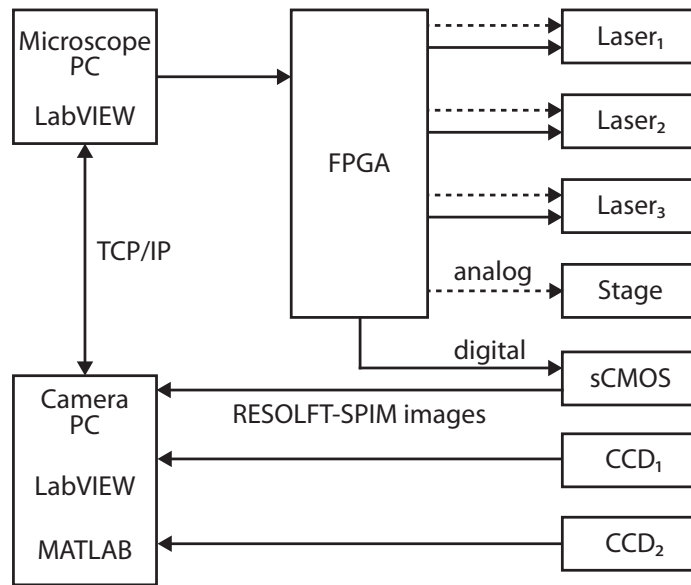


Figure 3.7: Block diagram of the hardware in the RESOLFT-SPIM setup. Controlled by a LabVIEW software on the microscope PC, an FPGA synchronously sends sequences of analogue and digital signals to the implemented devices. The camera PC saves RESOLFT-SPIM images acquired by the sCMOS camera as well as images taken by the CCD cameras for alignment.

3.2.3 Alignment strategies

A number of crucial parameters need to be adjusted for the best possible imaging performance of the RESOLFT-SPIM setup. In addition to the alignment steps of a conventional SPIM microscope with a single light-sheet, here especially the relative alignment of the three applied light-sheets needs to be considered. In a perfectly aligned RESOLFT-SPIM setup, all three laser beams are collinear in the illumination beam path and hit the illumination objective lens in the center of the back-focal plane at a right angle. In addition, the laser beams are ideally collimated for a common focal spot in the sample. The position of minimal beam waist is then aligned to the center of the FOV of detection. Moreover, all light-sheets coincide with the focal plane of detection.

In the following, the routine alignment procedure is described. Two indispensable tools that have been employed for a precise alignment of the RESOLFT-SPIM microscope are highlighted.

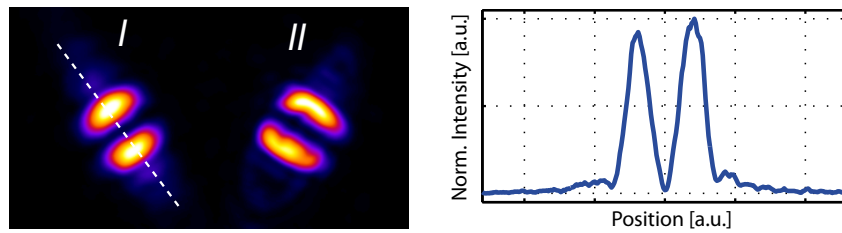


Figure 3.8: Tool for collinearity alignment of RESOLFT-SPIM lasers. A half transparent pellicle at one position and a removable mirror at a further position along the combined illumination beam path direct the three laser beams towards the same CCD camera. In the aligned RESOLFT-SPIM setup, the beam cross-sections are imaged to two triples (*I* and *II*) with the same size. Also, the symmetry of the off-switching illumination pattern can be evaluated in a line profile.

Collinearity alignment

In a standard SPIM setup, multiple laser lines are often combined in an optical fiber which is then fed into the microscope. A co-alignment of the applied lasers is thus achieved by setup design. A misplacement of the laser beam prior to laser coupling leads to a reduced intensity in the setup rather than an offset. A similar alignment procedure is not applicable to the RESOLFT-SPIM setup since the TEM_{10} mode of the off-switching laser cannot be coupled into a single mode fiber. For this reason an alignment tool has been employed which allows for precise control of collinearity and collimation of the lasers. To this end, the cross-sections of all three laser beams at two positions in the beam path are simultaneously imaged on the same detector. These images are made accessible by inserting an approximately half transparent pellicle at an early position and a removable mirror³ at a further position along the illumination path. These optical elements and the corresponding beam paths are included in figure 3.2.1. Additional mirrors route the auxiliary beams on a lens ($f_{L10} = 40$ mm) that images the cross-sections on a CCD camera (DMK 41AU02, The Imaging Source, Bremen, Germany). The diameters of the already expanded beams at the position of the removable mirror are reduced with a home-built reverse beam expander. In the ideal case of perfect alignment, the collimated lasers form two concentric triples of equal size on the camera.

As shown in figure 3.8, with a line profile through the imaged cross-section of the off-switching beam, the illumination pattern can be checked for symmetry. The quality of the intensity zero, however, cannot be evaluated. The low NA of the imaging lens in front of the CCD camera does not capture

³ The removable mirror is also inserted in the aligned RESOLFT-SPIM microscope to easily measure the power of the beams or supervising the timing of the laser pulses prior to imaging.

the polarization components along the illumination axis, in contrast to the objective lens with higher NA.

Alignment to the illumination objective

In the next step, the collinear and collimated beams are aligned with respect to the illumination objective. In the RESOLFT-SPIM setup this is done with the help of two pinholes which are separately placed along the illumination axis. The aluminum tube which holds and connects the pinholes is screwed in the position of the illumination objective. A perfectly aligned beam passes both pinholes at its center.

Alignment to the focal plane of detection

In order to precisely align the generated light-sheets to the focal plane of the detection objective, a second auxiliary beam path has been implemented. Two lenses placed perpendicular to both objectives image the y - z cross-section of the light-sheets onto a CCD camera (HXG40, Baumer, Frauenfeld, Switzerland). Figure 3.9 shows a projection of the CAD drawing and the beam path as green line. A fluorescence signal generated in the specimen chamber is detected by a lens ($f_{11} = 30$ mm) through the glass window. Small mirrors route the collected light onto the center of a second lens ($f_{12} = 50$ mm) which images the emitter onto the camera. The whole construction is placed on top of the micro positioning stage which translates the lens system with respect to the common focal spot of both objectives.

The beams are made visible in the zebrafish medium E3 that is filled in the specimen chamber. It contains methylene blue, one of the early fluorophores described in section 2.1.2. Here, fluorescence emitted by methylene blue molecules reveals the light-sheet cross-sections. The images are shown in figure 3.9b. The characteristic profile for each light-sheet is clearly visible. Especially, the intensity distribution of the off-switching illumination pattern can be seen and adjusted if needed. In the case of perfect alignment, the off-switching illumination pattern is equally intense on both sides of the zero-intensity area at any position along the light-sheet to efficiently switch off the RSFPs above and below the focal plane to equal parts. Importantly, the angle of the light-sheets with respect to the detection focal plane can be analyzed. Assuming a precise manufacture of the front plate holding the objective lenses, the light-sheets are parallel to the detection front lens if they enclose an angle of $\beta = 30^\circ$ with the horizontal plane. In addition to the alignment of the laser beams, the rotation of the cylindrical lens can be optimized. It is properly oriented, if the imaged cross-sections feature a minimal beam waist $\omega_{0,z}$.

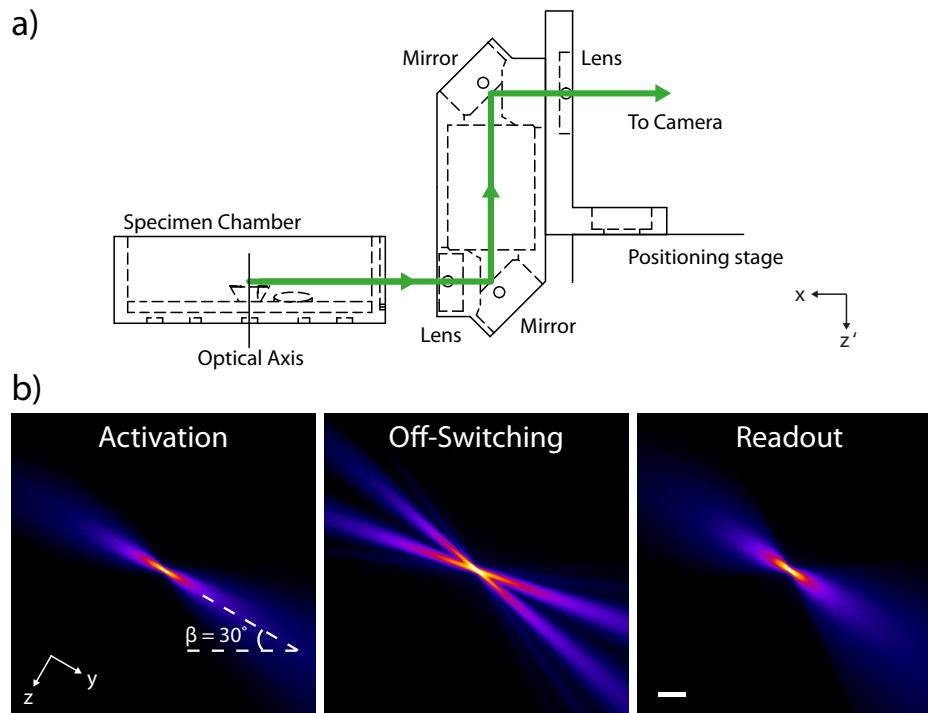


Figure 3.9: Tool for the alignment of the light-sheets to the focal plane of detection. a) Fluorescence emitted in the RESOLFT-SPIM specimen chamber is collected perpendicular to both the illumination and the detection axis and is imaged onto a CCD camera. b) The y - z cross-sections of the activation, off-switching, and readout light-sheets are made visible in E3 medium containing methylene blue. The light-sheets are parallel to the focal plane of detection at an angle of 30° to the horizontal axis. Scale bar: $100\ \mu\text{m}$.

Alignment to the FOV of the camera

The minimal beam waist along the illumination axis of the collinear light-sheets is then placed in the center of the detection FOV for ideally homogeneous illumination of the sample. For this purpose, the specimen chamber is again filled with E3 medium containing methylene blue. Here, the emitted fluorescence is collected by the detection objective and imaged on the sCMOS camera. Figure 3.10 illustrates the setup for this experiment and the resulting image for a readout light-sheet generated by a $40\times/0.8$ NA illumination objective. The x - y cross-section of the light-sheet is made visible. In a perfectly aligned RESOLFT-SPIM setup, the focus of the illumination objective is imaged on the center line of the camera chip. For alignment, the imaging medium is illuminated at maximal laser power. As a result, some fluorophores around the focus of illumination are bleached which is detected as region of lower fluorescence in the image. This darker line can then be easily aligned to the center of the detection FOV by translating the illumination ob-

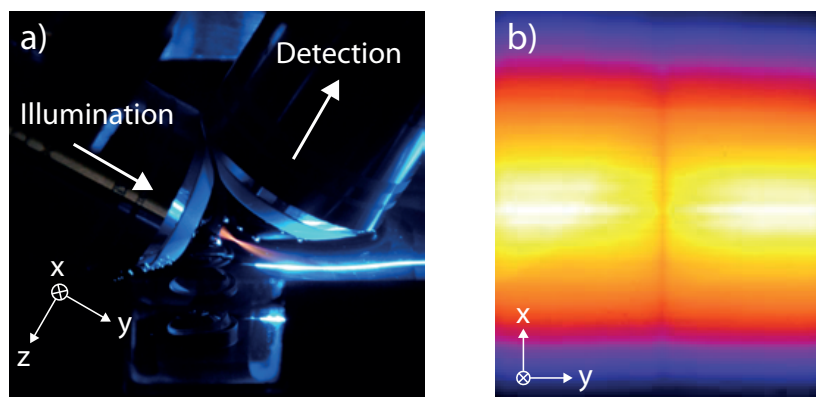


Figure 3.10: Light-sheet alignment to the FOV of detection. a) The x - y illumination profile of an activation light-sheet generated by a 40x/0.8 NA objective is made visible in fluorescent medium and recorded with the sCMOS camera. b) At high laser power, an area around the position of minimal light-sheet thickness is partially bleached. This line of reduced fluorescence is placed to the center of the detection FOV by axially translating the illumination objective lens. If this line is imaged sharply on the camera, the light-sheets coincide with the focal plane of detection. Also the axial position of the cylindrical lens and the relative lateral position of the objective lenses can be analyzed in this alignment setup.

jective along its axis. Furthermore, the x - y plane of the light-sheets coincides with the focal plane of detection if this darker region is sharply imaged on the camera. This alignment procedure is only valid for the activation and read-out light-sheet, since the illumination profile of the off-switching laser only affects out-of-focus fluorophores. However, for collinear light-sheets also the plane of zero-intensity coincides with the detection focal plane.

In addition, the position of the cylindrical lens can be evaluated in the same image. Ideally, the light-sheet features a minimal beam waist $\omega_{x,0}$ at the center of the detection FOV. It is worth a remark, that the relative x -position of the objectives can also be analyzed. A displacement results in an offset of the illumination pattern in the x -direction of the image. It is corrected by translating the detection objective with the flexure design shown in figure 3.5.

3.3 RESOLFT-SPIM imaging

The imaging capabilities of RESOLFT-SPIM are especially highlighted when the acquired super-resolved images are compared to conventional diffraction-limited SPIM recordings of the same sample region. This section explains how these images are taken and represented. The imaging strategy and the processing routine, described in the following, are applied to all biological applications presented in this thesis.

3.3.1 Imaging strategy

A general description of the imaging procedure using RESOLFT-SPIM is presented here. The trigger sequences of the involved devices are sketched in figure 3.11. Rising and falling edges mark enabling and disabling events of a digitally controlled device, respectively. Also, the analogue signal of the stage scanner is shown. The vertical dashed lines frame the time period of one scanning step. The depicted sequence in this period is repeated for each targeted position in the sample until the scan is stopped. Typically several tens of micrometers are scanned with a step size of 50 nm and an acquisition time of 80-200 ms per step.

First, the stage scanner moves to the start position of a region of interest. Then, the RSFPs are activated by a UV light pulse of length t_{act} . A short illumination pause of 2 ms allows the fluorophores to relax to an equilibrium state. For RESOLFT-SPIM images, it is followed by an off-switching pulse of length t_{off} which is typically longer than t_{act} . For negative switching RSFPs the off-switching is a competing process to the generation of fluorescence. Consequently, a high number of photons are emitted for the time period of t_{off} and directed towards the detector. Although the camera is not active during activation and off-switching, some photons are converted into signaling electrons on the sensor. Because of this so called *afterglow effect*, the camera is set active for a FOV-dependent exposure time and an image is recorded. This image, which is labeled as *I* in the figure, is discarded from the image stack after the measurement. More details about the afterglow effect and its dependency on the off-switching power can be found in appendix A.1. Subsequently, another image, labeled as *II*, is recorded with the same exposure time. It serves as dark image and is subtracted from the signal in the processing routine (cf. section 3.3.2). The third image (*III*) is the actual sub-diffraction RESOLFT-SPIM image. It is taken during the readout period t_{on} with the 488 nm laser. In order to directly visualize the resolution improvement by RESOLFT-SPIM, a conventional SPIM image is taken in a second activation and readout cycle with the same exposure time and light intensity. Since the off-switching laser is not used here, a diffraction-limited image *IV* is generated. According to the results obtained from the stability measurement shown in figure 3.6, the sample region recorded in images *III* and *IV* can be considered identical. Also, the exposure times are short compared to typical movements of the specimens imaged in this section. Finally, the stage scanner moves to the next position where another illumination cycle starts.

By translating the scanner only in the horizontal plane, the biological sample is always positioned at the minimal light-sheet waist. This assures that the sample is imaged with the same axial resolution at any scan position. In principle, a very large area, up to the maximal scanning range of the scanner can be imaged with this method.

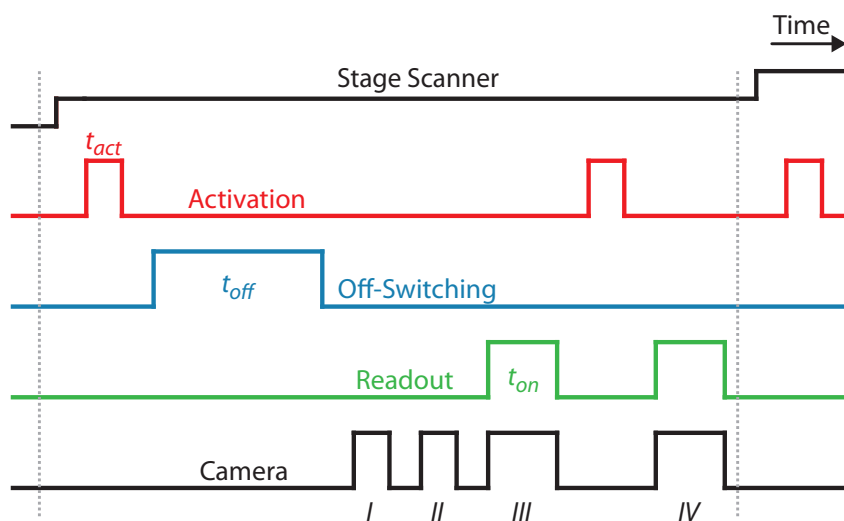


Figure 3.11: Signal sequence for RESOLFT-SPIM images. The stage scanner moves to the start position. Then, the activation laser switches the fluorophores to the on-state for a light pulse length of t_{act} . The off-switching laser subsequently switches a subset of the activated fluorophores back to the off-state. The sample is illuminated for a time t_{off} . During these periods, no images are recorded. Since the fluorescence is a competing process to the off-switching, the camera is illuminated without being readout which produces unwanted signals (afterglow effect). To clear the camera chip, an image (*I*) with a minimal exposure time is taken followed by an image (*II*) that is later subtracted as background. The residual activated RSFPs are read out for a time t_{on} , which is also the exposure time of the camera. Image *III* is the RESOLFT-SPIM image. Another activation pulse followed by a second readout period generates a diffraction-limited conventional SPIM image (*IV*). The sequence between the vertical dashed lines is repeated for each scanning position.

3.3.2 Image representation

Image data recorded in RESOLFT nanoscopes and standard SPIM do typically not require any post-processing such as fitting, denoising or restoration. The excellent signal-to-noise ratio characteristic for both techniques even corroborates this fact. Also their combination, the new RESOLFT-SPIM technique, benefits from these advantages. As described in section 3.3.1, an image stack consisting of a sequence of thin two-dimensional optical slices of the sample is recorded. It contains data acquired in RESOLFT-SPIM and diffraction-limited conventional SPIM mode. After sorting of the images according to their imaging method, the information in the 3D stacks is displayed as a single frame image or an appropriate 2D projection for this thesis.

The power of the new microscope is ideally demonstrated in image cross-sections perpendicular to the optical axis of the light-sheets. Single slices in the x - z and y - z plane are of particular interest for measuring the axial resolution of the RESOLFT-SPIM technique. In a projection of maximum inten-

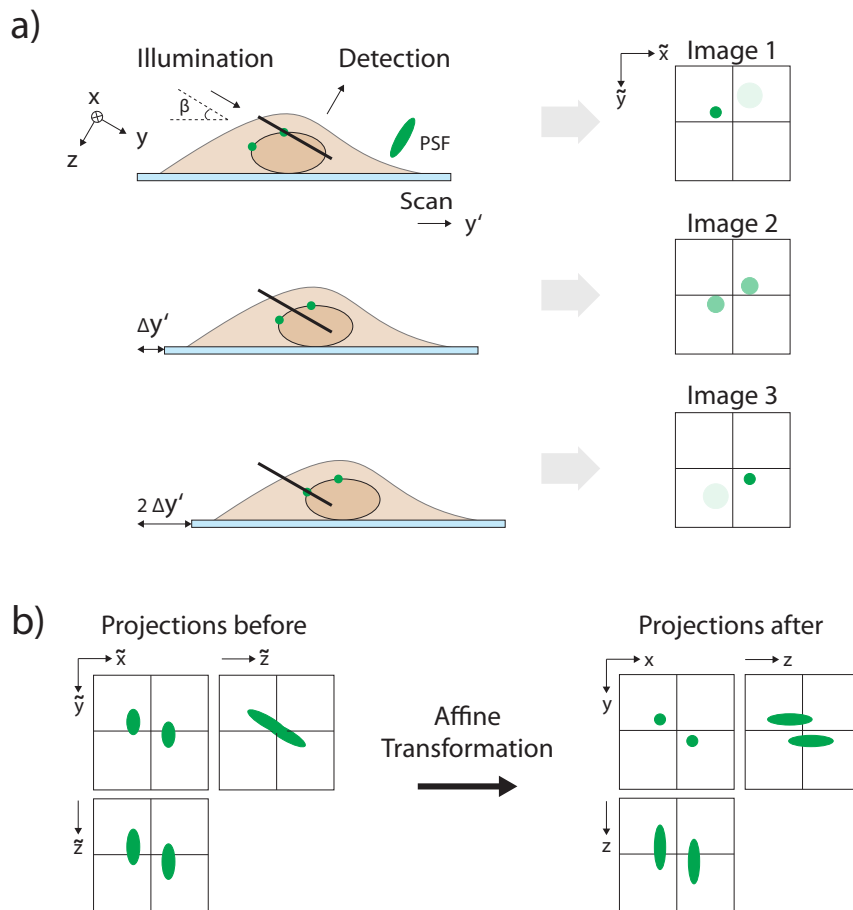


Figure 3.12: Representation of RESOLFT-SPIM images. a) A sample with two fluorophores is scanned in y' direction through the static illumination light-sheet, which encloses an angle β with the horizontal plane. For clarity, the effective PSF after off-switching is here elongated along the z -axis. Three steps of the scanning process are illustrated. The resulting images taken in the FOV of the camera (black line) are shown on the right. b) The acquired image stack is affinely transformed to the coordinate system of the objective lenses, so that the axial and lateral extent of the effective PSF is directly visible in the according maximum projections. Note that the affine transformation does not change the raw character of the RESOLFT-SPIM images.

sity of multiple of these slices along y and x , respectively, the separation of objects with a distance below the diffraction limit can be demonstrated. In order to extract the desired views of the data stack, the recorded images are transformed to the coordinate system of the light-sheet. It should be noted, that the procedure described in the following re-arranges the acquired data without changing its raw character. The derived algorithm was implemented in a MATLAB script.

The crucial steps to obtain the x - z and y - z projections from the recorded data are explained in figure 3.12. For the description of the concept, a model cell is grown on a coverslip in the RESOLFT-SPIM setup, as an example for any specimen. Two sparse proteins on the nuclear membrane are tagged with an RSFP. The cell is placed in the focal plane of the detection objective indicated by the black line through the nucleus. In order to distinguish the lateral and axial direction in the sketch, the effective PSF is elongated in the z direction and has a cylindrical symmetry. The sample is moved in y' -direction at an angle of $\beta = 30^\circ$ with respect to the light-sheets. The step size is denoted as $\Delta y'$. At each scan position a two-dimensional image in the x - y plane is captured by the camera (cf. figure 3.12a). In the first image, one of the fluorophores is in focus. The other fluorophore is in focus after two scanning steps. The maximum projections of the recorded raw image stack before processing are illustrated in figure 3.12b. The projections in the x - z and y - z planes are obtained by reslicing the image stack in the corresponding direction. The image of a single emitter appears tilted. To transform the data to the x - y - z coordinate system of the objective lenses, the data stack is affinely transformed in a shear operation using the following matrix.

$$\begin{pmatrix} x \\ y \\ z \end{pmatrix} = \begin{pmatrix} 1 & 0 & 0 \\ 0 & 1 & a \\ 0 & 0 & 1 \end{pmatrix} \begin{pmatrix} \tilde{x} \\ \tilde{y} \\ \tilde{z} \end{pmatrix} \quad \text{with} \quad a = \frac{\Delta y'}{p_{x,y}} \sin 60^\circ, \quad (3.1)$$

where $p_{x,y}$ is the sampling size in the x and y direction of the image. It depends on the overall magnification M of the detection system and the physical pixel size of the camera $p_{x,y}^{cam}$. Typically, M can be expressed in terms of the magnification of the detection objective lens M_{obj} and the focal length of the implemented tube lens f_{tub} in millimeters, which leads to

$$p_{x,y} = \frac{p_{x,y}^{cam}}{M} = \frac{200 p_{x,y}^{cam}}{M_{obj} f_{tub}}. \quad (3.2)$$

In the RESOLFT-SPIM setup the lateral sampling size has a value of $p_{x,y} = 108.3$ nm for $p_{x,y}^{cam} = 6.5$ μm , $f_{tub} = 300$ mm and $M_{obj} = 40$. The sampling size in z depends on the step size of the scan and can be calculated as

$$p_z = \Delta y' \sin \beta. \quad (3.3)$$

For an angle of $\beta = 30^\circ$, p_z is exactly half the step size of the scan. Since an anisotropic voxel size is ideally suited to visualize the resolution improvement in RESOLFT-SPIM, all images in this thesis will be displayed in this scaling unless otherwise noted⁴. The projections of the resulting x - y - z stack are shown in figure 3.12b. The axial and lateral resolution of the setup can be directly measured in the processed x - z and y - z projections. The x - y projection serves as an overview image of the specimen. It is mirrored so that sample features in the overview image can be directly recognized in the x - z projection.

3.4 Characterization of the setup

In this section the RESOLFT-SPIM setup is characterized. First, the parameters of the applied light-sheets are measured and analyzed. Then, the PSF of the system and the quality of the intensity zero region is determined using gold colloids. Furthermore, the resolving power of RESOLFT-SPIM is demonstrated on single RSFP filled objects. These also serve as samples for the validation of the known square root law using the new technique. In addition, the Rayleigh length of the effective light-sheet generated by the off-switching process is measured. Finally, the enhancement in axial resolution enabled by the new optical nanoscope is demonstrated in RESOLFT-SPIM images of dense samples.

3.4.1 Light-sheet parameters

Once the light-sheets have been aligned using the strategies described in section 3.2.3, their extent measured at FWHM in the axial and lateral direction, i.e. Δz and Δx , in the sample can be characterized. These parameters define the Rayleigh range in both dimensions and are important since they set the boundaries of the usable FOV of the setup according to equation 2.17. The reduction of Δz in the RESOLFT-SPIM imaging mode is later in this thesis shown to influence the FOV (cf. section 3.4.5). The Δz values obtained in this experiment serve as reference.

The parameters are measured by reflecting the light-sheets on a mirror that was glued in the specimen chamber (cf. figure 3.6a). Since the mirror surface is positioned at an angle of 15° with respect to the horizontal plane, the camera image directly displays the x - z cross-sections of the light-sheets. The laser beams have been attenuated before they hit the illumination objective and the emission band-pass filters have been removed for this experiment. The position of minimal beam waist is set to the center of the FOV _{y} . Scanning the mirror through the static light-sheets, translates and defocuses the cross-sections on the chip. A similar processing routine as described in section 3.3.2,

⁴ For an isotropic voxel size, the processed x - z and y - z cross-sections need to be scaled by $p_z/p_{x,y}$.

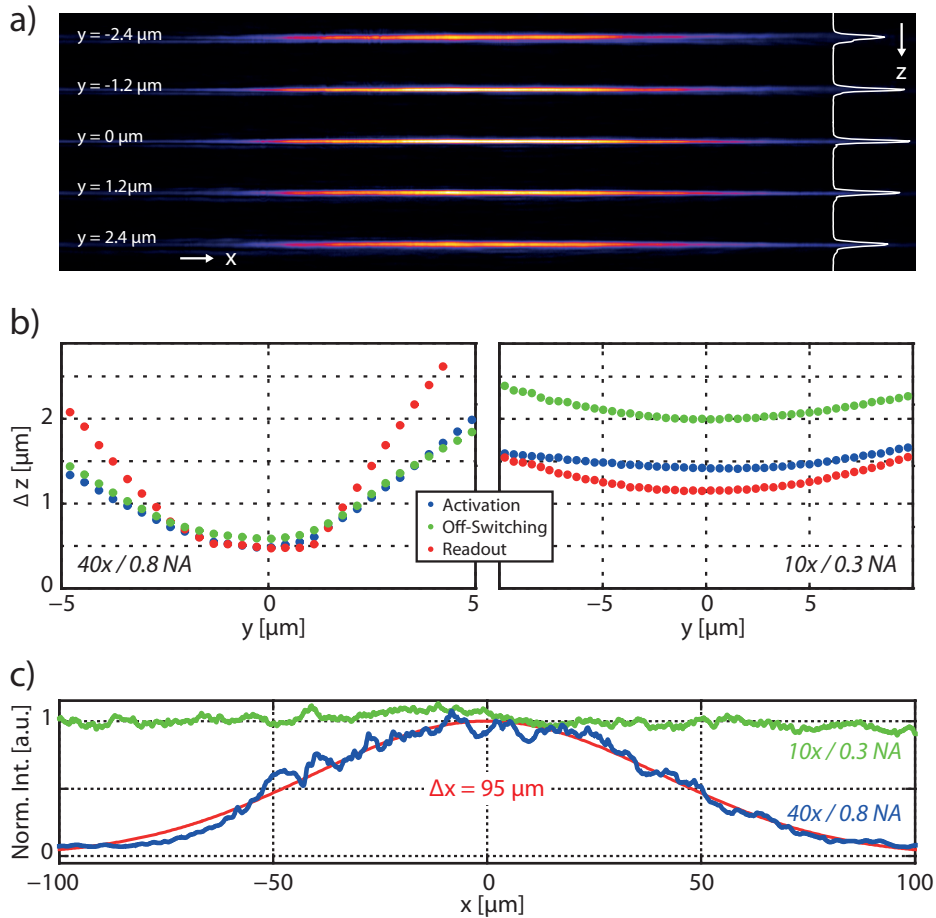


Figure 3.13: Measurement of light-sheet parameters. a) A mirror in the RESOLFT-SPIM specimen chamber with a surface angle of 15° to the horizontal plane is scanned through the static readout light-sheet generated by a $40\times/0.8$ NA objective lens. At each scan position, an x - z cross-section is recorded. Here, five images of positions around the light-sheet focus at $y = 0$ are shown in a montage. A line profile along the z -axis across the integrated light-sheet intensity reveals an increase in light-sheet thickness even at short distances to the focus. b) In this style, all light-sheets that are applied in this thesis have been characterized. The FWHMs of Gaussian fits to the line profiles along z are plotted versus the illumination axis y . The data points of the activation, off-switching, and readout light-sheets are displayed as blue, green, and red dots, respectively. The light-sheets generated by a $10\times/0.3$ objective lens (right) exhibit measured Rayleigh lengths that are 6.5 times longer than those measured for light-sheets generated by a $40\times/0.8$ NA objective lens (left). c) The lateral extent of an off-switching light-sheet in the x -direction is plotted for a $40\times/0.8$ NA (blue) and a $10\times/0.3$ NA (green) illumination objective lens. A Gaussian fit to the high NA intensity profile reveals a FWHM of $95\ \mu\text{m}$, whereas the low NA light-sheet uniformly covers the entire FOV of the camera.

which here also accounts for the additional tilt of the mirror surface, results in a stack of x - z images along the optical illumination axis y . Figure 3.13a shows a typical scan of the readout laser using illumination and detection objectives with an NA of 0.8. In a montage, the x - z cross-sections at five positions along the y -axis are displayed together with the vertical intensity profile of the image summed along the x -axis. A significant reduction in intensity and broadening of the light-sheet profile is visible already at relatively small distances of $y = \pm 1.2 \mu\text{m}$ to the position of minimal beam waist at $y = 0$ and is even more evident at $y = \pm 2.4 \mu\text{m}$.

In this style, the cross-sections of all light-sheets that are used in this thesis have been imaged and analyzed. From fits to the axial intensity profiles at several y -positions along the illumination axis, the light-sheet thickness Δz is extracted. A Gaussian function was fitted to the activation and readout profiles, whereas a typical off-switching profile as shown in figure 2.10c was fitted to the off-switching laser⁵. Figure 3.13b displays the results for each light-sheet generated by a 40x/0.8 NA and a 10x/0.3 NA illumination objective. As expected, the light-sheet thickness increases from the center to either side in a hyperbolic shape for all lasers. The activation, off-switching and readout light-sheets have a FWHM at the minimal beam waist Δz of 460 nm, 576 nm, and 458 nm for the high NA objective lens and 1407 nm, 1294 nm, and 1914 nm for the low NA objective lens, respectively. The Rayleigh ranges $y_{0,z}$ are measured to range between 1.8 and 2.3 μm in the high NA and between 12.1 and 19.4 in the low NA case. In contrast to the readout and off-switching lasers, the activation laser does not use the full NA of the low NA objective. For this reason, the light-sheet has a thicker beam waist and a longer Rayleigh range. If this is taken into account, the measured values are in good agreement with the theoretical values obtained from equations 2.16 and 2.17.

Additionally, the lateral extent of the light-sheets at the position of minimal beam waist is measured. To this end, the x - z cross-section at $y = 0$ is summed along the axial direction. Figure 3.13 shows the normalized profile of the off-switching laser for the 40x/0.8 NA illumination objective. A Gaussian fit curve to the data points reveals a value of $\Delta x = 95 \mu\text{m}$. For comparison, the normalized data points obtained from the measurement with a 10x/0.3 NA objective are also plotted. At a total magnification of $M = 60$ in the detection path, the light-sheet uniformly illuminates the sample region across the full FOV_x of the camera. Similar values have been obtained for the activation and readout light-sheets. It is worth a remark that the lateral extent of an illuminating light-sheet can be controlled by the focal length of the implemented cylindrical lens.

⁵ In this case, Δz is the distance from the zero-intensity center to the $1/e^2$ drop in intensity on the outer slope of the profile divided by 0.85.

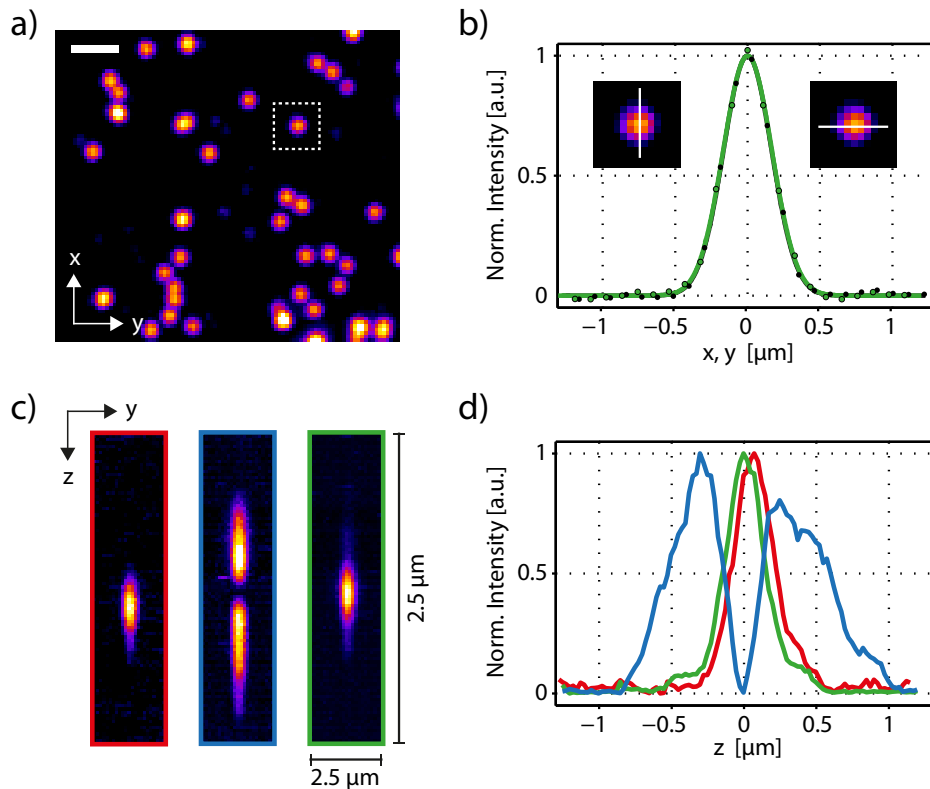


Figure 3.14: Measurement of the system's PSF and analysis of the zero-intensity region. Gold colloids on a glass coverslip scatter light of the laser light-sheets generated by a 40x/0.8 NA illumination objective, which is then imaged onto an sCMOS camera. a) An overview image in the x - y plane shows the gold colloids imaged with the readout light-sheet. Scale bar: 1.5 μm . b) Line profiles in x - and y -direction through an arbitrary gold colloid image are shown. Gaussian fits to the data points reveal a FWHM in x (green dots and curve) and y (black) of 390 and 394 nm, respectively. c) A y - z projection ($2.5 \times 2.5 \mu\text{m}^2$) of a gold colloid imaged with the activation (red), off-switching (blue), and readout (green) light-sheet is shown. Note that the sampling size in z is 25 nm, whereas the sampling size in y is 108.3 nm and the image has squared dimensions. The off-switching illumination profile clearly features an intensity minimum in the center. d) Line profiles along z displays that the minimum is close to the background signal which allows for RESOLFT-SPIM images with a potentially high signal-to-noise ratio. Despite a slight displacement from the center, the activation and readout peaks fully cover the off-switching zero-intensity position. Fits to their profiles exhibit a FWHM of 326 and 318 nm, respectively.

3.4.2 Quality of the zero-intensity region

In a further experiment, the quality of the zero-intensity region created by the off-switching laser and the axial extent of the activation and readout PSF in the RESOLFT-SPIM setup have been measured. These are crucial parameters

since residual intensity at the center of the off-switching pattern reduces the signal-to-noise ratio in the RESOLFT-SPIM images.

The implemented light-sheets generated by a 40x/0.8 NA objective lens illuminated a sample of gold colloids with a diameter below the diffraction limit. The sample preparation is described in appendix A.2. The scattered light was collected by the 40x/0.8 NA detection objective, routed through the band-pass filters and imaged on the ORCA Flash camera. A range of 20 μm on the coverslip was scanned with a step size of 50 nm. At each scan position, an image was recorded with each of the activation, off-switching, and readout laser, respectively. Figure 3.14 summarizes the results. From an overview image ($10.4 \times 9.4 \mu\text{m}^2$) in the x - y plane of the readout laser displayed in figure 3.14a, one image of an arbitrary gold colloid was extracted. The lateral line profiles along x and y reveal a FWHM of 390 and 394 nm, respectively. The line profiles for the activation and off-switching laser have similar lateral extents (data not shown). Figure 3.14b shows a y - z projection of an imaged gold colloid for each of the three light-sheets. The $2.5 \times 2.5 \mu\text{m}^2$ images appear elongated along z because of sampling sizes of 108.3 in the y - and 25 nm in the z -direction. From the corresponding line profiles along z it can be deduced that the activation and readout peaks overlap with the zero-intensity center. Furthermore, the depth of the off-switching profile reaches a level close to the background signal, which defines the intensity zero in the plot. The PSFs of the activation and readout light-sheets have an axial FWHM of 326 and 318 nm, respectively. It should be noted that these values are even lower than the measured FWHM values in the lateral direction.

3.4.3 Resolving power

As described in section 2.2.2, the FWHM of a Gaussian fit to the imaged fluorescence intensity distribution of a single emitter is often considered as a measure for the resolving power of a microscope. To circumvent the potential problems of single molecule imaging, it is common to employ spherical objects marked with multiple fluorophores as technical samples to determine the resolving power⁶. If the actual size of the object was independently measured with another technique, the effective PSF can be calculated from the recorded image.

In order to determine the resolving power of RESOLFT-SPIM, single particles of the human immunodeficiency virus (HIV) type I have been imaged. HIV-1 was the first HIV version discovered and is the most widespread type worldwide. A single virion is approximately spherical with a mean diameter of 160 nm, which was derived in other studies [151]. A virion with this mean diameter contains more than 2000 Gag proteins [18]; about half of these were

⁶ In many fluorescence microscopy experiments silica beads filled with synthetic dyes are used as technical samples. A method that describes how to fill these beads with RSFPs has not been reported yet.

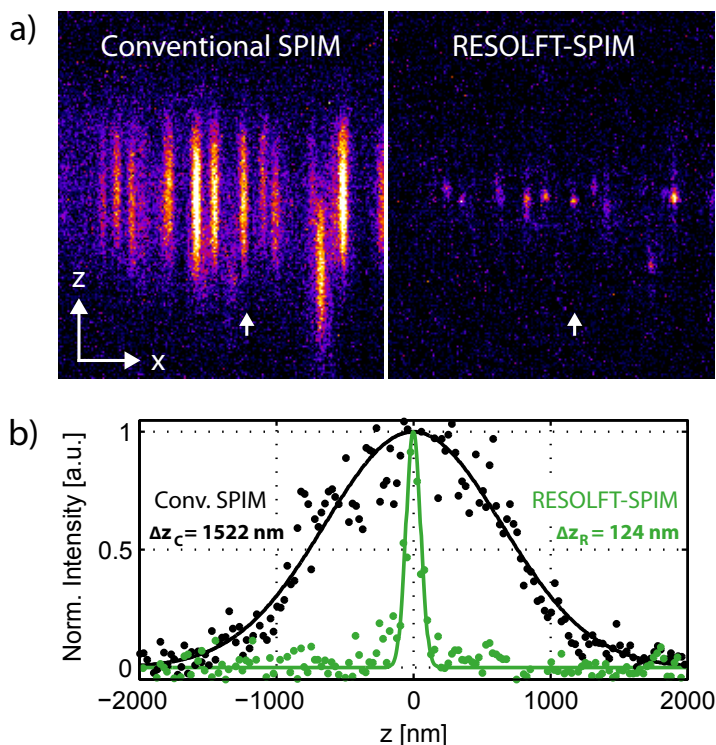


Figure 3.15: The resolving power of the RESOLFT-SPIM nanoscope is measured on single HIV-1 particles. a) Virions enclosing up to 1000 rsEGFP2 molecules are imaged on a glass coverslip in conventional SPIM and RESOLFT-SPIM mode. An x - z cross-section through a typical three-dimensional image stack clearly shows the improvement in z -resolution enabled by the RESOLFT-SPIM technique. Note that the pixel size in both images is 108.3 nm in x - and 25 nm in z -direction, which results in image dimensions of $19 \times 5 \mu\text{m}^2$. b) The pixel intensity along a line in the z -direction through the same single virus particle is plotted for conventional SPIM (black dots) and RESOLFT-SPIM (green dots), respectively. The x -position of the line profiles is marked with white arrows in the images. The FWHMs of Gaussian fits to the data reveal an improvement in axial resolution by RESOLFT-SPIM by a factor of 12.3 compared to standard SPIM.

tagged with rsEGFP2 for the following experiment. A sketch of a typical matured HIV-1 particle and a description of the labeling procedure can be found in appendix A.3.

rsEGFP2 filled HIV-1 particles were sparsely distributed on a glass coverslip as described in appendix A.2. Following the imaging procedure explained in section 3.3.1, 3D stacks containing RESOLFT-SPIM and conventional SPIM images of the same region in the sample have been acquired. The RESOLFT-SPIM images were obtained with the following parameters. First, the sample was illuminated with the activation light-sheet for 10 ms. The power measured close to the back-focal plane of the illumination objective was 250 μW . After a short pause of 2 ms, the off-switching laser with a power

of 7.11 mW irradiates the sample for 30 ms. After two additional frames for sensor clearing and background reference with an exposure time of 10 ms, the residual activated fluorophores were read out with a power of 155 μ W that was applied to the sample for 50 ms. Conventional SPIM images were obtained with the same activation and readout light intensities and exposure times. A total range of 20 μ m was scanned with a step size of 50 nm.

The acquired RESOLFT-SPIM images are compared to the conventional SPIM images in terms of axial and lateral resolution. The results are summarized in figure 3.15. Raw x - z cross-sections of the recorded image stacks are shown. A standard SPIM image of a single virus is extended in the z -direction as a consequence of the convolution of the virus object and the typical anisotropic PSF (cf. section 2.2.1). In RESOLFT-SPIM mode, the effective light-sheet is axially confined by the off-switching light pattern which results in a less elongated effective PSF. It needs to be pointed out, that the pixel size in both images is 108.3 nm in the lateral and 25 nm in the axial direction. A FWHM of $\Delta z_R = 124$ nm is measured on a single virion. For comparison the same particle imaged with conventional SPIM has a FWHM value of $\Delta z_C = 1522$ nm. Consequently, the new RESOLFT-SPIM setup has an axial resolving power that is increased by a factor of 12.3 compared to conventional SPIM.

The single virus particle shown in figure 3.15 was picked from a random position in the sample. The next experiment was intended to confirm these results in average over a large area. Therefore, the resolving power of RESOLFT-SPIM was determined for hundreds of HIV-1 particles and compared to conventional SPIM. Imaging was performed with the same parameters as for the previous experiment. In order to simultaneously extract the FWHM of a fit in axial and lateral direction to a single HIV-1 image, a 2D Gaussian function was fitted in a LabVIEW routine. A starting point of the fitting algorithm is manually selected by clicking on the center of the intensity distribution.

A typical x - z cross-section of a conventional SPIM image and the corresponding 2D Gaussian fit is shown in figure 3.16a. The images have an isotropic pixel size of 108.3 nm which results in an image size of $4.8 \times 4.8 \mu\text{m}^2$. The histograms of 260 successfully extracted FWHM values in the axial, Δz_C , and the lateral, Δx_C , dimension are shown, respectively. The fits to the normal distributions peak at $\Delta z_C = 1460$ nm and $\Delta x_C = 388$ nm. Within the boundaries of the standard deviations, these values reflect the average resolving power of a conventional SPIM microscope with this optical arrangement.

The measured values are compared to those obtained from 2D Gaussian fits to RESOLFT-SPIM images of HIV-1. The data is shown in 3.16b. The displayed example images have the same number of pixels and the same lateral pixel size as the corresponding conventional SPIM images, but the axial pixel size was kept at 25 nm. In the same manner as described before, the FWHMs of 210 valid fits in z and x , respectively, were plotted in histograms showing the count numbers of axial and lateral widths. A Gaussian fit to the normal distribution reveals an average resolving power in the axial direction of $159 \pm$

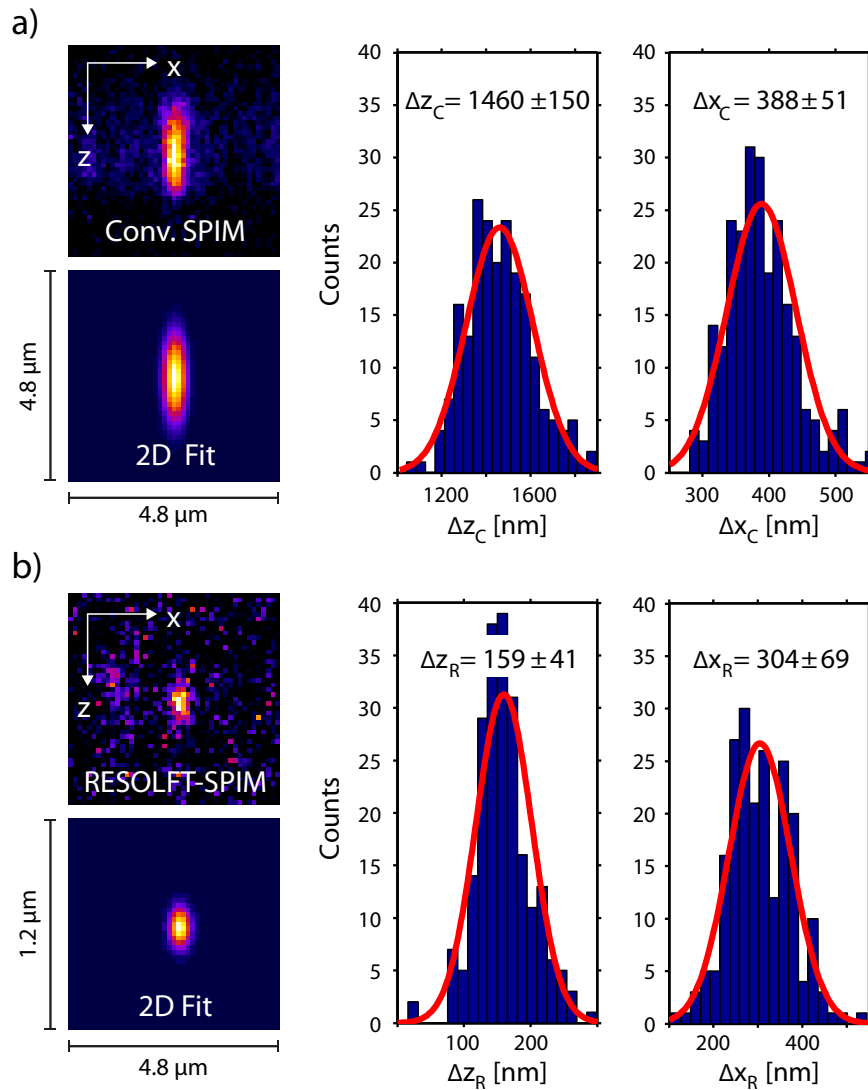


Figure 3.16: Distribution of axial and lateral FWHMs of Gaussian fits to HIV-1 particles imaged in RESOLFT-SPIM and conventional SPIM mode. a) The FWHMs in z and x were extracted from more than 200 2D fits to conventional SPIM images of single HIV-1 particles on a glass coverslip. A typical image and the corresponding fit is exemplarily shown. From a fit to the distribution of FWHMs, the peak positions and the standard deviations are determined. b) The same region was scanned at maximal off-switching power in RESOLFT-SPIM mode. 210 fits in z and x , respectively, were analyzed the same way. Here, the resolving power in z -direction averaged over the FOV is improved by a factor of 9.2. Also, the lateral resolution in RESOLFT-SPIM is improved by more than 20%. Note that for a valid fit, the 45×45 pixels of the images have different scales. In RESOLFT-SPIM images the pixel size in z is 25 nm, while the pixel size in x and the pixel size in both dimensions in conventional SPIM images is 108.3 nm.

41 nm. If the particle size is taken into account, an effective light-sheet thickness with a FWHM value of 98 nm is derived. The lateral distribution peaks at 304 nm with a standard deviation of 69 nm. In average, RESOLFT-SPIM increases the axial resolving power by a factor of 9.2 compared to the conventional SPIM mode. In addition, the mean lateral resolution is improved by more than 21%.

3.4.4 Validation of the square root law

The RESOLFT-SPIM images analyzed for figures 3.15 and 3.16 were acquired with the maximally available off-switching power. The following experiment is intended to validate the square root law (cf. equation 2.28) for the RESOLFT-SPIM technique in order to prove that also in this setup the axial resolution is in principle unlimited by diffraction. For this purpose, the resolving power of the RESOLFT-SPIM microscope is measured for different off-switching powers and constant off-switching time. As described in the previous paragraph, multiple single virion images have been fitted with a 2D Gaussian function.

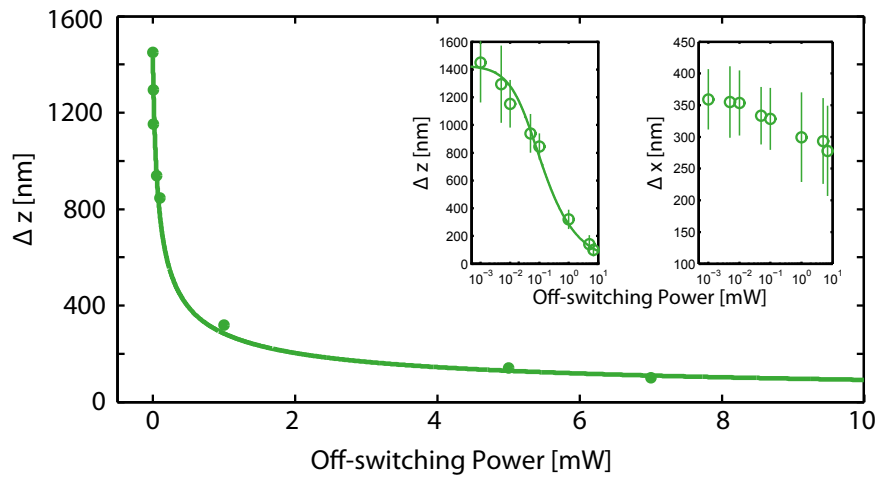


Figure 3.17: Validation of the square root law in RESOLFT-SPIM. The theoretical predicted square root dependency of the resolving power on the off-switching power is shown for the new RESOLFT-SPIM setup. For a fixed off-switching time $t_{off} = 30$ ms, the average axial FWHMs of HIV-1 particles imaged in RESOLFT-SPIM mode were determined for various off-switching powers featuring an axial zero-intensity region. The mean FWHM values are plotted versus the off-switching power in the back-focal plane of the illumination objective (green dots). A fit (green line) to the data according to equation 2.28 confirms the square root dependency. The same data and fit is shown together with error bars on a logarithmic scale in the left inset. The dependency of the lateral resolution on the off-switching power in axial direction is plotted in the right inset together with the error bars.

The lateral and axial FWHM of each fit is plotted in a histogram specific for a certain off-switching power. The average FWHM in z - and x -direction derived from Gaussian fits to each FWHM distribution is deconvolved with the particle size and plotted versus the off-switching power measured close to the back-focal plane of the illumination objective. Figure 3.17 shows the measured data along with a fit according to equation 2.28. The measured values match to the square root dependence. The mean lateral FWHM also depends on the off-switching power in the axial direction as shown in the inset in figure 3.17. This result can be explained with the increased optical sectioning capability enabled by RESOLFT-SPIM. The PSF of a single emitter in this nanoscope features a smaller width if out-of-focus light is suppressed by RESOLFT. Depending on the off-switching intensity in the axial direction relative to the saturation intensity of the fluorophores, the light-sheet thickness is reduced. Thinner optical sections cover smaller parts of the detection PSF and hence also increase the lateral resolution.

3.4.5 Rayleigh range of the RESOLFT light-sheet

This experiment was intended to measure the Rayleigh range of the effective fluorescence light-sheet which is created by switching-off RSFPs at the outer edge of the activated volume with RESOLFT-SPIM. To this end, the average axial FWHM values of imaged rsEGFP2 filled HIV-1 particles were determined at different y -positions along the applied light-sheets. The distance between two y -positions, denoted as Δy is not directly given by the setup, but it can be determined from the measured data. The data analysis of this experiment is exemplarily depicted for a particular Δy in figure 3.18a. It is assumed that at a vertical position $z'=I$ of the sample, the light-sheet hits the HIV-1 particles on the coverslip at the position of minimal beam waist along the y -direction. The sample is scanned and imaged with the same parameters as described in the single HIV-1 experiment. In the next step of the experiment, the sample is moved downwards to $z'=II$. At the position where the light-sheet hits the sample, the light-sheet thickness is increased according to equation 2.13. The sample is scanned with the same parameters as in the first step. After the affine transformation described in section 3.3.2, the maximum projections along the z -axis of both image stacks is color coded and overlapped. White dashed lines in the figure mark the start and the end of the scanned FOV for each scan step. The distance between the start positions of the two scans is equal to the distance Δy of the second scan position to the position of minimal beam waist along the optical illumination axis.

RESOLFT-SPIM and conventional SPIM scans have been performed at nine z' positions. For each scan step and each imaging mode, the axial FWHM values of around 100 imaged virions were determined by 2D Gaussian fits and added to a histogram. In figure 3.18b the average FWHM obtained from a fit to the histogram was plotted together with the standard deviation as a

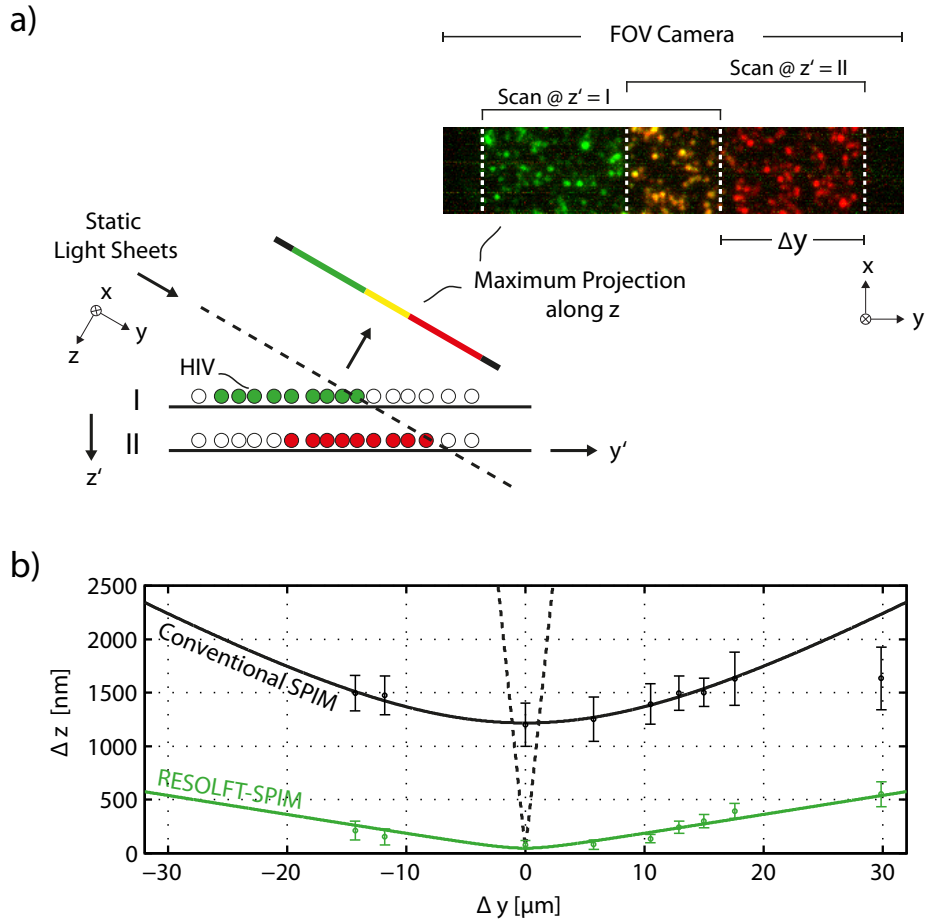


Figure 3.18: The Rayleigh range of the RESOLFT light-sheet measured on HIV-1 particles. At several positions along the optical illumination axis of the applied light-sheets, the average axial FWHM of HIV-1 was determined as described for single HIV-1 experiments. The distance Δy of the measured sample plane from the minimal beam waist position is derived as depicted in a) and explained in greater detail in the text. b) The average value of Δz together with the standard deviation was plotted versus the measured value of Δy for conventional SPIM (black dots) and RESOLFT-SPIM (green dots). Fits to the data points according to equation 2.13 reveal an increase in beam waist (FWHM) by a factor of $\sqrt{2}$ at $\Delta y = \pm 11.7 \mu\text{m}$ for RESOLFT-SPIM, and $\Delta y = \pm 19.4 \mu\text{m}$ for conventional SPIM. For reference, the beam waist at FWHM of an equivalent, theoretical Gaussian light-sheet with the same minimum value as achieved by RESOLFT is plotted versus Δy (black dashed line). RESOLFT-SPIM clearly extends the available FOV along the y direction.

function of Δy . As expected, the FWHM increases with increasing distance to the position of minimal beam waist for each imaging mode. A fit to the data points in conventional SPIM mode according to equation 2.13 adapted to FWHM values, reveals a Rayleigh range in y -direction of $19.3 \mu\text{m}$. The data point obtained at a distance of $\Delta y = 29.9 \mu\text{m}$ has not been taken into account for the fit. At this distance the light-sheet thickness is larger than the axial extent of the detection objective. From the FWHM of the HIV-1 particles only a distribution around this value is obtained and does not reflect the true thickness of the light-sheet. For $I \gg I_S$, the increase in beam waist of a RESOLFT light-sheet is well approximated by equation 2.13. A fit to the data points reveals a Rayleigh range of $11.7 \mu\text{m}$. For comparison and visualization of the benefit of RESOLFT, an equivalent Gaussian light-sheet with a theoretical Rayleigh range derived from a beam waist of 98 nm (FWHM) and equation 2.14 was added to the plot. RESOLFT clearly increases the available FOV along the y -direction. As a consequence, even specimens with dimensions larger than the FOV_y , defined by diffraction can now be imaged with a homogeneous axial resolution below the diffraction limit.

3.4.6 Resolution in a dense sample

In the following, the measured resolving power of the novel RESOLFT-SPIM is used to distinguish two or more objects located at an axial distance smaller than the diffraction limit. Dense HIV-1 samples have been prepared as described in appendix A.2. The sample was imaged with the same parameters as for the single emitter experiment following the imaging strategy described in section 3.3.1. A maximum projection of the HIV-1 sample along the y -axis is shown in figure 3.19a. For comparison, the conventional SPIM recording is shown together with the RESOLFT-SPIM projection. Plots of the normalized intensity on a vertical line through the image of two virus particles versus the axial position is shown in figure 3.19b. The objects can clearly be distinguished in the RESOLFT-SPIM mode, but cannot be seen as separated peaks in the conventional SPIM mode. Fitting a linear combination of two Gaussian profiles to the according data reveals an actual axial distance below the diffraction limit. It is worth a note, that the axial distance, here, describes the distance along the z -axis of the light-sheet and refers to a physical distance of 339 nm along the x - y' -plane on the coverslip.

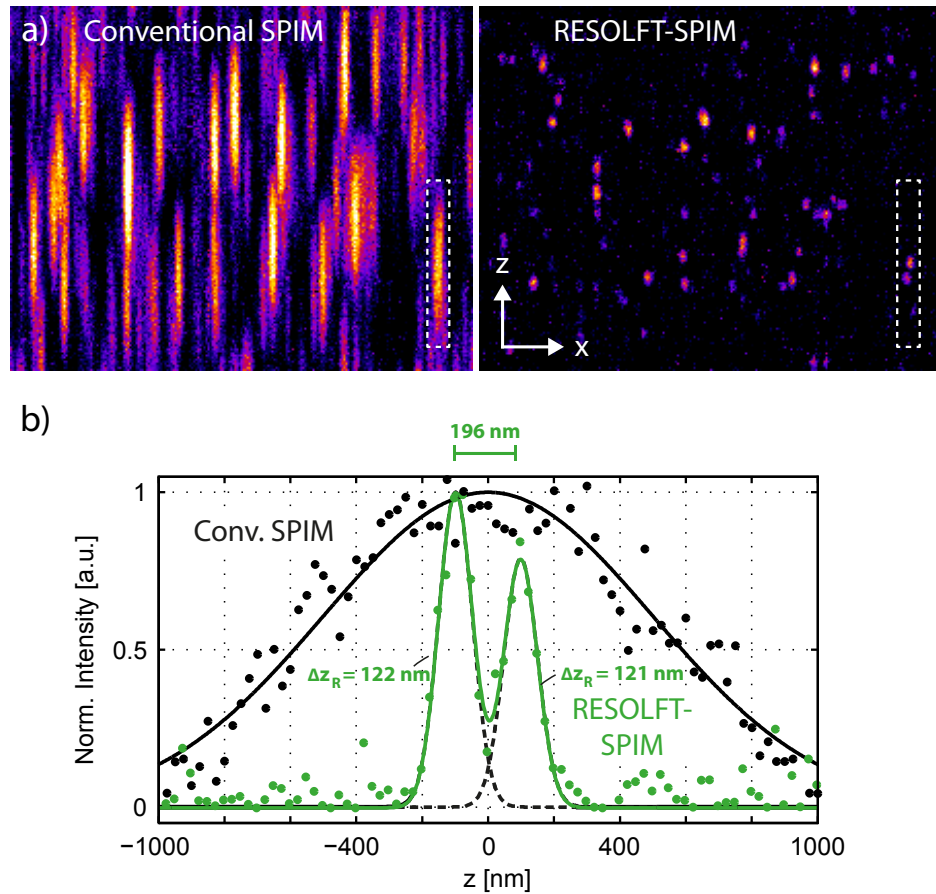


Figure 3.19: Resolving power of RESOLFT-SPIM in a dense sample. a) An x - z cross-section of the same area in a dense HIV-1 sample is shown for conventional SPIM and RESOLFT-SPIM imaging mode. Single virions are clearly separable in the RESOLFT-SPIM image, even at a distance closer than the diffraction limit, whereas they are not separable in the conventional SPIM mode. The pixel size in x and z is 108.3 nm and 25 nm, respectively, which results in an image size of $24 \times 4 \mu\text{m}^2$. b) Line profiles along the z -axis through the intensity profile marked by the white dashed borders in the images reveal two single peaks clearly separable at a distance below the diffraction-limit. The same HIV-1 virions can not be distinguished in the conventional SPIM mode.

3.5 Biological applications

In this section, the imaging capabilities of RESOLFT-SPIM setup are demonstrated on living biological samples. First, a time series of HIV-1 virions assembling on the cell membrane of an infected HeLa cell is recorded. Then, super-resolved images of RSFP-labeled constituents of the nuclear pore complex in U2OS cells are shown. Finally, a network formed by the intermediate filament protein keratin-19 was imaged in RESOLFT-SPIM with sub-diffraction axial resolution. All images presented in this section are recorded with a 10x/0.3 NA illumination objective and a 40x/0.8 NA detection objective.

3.5.1 HIV-1 assembly in living HeLa cells

In the previous sections, it has been shown that RESOLFT-SPIM enables the separation of virus particles at distances below the diffraction limit. In the experiment presented here, this advantage is exploited for resolving HIV-1 assembly sites in a living cell. The process of assembly occurs at the plasma membrane of infected cells. It is driven by the polyprotein Gag whose sub-units can be fluorescently labeled. The dynamics of the assembly have already been investigated using a wide-field microscope and TIRF illumination [80], which, however, restricted the observable locations to a small volume near the glass coverslip. In contrast, RESOLFT-SPIM offers a widely homogeneous effective light-sheet throughout the entire cell sample. This in principle enables the observation of assembly sites at any position on the cell membrane with sub-diffraction axial resolution.

To prove this statement, HeLa cells have been prepared for imaging as described in appendix A.2. In the transfected cells, assembly sites enclosing up to 1000 rsEGFP2 proteins are formed. The onset of their formation is dependent on the individual cell and ranges between 12-18 hours. A mechanically stable setup and photostable fluorophores are therefore prerequisites for a successful measurement. The transfected cells were mounted on the platform in the RESOLFT-SPIM specimen chamber. A temperature of about 33°C in the specimen chamber and an imaging medium containing HEPES provides an appropriate environment for long-term measurements. The sample was then scanned through the static light-sheets according to the scheme presented in section 3.11. For each scanning step a RESOLFT-SPIM and a conventional SPIM image has been taken. A total range of 40 μm was scanned with a step size of 50 nm. The RSFPs were activated with a power of 260 μW for 10 ms. Off-Switching was performed with a power of 3.8 mW that was applied to the sample for 30 ms. The residual activated RSFPs were readout for 40 ms with a power of 160 μW . With a time interval of 10 minutes five image stacks have been recorded, which sums up to a total frame number of 8000 not including

the extra images taken to avoid the afterglow effect in the RESOLFT-SPIM image and for background reference.

Figure 3.20 displays the results. An x - y projection of the stack at $t = 0$ serves as an overview image of the infected cell. Its approximate boundaries are highlighted. Partially overlapping diffraction-limited spots of HIV-1 assembly sites are visible. The advantage of RESOLFT-SPIM compared to the conventional imaging mode is clearly demonstrated in x - z projections of the stacks. With the new technique, images of single assembly sites exhibiting an axial extent below the diffraction-limit can be found at any time point

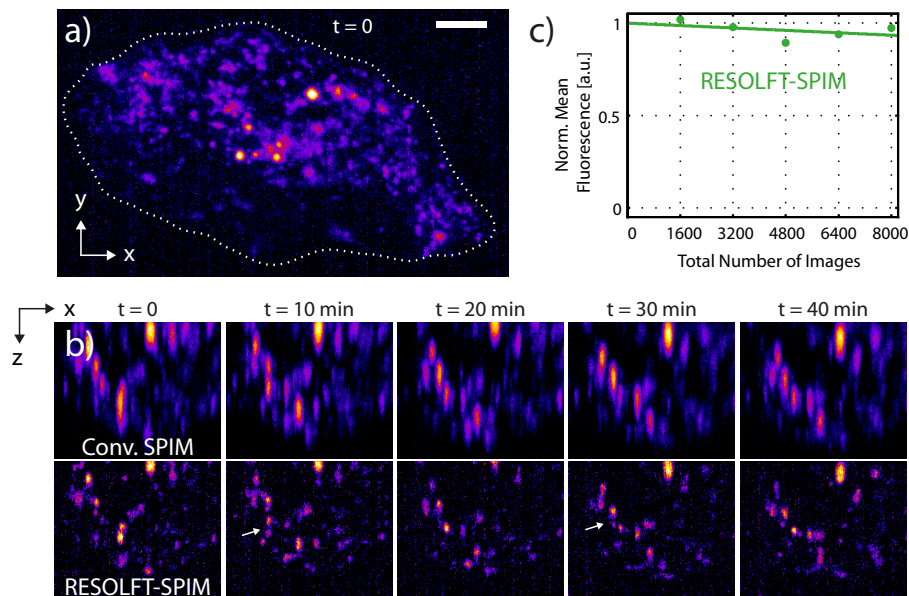


Figure 3.20: Live-cell RESOLFT-SPIM imaging of individual HIV-1 assembly sites. a) The HIV-1 assembly at the cell membrane of a HeLa cell was recorded over more than 40 min in RESOLFT-SPIM and conventional SPIM mode. An x - y projection of a RESOLFT-SPIM image stack taken at a time point $t = 0$ serves as an overview image. A white dashed line marks the boundaries of the living cell. A total volume of $45 \times 26 \times 7.5 \mu\text{m}^3$ was recorded and the voxel size is set to $108.3 \times 108.3 \times 50 \text{ nm}^3$. Scale bar: $5 \mu\text{m}$. b) The maximum intensity projections along the illumination axis of five image stacks taken in conventional (top row) and RESOLFT-SPIM mode (bottom row) are shown. The images were cropped to a size of $19 \times 7.5 \mu\text{m}^2$. The same cell was recorded at a time interval of 10 min. The superior axial resolution of RESOLFT-SPIM reveals single HIV-1 assembly sites that cannot be distinguished in diffraction-limited SPIM. Two of these regions in the cell are highlighted by white arrows. Single HIV-1 assembly sites imaged with RESOLFT-SPIM can be tracked in three dimensions over time. c) Light-sheet illumination and the low switching fatigue of rEGFP2 proteins contribute to the ability to record a total number of 8000 frames of the same cell without significant reduction in mean fluorescence. The data points are fitted with a linear function.

during the course of the experiment. In contrast, neighboring assembly sites cannot be resolved in the axial direction in the standard SPIM mode. In addition, RESOLFT-SPIM also allows for tracking of virus particles in dense regions over a long period of time. Its optical sectioning capabilities and low power operation together with the low switching fatigue of rsEGFP2 enables a recording without significant reduction in fluorescence. In Figure 3.20c the mean fluorescence is plotted versus the number of acquired images. A linear fit to the data points reveals a drop in fluorescence to 93% after 8000 frames. This indicates that it would be possible to acquire a further multiplicity of 3D image stacks of the same region in this setup.

3.5.2 Nuclear pore complexes of living U2OS cells

In the following, the imaging capabilities of RESOLFT-SPIM are demonstrated on nuclear pores of living human cells. Nuclear pores are tiny holes in the envelope of the cell nucleus. The protein structure called the nuclear pore complex (NPC) that surrounds each pore is generally thought to play an important role in the import and export of macromolecules through the pores. Each NPC has a highly conserved structure consisting of many distinct protein species, called nucleoporins. In this experiment, the nucleoporin Nup214 has been fused with rsEGFP(N205S). In order to enhance the fluorescence signal, a single target protein was fused with three rsEGFP(N205S) molecules. Details about the cloning strategy and the sample preparation are described in appendix A.2.

The density of pores on the nuclear envelope depends on the cell type and the stage in the life cycle. Highly active and differentiated cells have the greatest density. Human U2OS cells are a well-established experimental system for studying NPCs. A typical U2OS cell features a density of 5.7 ± 2.7 NPCs/ μm^2 [104]. Assuming a detection PSF with a lateral FWHM of 390 nm as derived from measurements on gold colloids (cf. section 3.4.2), some single nuclear pores are expected to be distinguishable from their surrounding in x - y projections of a nucleus of this cell type. For these reasons, U2OS cells were used for imaging in this experiment.

RESOLFT-SPIM images were taken following the general imaging procedure described in section 3.3.1, and compared to conventional SPIM images of the same sample region. Fluorophores were activated with the UV laser at a power of 320 μW for 30 ms. After a relaxation time of 2 ms, off-switching was performed at a power of 7 mW for 100 ms. Then, two images with an exposure time of 10 ms each were taken to avoid the afterglow effect (cf. appendix A.1) and to get a background image. Subsequently, the residual activated rsEGFPs were readout for 50 ms with a power of 350 μW . At the same time the camera was exposed and a RESOLFT-SPIM image was recorded. Thereafter, a diffraction-limited SPIM image is taken with the same parameters for activation and readout before the stage scanner moved to the next position. A

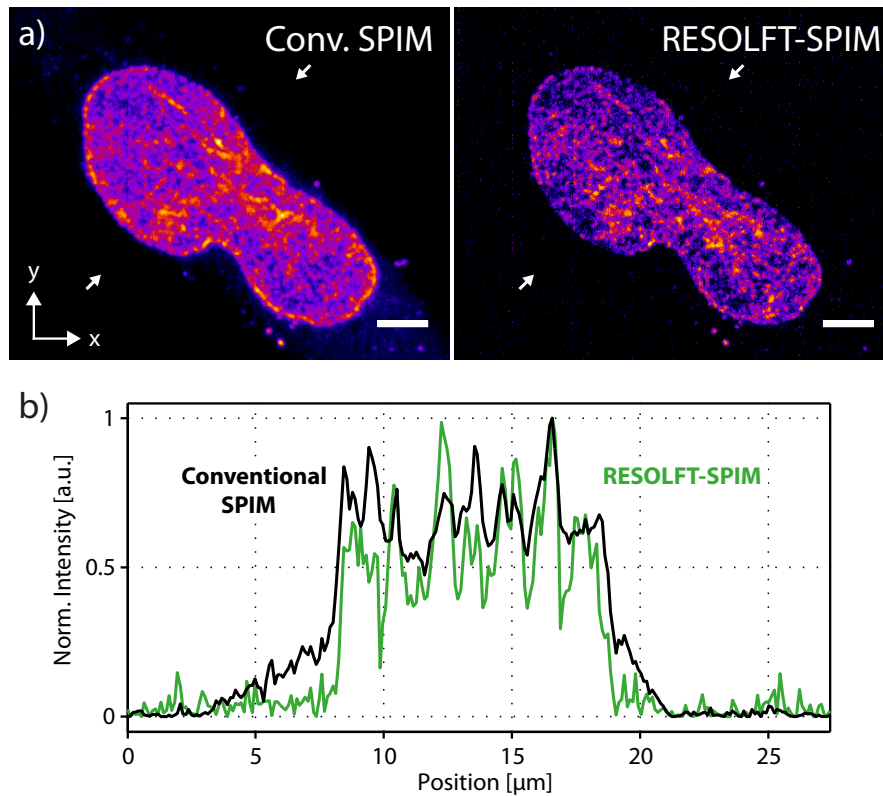


Figure 3.21: Improved lateral contrast in a biological sample by RESOLFT-SPIM. a) Image stacks of a living U2OS cell expressing Nup214-3x-rsEGFP(N205S) are taken in conventional SPIM (left) and RESOLFT-SPIM (right) imaging mode and projected along the z -axis. For display, a background of 10% of the maximum value in each image was subtracted. Scale bar: 5 μm . b) The normalized intensity profiles on a line between the white arrowheads in each image reveal an enhanced contrast in RESOLFT-SPIM (green) compared to the conventional SPIM mode (black). RESOLFT enables sub-diffraction optical sectioning by switching off out-of-focus light.

total range of 60 μm was scanned with a step size of 50 nm, resulting in an image plane distance of 25 nm in the affine transformed image stack and a total number of 4800 images.

Figure 3.21a shows an x - y projection of a scan through a cell in conventional SPIM and RESOLFT-SPIM mode. The detection path had an overall magnification of $M = 60$, which translates the pixel size of the detector into a lateral sampling size of 108.3 nm in the sample. In both images 10% of the maximum intensity value was subtracted as background. Comparing the projections of the two imaging modes, single nucleoporins can be found in both images. However, features appear clearer in the RESOLFT-SPIM image. Figure 3.21b shows the plotted normalized pixel intensity along lines through the nucleus. The ends of the line profiles are marked with white arrows in the im-

ages. The plot confirms that the background signal between single peaks is indeed reduced compared to the conventional SPIM image.

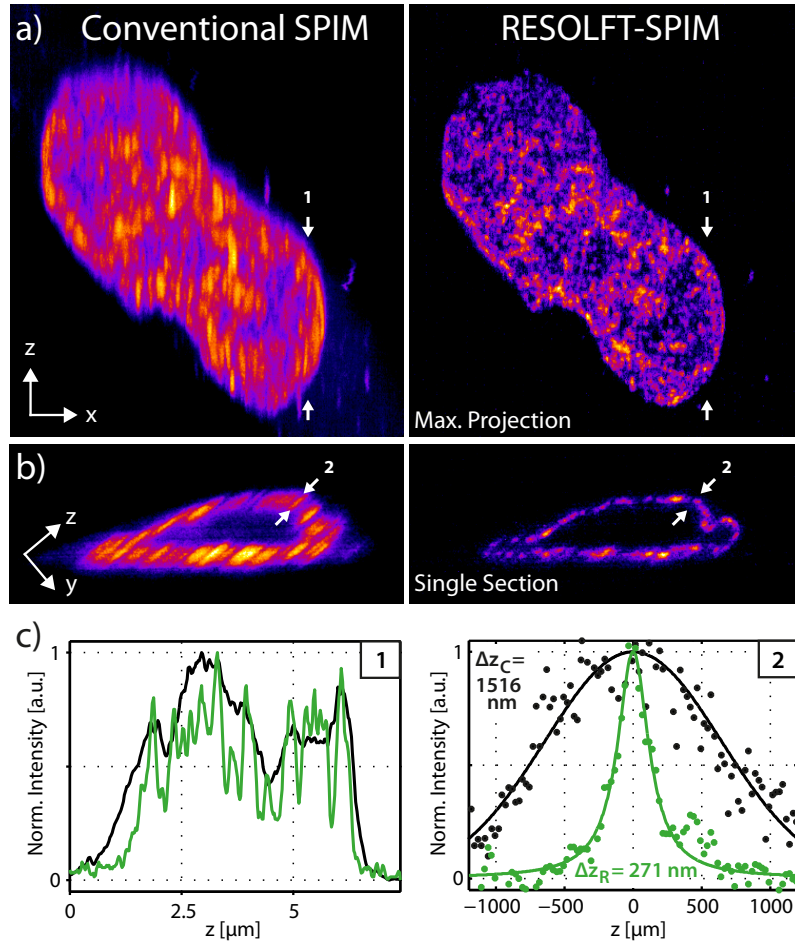


Figure 3.22: Live-cell imaging capabilities of RESOLFT-SPIM demonstrated on nuclear pore complexes. A stack of 400 images was recorded with a step size of 50 nm, which results in a total volume of $43 \times 34 \times 20 \mu\text{m}^3$. The voxel size is set to $108.3 \times 108.3 \times 50 \text{ nm}^3$. a) The maximum intensity projection along the illumination axis y of a living U2OS cell expressing Nup214-3x-rsEGFP(N205S) is shown for conventional SPIM (left column) and RESOLFT-SPIM (right column). A line profile along z of the region between the arrowheads is plotted in c). Enabled by an effective light-sheet thickness below the diffraction limit, RESOLFT-SPIM (green line) reveals distinct peaks which cannot be distinguished in diffraction-limited conventional SPIM (black line). b) In a single y - z section through the nucleus the resolution enhancement by RESOLFT is highlighted. Note that for display the image was rotated by 30° around the x -axis. d) A line profile through a nuclear pore complex marked in b) is plotted for the diffraction-limited SPIM (black dots) and RESOLFT-SPIM (green dots) imaging mode. A Gaussian (black) and Lorentzian fit (green) to the conventional SPIM and RESOLFT-SPIM data points, respectively, reveals an increase in axial resolution of more than a factor of 5 for RESOLFT-SPIM.

In order to test whether the RESOLFT-SPIM nanoscope is able to separate features along the z -axis that cannot be distinguished in the diffraction-limited conventional SPIM approach, the corresponding x - z maximum projections of the same data stack are shown in figure 3.22a. The RESOLFT light-sheet image clearly exhibits an increased resolution along the axial direction. Enabled by an effective light-sheet with sub-diffraction thickness, single nucleoporins are also separable along the z -axis in RESOLFT-SPIM, whereas the highly anisotropic PSF in the conventional SPIM mode severely blurs the image. A single y - z slice of the nucleus imaged with RESOLFT-SPIM is shown in figure 3.22b in comparison to the standard SPIM mode. The slice was rotated around the x -axis so that the coverslip to which the nucleus is attached is oriented horizontally in the image. Also in this view the increase in axial resolution is evident. RESOLFT-SPIM reveals the boundaries of the nucleus since the Nup214-3x-rsEGFP(N205S) fusion proteins on its surface can be imaged at sub-diffraction axial resolution. In contrast, the anisotropic PSF in the conventional SPIM mode blurs the image mainly in the z -direction. Line profiles along the z -axis in the x - z projection and the y - z slice confirm the qualitative results (cf. figure 3.22c). Across the nucleus the normalized intensity profile of the RESOLFT-SPIM image exhibits separable peaks that cannot be resolved in the conventional SPIM mode. A Lorentzian fit to the normalized data points of an axial intensity profile of a single Nup reveals an increase in resolution by a factor of 5.6.

3.5.3 Cytoskeleton of living HeLa cells

In a further experiment, the imaging capabilities of RESOLFT-SPIM were demonstrated on the cytoskeleton of living HeLa cells. In general, the cytoskeleton determines the mechanical properties of cells and consists of a complex filament network. One of the filament-forming proteins is keratin-19 which was tagged with an RSFP for this experiment. To this end, HeLa Kyoto cells expressing keratin-19-rsEGFP(N205S) have been prepared as described in appendix A.2. For imaging, the general sequence that has been described in section 3.3.1 was applied with the following settings: The RSFPs in the sample were activated with 405 nm light at a power of 350 mW for 10 ms. The double-sheeted off-switching laser with a power of 6.9 mW was applied for 100 ms to switch the RSFPs in the periphery of the detection focal plane into the off-state. After two clearing images with a 10 ms exposure time each, fluorophores that remained activated in the very center of the detection volume were readout with 488 nm light for 60 ms at a power of 150 μ W. In order to directly visualize the improvement in resolution, a conventional SPIM image is subsequently taken at the same scan position. The RSFPs were thereby activated and readout with the same light doses and exposure times as for the RESOLFT-SPIM image. The off-switching laser was not used in this case which results in a diffraction-limited SPIM image. A total range of 60 μ m was

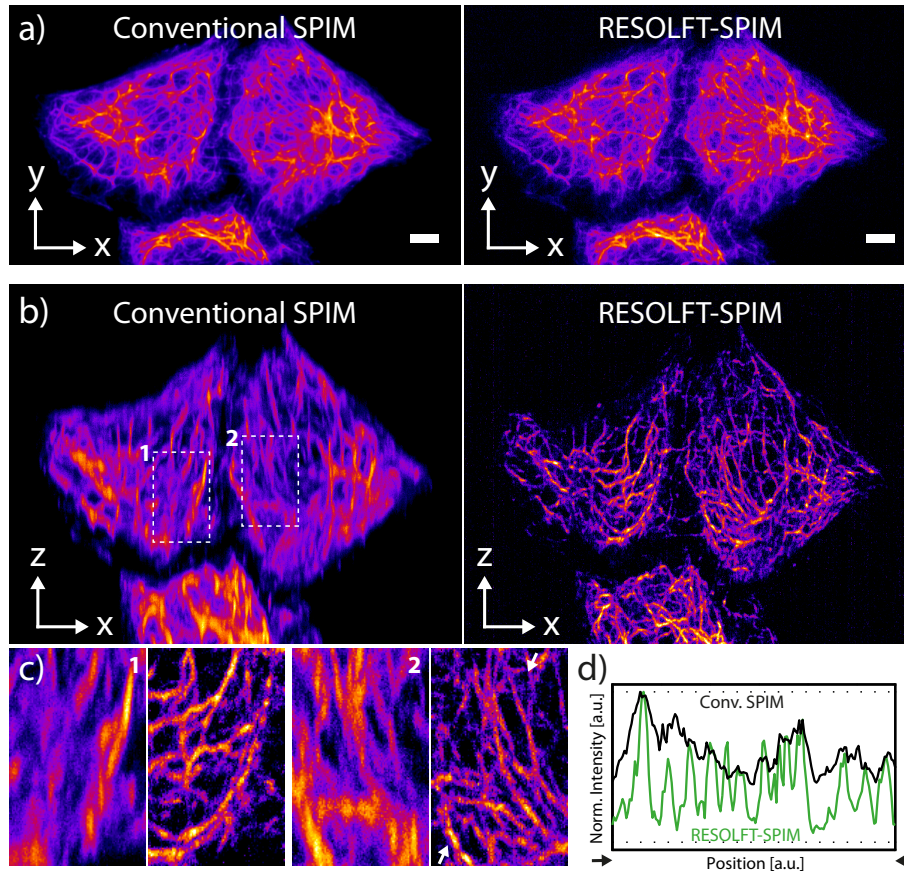


Figure 3.23: Conventional SPIM and RESOLFT-SPIM images of the keratin-19 network in living HeLa cells. The keratin-19 fibers have been tagged with rsEGFP(N205S). A stack of 1200 images per imaging technique was recorded with a step size of 50 nm, which results in a total volume of $82 \times 47 \times 30 \mu\text{m}^3$. The voxel size is set to $108.3 \times 108.3 \times 50 \text{ nm}^3$. a) The summed image of all x - y RESOLFT-SPIM slices contains the same lateral information as the diffraction-limited conventional image. Scale bar: $5 \mu\text{m}$. b) The superior resolving power of RESOLFT-SPIM is demonstrated in x - z projections of the same image stack. The RESOLFT-SPIM image displays much thinner features than conventional SPIM. Keratin-19 strands are clearly separable even in dense areas. c) Magnified views of two areas in the sample highlight the imaging capabilities of RESOLFT-SPIM. The images show an x - z area of $10.7 \times 7.8 \mu\text{m}^2$. d) Normalized intensity profiles along a line between the white arrowheads in the magnified image 2 reveal single peaks for separated keratin-19 strands in the RESOLFT-SPIM imaging mode (green) that cannot be resolved in conventional SPIM (black).

scanned with a step size of $\Delta y' = 50$ nm resulting in an image stack of 4800 images. For display the stacks have been sheared as explained in section 3.3.2.

Figure 3.23a shows conventional SPIM and a RESOLFT-SPIM images of the same area in the sample, which were obtained by summing up all x - y slices of the volume scan through the cell according to the imaging mode. The labeled keratin-19 network of the cell is clearly visible in both images. Also signals originating from fine structures in the periphery of the cells are detected and contribute to the image. This is an evidence for a central plane in the RESOLFT-SPIM off-switching pattern that indeed has an intensity close to zero. Moreover, whole cells can be imaged in RESOLFT-SPIM with an adequately high sampling rate without a visible drop in intensity, which also indicates a low switching fatigue of the RSFPs.

The superior resolving power of RESOLFT-SPIM compared to the conventional SPIM equivalent is demonstrated in x - z cross-sections of the same cell in figure 3.23b. For display, 10% of the maximum intensity value in each image was subtracted. The RESOLFT-SPIM image reveals much thinner features of the cytoskeleton than the conventional SPIM image. Keratin-19 strands can be clearly distinguished even in dense regions of the sample. A closer view on two areas of a cell further highlights the resolving power of RESOLFT-SPIM compared to the diffraction-limited equivalent. Magnified images of both techniques are displayed side-by-side in figure 3.23c. A normalized intensity profile along a line between two arrowheads in one of the zooms reveals single peaks for separable keratin-19 fibers enabled by RESOLFT-SPIM. The same structures are blurred in the diffraction-limited image recorded in the conventional SPIM mode.

Summary and discussion

In this thesis a new microscopy technique, called RESOLFT-SPIM, is presented, that symbiotically combines the advantages of RSFP-based RESOLFT nanoscopy and SPIM. RESOLFT-SPIM exploits long-lived dark and fluorescent states provided by reversibly switchable fluorophores to gain sub-diffraction axial resolution with very low light intensities that allow for long-term imaging. In combination with SPIM, RESOLFT reduces the axial extent of a light-sheet below the diffraction limit and enables detailed non-invasive imaging of living specimens. Furthermore, the RESOLFT-SPIM concept offers the first approach on improving the axial resolution in RSFP-based nanoscopy. In the following, the results presented in chapter 3 are summarized and discussed.

Imaging with sub-diffraction axial resolution

The resolving power of the RESOLFT light-sheet microscope was characterized on HIV-1 particles enclosing rsEGFP2 proteins. On a single virion, the FWHM of a Gaussian fit to the line profile in axial direction is reduced from a value of 1522 nm for a diffraction-limited SPIM to 124 nm in RESOLFT-SPIM. This is equal to an increase in resolution by a factor of 12.3. The axial resolution in RESOLFT-SPIM, which is, at least conceptually, unlimited, is superior to any SPIM variant which does not truly break the barrier set by diffraction, especially SPIM in combination with Bessel-beam[114] or structured illumination [114, 39]. Previously reported point-scanning RESOLFT setups have shown to increase the lateral resolution in biological cells by not more than a factor of 5 using the same RSFP type [46]. However, super-resolved images on HIV-1 particles, in particular, have not been demonstrated with these techniques yet. In another comparison, RESOLFT-SPIM clearly outperforms the previous STED-SPIM approach, where a gain in axial resolution by a factor of less than 1.5 was reported for dye-filled particles at the expense of much higher light doses[38].

In a further experiment, a detailed analysis of the distribution of FWHM values across the entire homogeneously illuminated FOV_x of 222 μm revealed an average FWHM in the axial direction of 159±41 nm. If the average HIV-1 particle size of 160 nm [151] is taken into account, a RESOLFT light-sheet thickness with a FWHM value of 98 nm is obtained. The capability to create optical sections with sub-100 nm thickness is similar to the axial resolving power of a typical TIRF microscope [34], however, with an eminent differ-

ence: In contrast to TIRF that is conceptually bound to applications close to the coverslip surface, RESOLFT-SPIM offers sub-diffraction axial resolution in any slice throughout the entire specimen and can thus be applied to a broad range of (not just) cell biological questions. Parallelized fluorescence correlation spectroscopy with RESOLFT light-sheet illumination may allow to precisely characterize diffusion processes in a sub-diffraction volume. Another potential application is the quantitative analysis of protein complexes imaged in a volume defined by the RESOLFT light-sheet.

In order to show that the axial resolution in RESOLFT-SPIM is not conceptually limited, the theoretically predicted square root dependency of the resolution on the off-switching intensity [54] was determined in the RESOLFT-SPIM setup on HIV-1 particles. A square root fit to the measured data points confirms this dependency also for the novel technique. It is concluded that, for photostable RSFPs, the axial resolution of the presented RESOLFT-SPIM setup is mainly limited by the available laser power. As an interesting side effect, the average lateral resolution of RESOLFT-SPIM measured on HIV-1 is increased by up to 21% compared to the same virions imaged with diffraction-limited SPIM. This result can be explained with the increased optical sectioning capability enabled by RESOLFT-SPIM. The measured dependency of the lateral FWHM on the off-switching power in the axial direction supports this statement. Similar observations have been reported in other SPIM approaches [38].

The increased resolving power is demonstrated for two virions located at a distance well below the diffraction-limit. RESOLFT-SPIM clearly separates particles with an axial distance of 196 nm in the object space which are not seen as distinct objects in diffraction-limited SPIM images.

Imaging with large field of views

The RESOLFT-SPIM concept is demonstrated in a versatile setup, that allows to mount various objective combinations in order to adjust the light-sheet parameters to the biological questions that should be addressed. A low NA objective lens offers a homogeneously illuminated field of view that is, in its width, only limited by the size of the camera sensor. Large specimens with a lateral extent of 200 μm and more can be imaged with sub-diffraction axial resolution in a highly parallelized manner. Thinner light-sheets with a FWHM of 95 μm can be achieved with higher NA objectives. The FOV along the direction of illumination is in general proportional to the square of the light-sheet thickness for Gaussian-like beams. RESOLFT-SPIM has demonstrated to overcome this limit and to increase the depth of field for these light-sheets. For single optical sections, a FOV of more than $200 \times 20 \mu\text{m}^2$ became available by RESOLFT. With this technique even extended biological specimens can now be imaged with a homogeneous sub-diffraction light-sheet

thickness. The maximal y' -range that can be imaged with this FOV is only limited by the implemented stage scanner, which is 500 μm in this case.

Long-term imaging

The orthogonal objective arrangement in RESOLFT-SPIM is advantageous especially for the investigation of processes in living organisms. Since only thin sections of the sample are selectively illuminated at a time, photodamage and phototoxicity of the fluorophores and the specimen is reduced compared to point-scanning approaches. In favor by the low saturation intensities of RSFPs, the light exposure of the sample is kept at a minimum. Mainly for these reasons, light-sensitive physiological processes such as the formation of HIV-1 budding sites in infected cells can be imaged with RESOLFT-SPIM over more than 40 minutes. In this time period, 8000 images of the same 3D volume were recorded without significant reduction in fluorescence. On the technical side, the monolithic design of the objective mount unit contributes to reasonably stable imaging conditions during the measurement.

High-speed Imaging

Due to the highly parallelized illumination and detection regime, the acquisition speed of RESOLFT-SPIM is superior to point-scanning approaches. Recent advances in the development of novel RSFPs with fast switching kinetics contribute to this advantage. The acquisition time for a single slice of the sample was set to 94 ms for the applied laser powers and sub-100 nm axial resolution. Neglecting the pure technical parameter of stage movement, RESOLFT-SPIM consequently records a volume of $80 \times 40 \times 30 \mu\text{m}^3$ twice as fast as a confocal point-scanning microscope (sampling volume: $80 \times 80 \times 200 \text{ nm}^3$, dwell time: 3 μs) with a 4 times higher axial sampling rate. For specimens labeled with rsEGFP(N205S) the RESOLFT-SPIM acquisition rate is still higher than the point-scanning approach but lower than for rsEGFP2 samples since in this case off-switching is performed three times longer at the same power. Shorter off-switching periods together with higher off-switching powers lead to a similar increase in resolution in RESOLFT-SPIM. However, lower light doses are preferred which keeps photobleaching at a low level as demonstrated in this thesis. The advantage of parallel data acquisition can be fully harvested if the step response time of the stage scanner is tuned for stable high-speed applications.

Live-cell imaging

For the first time, a light-sheet fluorescence microscope with in principle diffraction-unlimited axial resolution is demonstrated in 3D imaging of living cells. Besides the recording of HIV-1 assembly as mentioned before, the

new nanoscope is applied to study nuclear pore complexes in living U2OS cells. The investigation of the structure of nuclear pores and their function is in the focus of current research [144]. In the new setup, a biocompatible, temperature controlled specimen chamber and buffered imaging medium provide near-physiological conditions for the sample.

RESOLFT-SPIM clearly separates single nuclear pore complexes in U2OS cells in contrast to diffraction-limited SPIM recordings of the same area in the sample. The nucleoporin Nup214 were tagged with a complex of three rsEGFP(N205S) proteins with the primary goal to enhance the image contrast in the axial direction. On this sample, it is shown that optical sectioning with sub-diffraction light-sheet thickness also improves the contrast in the lateral dimension. For this RSFP species and the available off-switching laser power, RESOLFT increases the axial resolution in the images of more than a factor of 5. A resolving power of RESOLFT-SPIM below 100 nm as it was demonstrated for rsEGFP2 labeled virions, is in the range of the axial extent of nuclear pores which potentially makes the constituents on the outer and inner part of the pore separable in rsEGFP2-labeled samples.

Furthermore, RESOLFT-SPIM is shown on the cytoskeleton of a living cell. The gain in axial resolution is used to clearly separate single keratin-19 strands in dense regions of the sample that are not seen as distinct in the diffraction-limited SPIM equivalent. On RESOLFT-SPIM images of keratin-19 fibers it is demonstrated that sub-diffraction z -resolution is possible while at the same time the full information about the sample structure is maintained.

Since RESOLFT-SPIM applies the same wavelength for off-switching and readout, both light-sheets are expected to show similar scattering properties inside samples with inhomogeneous refractive indices. This fact renders the RESOLFT light-sheet imaging more robust compared to other super-resolution concepts that employ different wavelengths. Thus, it bares the potential for applications in thicker living specimens, which can be cell tissues or even whole animals.

Outlook

The RESOLFT light-sheet microscope has been demonstrated to enable fast 3D imaging with sub-diffraction axial resolution. Various living samples labeled with one of the recently developed rsEGFP variants were recorded at low light levels. In future projects the existing RESOLFT-SPIM setup could potentially be equipped with an option for multi-color applications with resolutions below the diffraction-limit. Recordings with spectrally distinct RSFPs allow for colocalization studies in sub-diffraction volumes that may answer important biological questions. A possible second fluorophore species for two-color RESOLFT-SPIM is the very recent RSFP rsCherryRev1.4 with an emission peak that is spectrally well separable from the emission peaks of the rsEGFP variants. This red-emitting fluorophore has already been imaged in combination with rsEGFP(N205S) in a point-scanning and a parallelized RESOLFT setup [99]. In order to add this dual-color option to the existing RESOLFT-SPIM setup, at least one additional laser with a wavelength around 590 nm for off-switching and readout needs to be implemented. Both RSFP species could be activated simultaneously with the existing UV laser. Fluorescence can either be readout sequentially [99] or simultaneously by projecting the signals onto different areas on the same camera chip.

Furthermore, RESOLFT-SPIM can be equipped with an option to additionally increase the lateral resolution to regions below the diffraction limit. Since the RESOLFT-SPIM setup employs independent beam paths for illumination and detection of the sample, the same basic principles that lead to conceptually diffraction-unlimited lateral resolution in microscopes with wide-field detection can also be applied to RESOLFT-SPIM. One possible approach combines RESOLFT-SPIM with the previously demonstrated parallelized RESOLFT technique [20]. Light sheet based activation, off-switching and readout of RSFPs could be implemented through the illumination objective lens, which enables sub-diffraction axial resolution as shown in this thesis. The off-switching pattern characteristic for the parallelized RESOLFT approach is applied to the specimen through the detection objective lens which potentially leads to an additional increase in lateral resolution beyond the diffraction barrier in the system. The combination of these techniques has the potential to provide isotropic resolution below 100 nm since each of the methods per se has been demonstrated to feature a resolving power in this region. As for the symbioses of RESOLFT and SPIM, the advantages of both, RESOLFT-SPIM and parallelized RESOLFT are conserved. In addition, also this combined approach can be upgraded with a multi-color option.

The concepts of RESOLFT and SPIM have both been developed very recently. Despite their great contributions to biomedical research already in early years, the full potential of each of these techniques is yet about to be maximized. In this course, also the combined technique of RESOLFT-SPIM may take advantage of further advances in electronics, biochemistry, and optics within the next years. Scientific cameras with higher quantum yield and minimal readout noise increase the potential of capturing even weakly expressing specimens. Moreover, the ongoing development towards faster switching RSFPs may trigger RESOLFT-SPIM recordings of even faster processes in the sample. In addition, further enhancements of brightness and photostability of these fluorophores will keep the signal-to-noise ratio in RESOLFT-SPIM images at a constant high level even at faster switching rates. Also, new lenses and other optical elements increase the pool of objective combinations for RESOLFT-SPIM.

All these innovations eventually contribute to a microscope that is able to keep up with the desire of scientists for fast 3D imaging with isotropic spatial resolution on the molecular level. Ideally, large areas of living cells are recorded at low light intensities. Some of these goals have already been achieved with recent developments. Others have not yet become a reality. Many diverse features of nature are hence still hidden, but are on the verge of being uncovered.

Appendix

A.1 Afterglow effect

Although the camera is not active during activation and off-switching of the RSFPs in the sample, some photons emitted by RSFPs upon illumination with the off-switching pattern are converted into signaling electrons on the sensor. This so called afterglow effect of the sCMOS camera leads to severe background noise in the RESOLFT-SPIM image, if the sensor is read out directly after the off-switching process. The effect is characterized using the ORCA Flash 4.0 camera. The results are shown in figure A.1. Three images have been taken after the off-switching laser pulse. The intensity averaged over the entire image was normalized and plotted versus the applied off-switching power. The signals recorded in the image after the off-switching process show an exponential dependency on the applied power. This effect is reduced for the second and third image. For RESOLFT-SPIM, the first image after the off-switching process is discarded. The recorded signals are not dependent on the exposure time of the camera as shown in figure A.1b. The acquired signal increases if the off-switching laser is applied for a longer period of time.

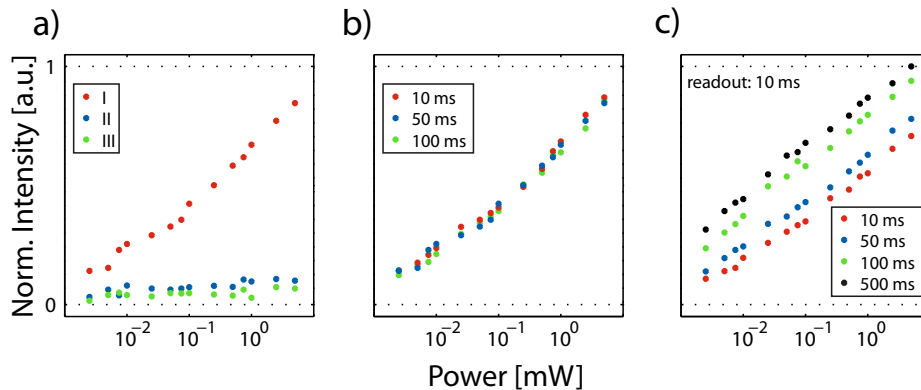


Figure A.1: Characterization of the afterglow effect. The normalized mean intensity of the acquired images after the off-switching process is plotted versus the off-switching power. The images were analyzed for a variable number of images taken after the off-switching process (a), different exposure times (b), and different off-switching times (c).

A.2 Sample preparation

In the RESOLFT-SPIM setup a variety of samples has been imaged. Here, the important aspects of their preparation are summarized.

Gold colloids on a glass coverslip

Gold colloids have been used to characterize the zero-intensity pattern and the detection PSF in the RESOLFT-SPIM setup. Details of the experiment are described in section 3.4.2. A standard round glass coverslip ($\varnothing = 5$ mm) was cleaned with absolute ethanol and air-dried. The coverslip was pressed on a piece of plastic paraffin film to prevent it from moving during the sample preparation. A 10 μ l drop of poly-l-lysine (Sigma Aldrich, St. Louis, MO) was incubated for 10 minutes on the coverslip and then carefully rinsed with ddH₂O. Then, gold colloids ($\varnothing = 80$ nm, BBI international, Grand Forks, ND) have been diluted at a ratio of 1:2 in ddH₂O, followed by passive absorption to the coated coverslip for 10 minutes. Finally, the coverslip was again carefully rinsed with ddH₂O. The gold colloid samples in this thesis have been imaged in FluoroBrite Dulbecco's modified Eagle's medium (DMEM) (Life Technologies, Carlsbad, CA).

HIV-1 particles on a glass coverslip

Single HIV-1 particles enclosing rsEGFP2 proteins have been used in the RESOLFT-SPIM microscope to measure its resolving power, to validate the square root law and to determine the Rayleigh range of the effective light sheet. Details are described in sections 3.4.3, 3.4.4, 3.4.5 and 3.4.6. A standard round glass coverslip ($\varnothing = 5$ mm) has been cleaned with absolute ethanol and air-dried. The coverslip was pressed on a piece of plastic paraffin film to prevent it from moving during the sample preparation. Then, a drop of HIV-1 particles diluted in PBS was incubated on the coverslip for 10 minutes. The final virion density on the coverslip was adapted to the goals of the experiment. To prevent photobleaching of rsEGFP2 proteins, the sample was covered with aluminum foil during incubation. Subsequently, the coverslip is carefully rinsed with phosphate buffered saline (PBS). In the experiments presented in this thesis, HIV-1 samples were imaged at room temperature in PBS or FluoroBrite DMEM medium (Life Technologies, Carlsbad, CA).

HeLa Kyoto cells transfected with pCHIV

HeLa Kyoto cells were grown in DMEM (Life Technologies, Carlsbad, CA) containing phenol red supplemented with 10% FBS and 1% sodium pyruvate. For imaging $4 \cdot 10^4$ cells were seeded on round coverslips ($\varnothing = 5$ mm) placed in a well of a 24-well plate. 24 hours after seeding, the cells were transiently

transfected with pCHIV and pCHIV-rsEGFP2 (0.6 µg each) using 3.6 µl of the transfection reagent XtremeGene9 (Hoffmann-La Roche, Basel, Switzerland) according to the manufacturer's guideline. The cells were imaged 15-24 hours after transfection without further treatment in FluoroBrite DMEM medium (Life Technologies, Carlsbad, CA) supplemented with 25 mM HEPES at 33°C for up to 15 hours. To prevent vaporization of the imaging medium, 10 ml of mineral oil (M5310, Sigma-Aldrich, St. Louis, MO) were added to the medium-filled specimen chamber.

HeLa Kyoto cells expressing keratin-19-rsEGFP(N205S)

Wild-type HeLa Kyoto cells were grown in DMEM (Life Technologies, Carlsbad, CA) containing phenol red, L-glutamine, and high glucose supplemented with 10% FBS and 1% sodium pyruvate. A stable cell line expressing keratin-19-rsEGFP(N205S) was established as described in the following. A total number of $4 \cdot 10^4$ cells were seeded in a well of a 24-well plate and grown for 24 hours. The cells were then transiently transfected with the construct pMD-tEosFP-N-keratin-19-rsEGFP(N205S) using FugeneHD (Promega GmbH, Mannheim, Germany) according to the manufacturer's guideline. The optimal DNA amount to transfection reagent volume ratio is found to be 1 µg to 3 µl. The transfected cells were selected by culturing them in the medium described above supplemented with geneticin selective antibiotic (G418 Sulfate, Life Technologies, Carlsbad, CA) at a final concentration of 1 mg/ml as selection medium. For sorting, the cells of a confluent 75 cm² flask were harvested and suspended in 4 ml of the selection medium and centrifuged for 5 minutes at 1000 rpm. The pellet was resuspended in 1 ml of PBS containing 3% BSA (sterile filtered) and seeded in a well of a 6-well plate with 2 ml of the selection medium. Subsequently, the cells were sorted by fluorescence-activated cell sorting (FACS) upon simultaneous illumination with 405 nm and 488 nm light. Only rsEGFP(N205S) positive cells were collected and grown in the selection medium. For the live-cell experiments with the RESOLFT-SPIM microscope demonstrated in section 3.5.3, a total number of 10^5 sorted cells were seeded on a round coverslip ($\varnothing = 5$ mm) in a well of a 24-well plate and grown for 24 hours. Three hours prior to imaging, the selection medium is exchanged by DMEM without phenol red (Life Technologies, Carlsbad, CA) containing HEPES to reduce unwanted background in the cells caused by phenol red uptake. Immediately before imaging, the coverslip was washed three times with PBS. The cells were imaged at room temperature in FluoroBrite DMEM medium (Life Technologies, Carlsbad, CA).

U2OS cells expressing NUP214-3x-rsEGFP(N205S)

U2OS cells were grown in McCoy's 5A (modified) medium (Life Technologies, Carlsbad, CA) containing phenol red, L-glutamine, high glucose, and

bacto-peptone supplemented with 1% FCS, 1% glutamine, 1% non-essential amino acids, and 1% penicillin streptomycin. For imaging, $4 \cdot 10^4$ cells were grown on a round coverslip ($\varnothing = 5$ mm) placed in a 24-well for 24 hours. Then, the cells were transiently transfected with the construct NUP214-3x-rsEGFP(N205S) and FugeneHD (Promega GmbH, Mannheim, Germany) according to the manufacturer's guidelines. The optimal DNA amount to transfection reagent volume ratio is found to be 0.5 μ g to 1.5 μ l. After an incubation time of 70-74 hours, the growth medium was exchanged by DMEM without phenol red (Life Technologies, Carlsbad, CA) containing HEPES to reduce unwanted background in the cells caused by phenol red uptake. Immediately before imaging, the coverslip was washed three times with PBS. The cells were imaged at room temperature in FluoroBrite DMEM medium (Life Technologies, Carlsbad, CA). In order to obtain the NUP214-3x-rsEGFP(N205S) construct, the DNA of the NUP214-gene was amplified per PCR from a pNUP214-EGFP plasmid and subcloned into a backbone that was obtained before by introducing a triple-rsEGFP(N205S) into a pmEGFP-N1 vector (kindly provided by Dr. Jan Ellenberg, EMBL).

A.3 HIV-1 enclosing rsEGFP2

HIV-1 particles filled with rsEGFP2 are highly suitable objects to characterize the RESOLFT-SPIM setup. Moreover, the long-term imaging capability of the setup was shown in a study of HIV-1 assembly at the plasma membrane of an infected cell. A sketch of the HIV-1 structure is shown in figure A.2 to illustrate the distribution of rsEGFP2 proteins in the mature virion together with the essential viral components.

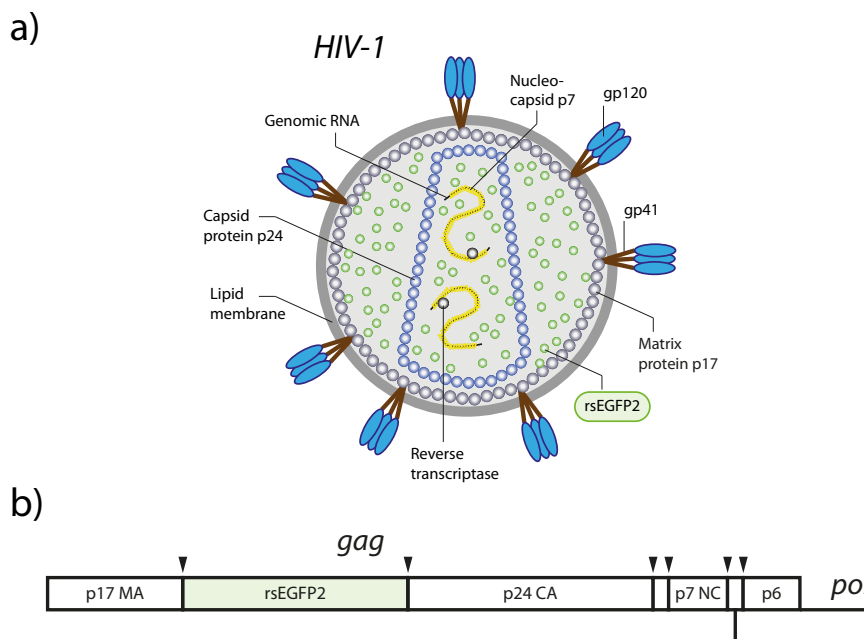


Figure A.2: Sketch of a HIV-1 particle and the Gag polyprotein. a) HIV-1 is composed of a lipid membrane containing glycoproteins (gp), a shell made of Matrix proteins located beneath the lipid bilayer and a cone-shaped Capsid core [16, 41, 106]. For the experiments described in this thesis, half of the Matrix proteins in the virion were tagged with rsEGFP2 by inserting the gene sequence of the RSFP in the sequence of the viral structural polyprotein Gag shown in b). Upon virus formation, Gag oligomerizes underneath the plasma membrane of an infected cell and a spherical Gag protein shell is formed. During maturation of the virus, Gag is cleaved at the sites marked with arrow heads. As a consequence, about 1000 rsEGFP2 proteins freely diffuse inside a mature single HIV-1 virion.

A.4 Imaging media for RESOLFT-SPIM

For RESOLFT-SPIM imaging, the specimen chamber is filled with optically transparent, water-based medium. Ideally, the medium contains components for cell growth and buffers the cells against changes in the pH. This buffering can, for example, be achieved by adding an organic buffer such as HEPES. Often, these media contain fluorescent components that can lead to background signals in the RESOLFT-SPIM image. Reducing the concentration of essential components may influence physiological processes in the specimen in long-term measurements. In order to find the optimal medium for RESOLFT-SPIM imaging, various media have been tested in the setup and evaluated in terms of their background noise. The results are shown in figure A.3. FluoroBrite containing HEPES offers moderate background noise and cell viability for several hours and is thus used for RESOLFT-SPIM imaging in this thesis.

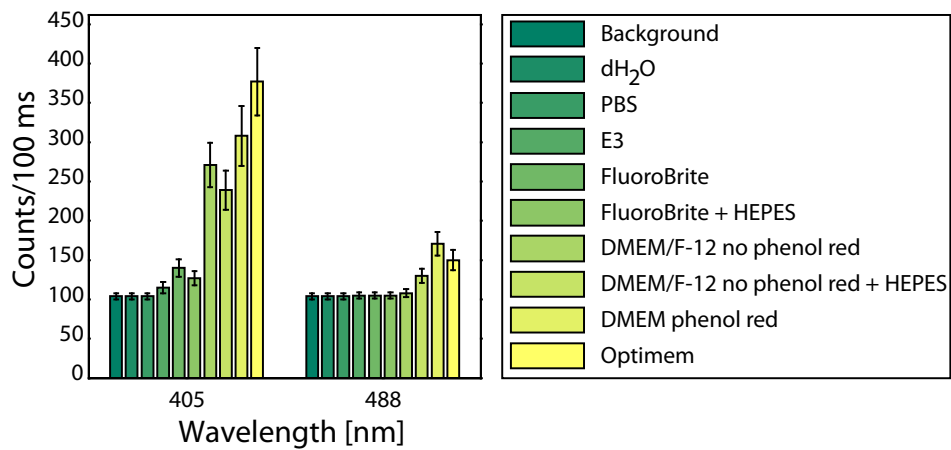


Figure A.3: Comparison of imaging media for RESOLFT-SPIM. The background signals generated by fluorescent components of various imaging media were measured in the RESOLFT-SPIM setup. The activation ($\lambda = 405$ nm) and readout ($\lambda = 488$ nm) light-sheets illuminate the medium filled specimen chamber with laser powers of 13.4 and 5.2 mW, respectively, measured in the back-focal plane of the 40x/0.8NA illumination objective. The plotted value is the number of counts per pixel and 100 ms exposure time, averaged over ten image frames and the full FOV of the camera.

Bibliography

- [1] E. Abbe. Beiträge zur Theorie des Mikroskops und der mikroskopischen Wahrnehmung. *Archiv für Mikroskopische Anatomie*, 9:413–468, 1873. (Cited on page 1.)
- [2] M. B. Ahrens, M. B. Orger, D. N. Robson, J. M. Li, and P. J. Keller. Whole-brain functional imaging at cellular resolution using light-sheet microscopy. *Nature Methods*, 10(5):413–420, 2013. (Cited on page 23.)
- [3] R. Ando, H. Hama, M. Yamamoto-Hino, H. Mizuno, and A. Miyawaki. An optical marker based on the UV-induced green-to-red photoconversion of a fluorescent protein. *Proceedings of the National Academy of Sciences of the United States of America*, 99:12651–12656, 2002. 20. (Cited on page 11.)
- [4] R. Ando, H. Mizuno, and A. Miyawaki. Regulated fast nucleocytoplasmic shuttling observed by reversible protein highlighting. *Science*, 306(5700):1370–1373, Nov. 2004. (Cited on page 11.)
- [5] M. Andresen, A. C. Stiel, J. Fölling, D. Wenzel, A. Schönle, A. Egner, C. Eggeling, S. W. Hell, and S. Jakobs. Photoswitchable fluorescent proteins enable monochromatic multilabel imaging and dual color fluorescence nanoscopy. *Nature biotechnology*, 26(9):1035–1040, Sept. 2008. (Cited on page 12.)
- [6] M. Andresen, A. C. Stiel, S. Trowitzsch, G. Weber, C. Eggeling, M. C. Wahl, S. W. Hell, and S. Jakobs. Structural basis for reversible photoswitching in Dronpa. *Proceedings of the National Academy of Sciences*, 104(32):13005–13009, Aug. 2007. (Cited on page 11.)
- [7] M. Andresen, M. C. Wahl, A. C. Stiel, F. Gräter, L. V. Schäfer, S. Trowitzsch, G. Weber, C. Eggeling, H. Grubmüller, S. W. Hell, and S. Jakobs. Structure and mechanism of the reversible photoswitch of a fluorescent protein. *Proceedings of the National Academy of Sciences of the United States of America*, 102(37):13070–13074, Sept. 2005. (Cited on page 11.)
- [8] D. Aquino, A. Schönle, C. Geisler, C. v. Middendorff, C. A. Wurm, Y. Okamura, T. Lang, S. W. Hell, and A. Egner. Two-color nanoscopy of three-dimensional volumes by 4pi detection of stochastically switched fluorophores. *Nature Methods*, 8(4):353–359, 2011. (Cited on page 35.)

- [9] E. A. Ash and G. Nicholls. Super-resolution aperture scanning microscope. *Nature*, 237(5357):510–512, June 1972. (Cited on page 1.)
- [10] K. Bahlmann, S. Jakobs, and S. W. Hell. 4Pi-confocal microscopy of live cells. *Ultramicroscopy*, 87(3):155–164, Apr. 2001. (Cited on page 35.)
- [11] M. Bates, B. Huang, G. T. Dempsey, and X. W. Zhuang. Multicolor super-resolution imaging with photo-switchable fluorescent probes. *Science*, 317:1749–1753, 2007. (Cited on page 2.)
- [12] K. Becker, N. Jährling, E. R. Kramer, F. Schnorrer, and H.-U. Dodt. Ultramicroscopy: 3D reconstruction of large microscopical specimens. *Journal of Biophotonics*, 1(1):36–42, Mar. 2008. (Cited on page 23.)
- [13] E. Betzig, G. H. Patterson, R. Sougrat, O. W. Lindwasser, S. Olenych, J. S. Bonifacino, M. W. Davidson, J. Lippincott-Schwartz, and H. F. Hess. Imaging intracellular fluorescent proteins at nanometer resolution. *Science*, 313(5793):1642–1645, Sept. 2006. (Cited on pages 2 and 28.)
- [14] G. Binnig, C. F. Quate, and C. Gerber. Atomic force microscope. *Physical Review Letters*, 56(9):930–933, Mar. 1986. (Cited on page 1.)
- [15] T. Brakemann, A. C. Stiel, G. Weber, M. Andresen, I. Testa, T. Grotjohann, M. Leutenegger, U. Plessmann, H. Urlaub, C. Eggeling, M. C. Wahl, S. W. Hell, and S. Jakobs. A reversibly photoswitchable GFP-like protein with fluorescence excitation decoupled from switching. *Nature Biotechnology*, 29(10):942–947, 2011. (Cited on pages 3 and 34.)
- [16] J. A. G. Briggs, K. Grünewald, B. Glass, F. Förster, H.-G. Kräusslich, and S. D. Fuller. The mechanism of HIV-1 core assembly: insights from three-dimensional reconstructions of authentic virions. *Structure (London, England: 1993)*, 14(1):15–20, Jan. 2006. (Cited on page 89.)
- [17] J. Capoulade, M. Wachsmuth, L. Hufnagel, and M. Knop. Quantitative fluorescence imaging of protein diffusion and interaction in living cells. *Nature Biotechnology*, 29(9):835–839, Sept. 2011. (Cited on pages 23 and 26.)
- [18] L.-A. Carlson, J. A. G. Briggs, B. Glass, J. D. Riches, M. N. Simon, M. C. Johnson, B. Müller, K. Grünewald, and H.-G. Kräusslich. Three-dimensional analysis of budding sites and released virus suggests a revised model for HIV-1 morphogenesis. *Cell Host & Microbe*, 4(6):592–599, Dec. 2008. (Cited on page 61.)
- [19] W. Chao, P. Fischer, T. Tyliczszak, S. Rekawa, E. Anderson, and P. Naulleau. Real space soft x-ray imaging at 10 nm spatial resolution. *Optics Express*, 20(9):9777–9783, Apr. 2012. (Cited on page 1.)

- [20] A. Chmyrov, J. Keller, T. Grotjohann, M. Ratz, E. d'Este, S. Jakobs, C. Eggeling, and S. W. Hell. Nanoscopy with more than 100,000 'doughnuts'. *Nature Methods*, July 2013. (Cited on pages 12, 35, and 83.)
- [21] J. Chojnacki, T. Staudt, B. Glass, P. Bingen, J. Engelhardt, M. Anders, J. Schneider, B. Müller, S. W. Hell, and H.-G. Kräusslich. Maturation-dependent HIV-1 surface protein redistribution revealed by fluorescence nanoscopy. *Science*, 338(6106):524–528, Oct. 2012. (Cited on page 34.)
- [22] D. M. Chudakov, V. V. Verkhusha, D. B. Staroverov, E. A. Souslova, S. Lukyanov, and K. A. Lukyanov. Photoswitchable cyan fluorescent protein for protein tracking. *Nature Biotechnology*, 22(11):1435–1439, Nov. 2004. (Cited on page 11.)
- [23] J.-A. Conchello and J. W. Lichtman. Optical sectioning microscopy. *Nature Methods*, 2(12):920–931, Dec. 2005. (Cited on page 17.)
- [24] R. N. Day and M. W. Davidson. The fluorescent protein palette: tools for cellular imaging. *Chemical Society Reviews*, 38(10):2887–2921, Oct. 2009. (Cited on page 10.)
- [25] W. Denk, J. H. Strickler, and W. W. Webb. 2-photon laser scanning fluorescence microscopy. *Science*, 248:73–76, 1990. (Cited on page 2.)
- [26] J. Durnin, J. H. Eberly, and J. J. Miceli. Comparison of bessel and gaussian beams. *Optics Letters*, 13(2):79–80, Feb. 1988. (Cited on page 26.)
- [27] J. Durnin, J. J. Miceli, and J. H. Eberly. Diffraction-free beams. *Physical Review Letters*, 58(15):1499–1501, Apr. 1987. (Cited on page 26.)
- [28] M. Dyba and S. W. Hell. Focal spots of size $\lambda/23$ open up far-field fluorescence microscopy at 33 nm axial resolution. *Physical Review Letters*, 88:163901, 2002. 16. (Cited on page 35.)
- [29] A. Egner and S. W. Hell. Fluorescence microscopy with super-resolved optical sections. *Trends in Cell Biology*, 15(4):207–215, Apr. 2005. (Cited on page 35.)
- [30] C. J. Engelbrecht and E. H. Stelzer. Resolution enhancement in a light-sheet-based microscope (SPIM). *Optics letters*, 31(10):1477–1479, May 2006. (Cited on pages 23 and 43.)
- [31] R. Erni, M. D. Rossell, C. Kisielowski, and U. Dahmen. Atomic-resolution imaging with a sub-50-pm electron probe. *Physical Review Letters*, 102(9):096101, Mar. 2009. (Cited on page 1.)

- [32] F. O. Fahrbach and A. Rohrbach. A line scanned light-sheet microscope with phase shaped self-reconstructing beams. *Optics Express*, 18(23):24229–24244, Nov. 2010. (Cited on page 26.)
- [33] F. O. Fahrbach, P. Simon, and A. Rohrbach. Microscopy with self-reconstructing beams. *Nature Photonics*, 4(11):780–785, 2010. (Cited on page 26.)
- [34] K. N. Fish. Total internal reflection fluorescence (TIRF) microscopy. In *Current Protocols in Cytometry*. John Wiley & Sons, Inc., 2001. (Cited on page 79.)
- [35] J. Fölling. *High-Resolution Microscopy with Photoswitchable Organic Markers*. PhD thesis, University of Göttingen, 2009. (Cited on page 32.)
- [36] J. Fölling, M. Bossi, H. Bock, R. Medda, C. A. Wurm, B. Hein, S. Jakobs, C. Eggeling, and S. W. Hell. Fluorescence nanoscopy by ground-state depletion and single-molecule return. *Nature Methods*, 5(11):943–945, 2008. (Cited on pages 2 and 28.)
- [37] C. Flors, J.-i. Hotta, H. Uji-i, P. Dedecker, R. Ando, H. Mizuno, A. Miyawaki, and J. Hofkens. A stroboscopic approach for fast photoactivation–localization microscopy with Dronpa mutants. *Journal of the American Chemical Society*, 129(45):13970–13977, Nov. 2007. (Cited on page 12.)
- [38] M. Friedrich, Q. Gan, V. Ermolayev, and G. S. Harms. STED-SpIM: Stimulated emission depletion improves sheet illumination microscopy resolution. *Biophysical Journal*, 100(8):L43–L45, Apr. 2011. (Cited on pages 35, 79, and 80.)
- [39] L. Gao, L. Shao, C. D. Higgins, J. S. Poulton, M. Peifer, M. W. Davidson, X. Wu, B. Goldstein, and E. Betzig. Noninvasive imaging beyond the diffraction limit of 3D dynamics in thickly fluorescent specimens. *Cell*, 151(6):1370–1385, Dec. 2012. (Cited on pages 26 and 79.)
- [40] V. Garcés-Chávez, D. McGloin, H. Melville, W. Sibbett, and K. Dholakia. Simultaneous micromanipulation in multiple planes using a self-reconstructing light beam. *Nature*, 419(6903):145–147, Sept. 2002. (Cited on page 26.)
- [41] T. Goto, M. Nakai, and K. Ikuta. The life-cycle of human immunodeficiency virus type 1. *Micron (Oxford, England: 1993)*, 29(2-3):123–138, June 1998. (Cited on page 89.)

- [42] K. Greger, J. Swoger, and E. H. K. Stelzer. Basic building units and properties of a fluorescence single plane illumination microscope. *The Review of scientific instruments*, 78(2):023705, Feb. 2007. (Cited on page 22.)
- [43] F. Görlitz, P. Hoyer, H. Falk, L. Kastrup, J. Engelhardt, and S. W. Hell. A sted microscope designed for routine biomedical applications. *Progress In Electromagnetics Research*, 147:57–68, 2014. (Cited on page 34.)
- [44] T. Grotjohann. *Generation of Novel Photochromic GFPs: Fluorescent Probes for RESOLFT-type Microscopy at Low Light Intensities*. PhD thesis, University of Göttingen, May 2012. (Cited on pages 11 and 12.)
- [45] T. Grotjohann, I. Testa, M. Leutenegger, H. Bock, N. T. Urban, F. Lavoie-Cardinal, K. I. Willig, C. Eggeling, S. Jakobs, and S. W. Hell. Diffraction-unlimited all-optical imaging and writing with a photochromic GFP. *Nature*, 478(7368):204–208, 2011. (Cited on pages 3, 12, and 34.)
- [46] T. Grotjohann, I. Testa, M. Reuss, T. Brakemann, C. Eggeling, S. W. Hell, and S. Jakobs. rsEGFP2 enables fast RESOLFT nanoscopy of living cells. *eLife*, 1, Dec. 2012. (Cited on pages 3, 12, 34, and 79.)
- [47] F. Göttfert, C. A. Wurm, V. Mueller, S. Berning, V. C. Cordes, A. Honigmann, and S. W. Hell. Coaligned dual-channel STED nanoscopy and molecular diffusion analysis at 20 nm resolution. *Biophysical Journal*, 105(1):L01–L03, July 2013. (Cited on page 34.)
- [48] M. Gu. *Advanced Optical Imaging Theory*. Springer, 1999. (Cited on page 17.)
- [49] N. G. Gurskaya, V. V. Verkhusha, A. S. Shcheglov, D. B. Staroverov, T. V. Chepurnykh, A. F. Fradkov, S. Lukyanov, and K. A. Lukyanov. Engineering of a monomeric green-to-red photoactivatable fluorescent protein induced by blue light. *Nature Biotechnology*, 24(4):461–465, Apr. 2006. (Cited on page 11.)
- [50] M. G. L. Gustafsson. Nonlinear structured-illumination microscopy: wide-field fluorescence imaging with theoretically unlimited resolution. *Proceedings of the National Academy of Sciences of the United States of America*, 102(37):13081–13086, Sept. 2005. (Cited on pages 28 and 34.)
- [51] M. G. L. Gustafsson, D. A. Agard, and J. W. Sedat. I5m: 3D widefield light microscopy with better than 100 nm axial resolution. *Journal of Microscopy*, 195:10–16, 1999. (Cited on page 35.)

- [52] M. G. L. Gustafsson, L. Shao, P. M. Carlton, C. J. R. Wang, I. N. Golubovskaya, W. Z. Cande, D. A. Agard, and J. W. Sedat. Three-dimensional resolution doubling in wide-field fluorescence microscopy by structured illumination. *Biophysical Journal*, 94:4957–4970, 2008. 12. (Cited on pages 26 and 35.)
- [53] S. Habuchi, R. Ando, P. Dedecker, W. Verheijen, H. Mizuno, A. Miyawaki, and J. Hofkens. Reversible single-molecule photo-switching in the GFP-like fluorescent protein Dronpa. *Proceedings of the National Academy of Sciences of the United States of America*, 102:9511–9516, 2005. 27. (Cited on page 11.)
- [54] B. Harke, J. Keller, C. K. Ullal, V. Westphal, A. Schönle, and S. W. Hell. Resolution scaling in STED microscopy. *Optics Express*, 16(6):4154–4162, Mar. 2008. (Cited on pages 2, 30, and 80.)
- [55] B. Harke, C. K. Ullal, J. Keller, and S. W. Hell. Three-dimensional nanoscopy of colloidal crystals. *Nano letters*, 8(5):1309–1313, May 2008. (Cited on page 35.)
- [56] M. Heilemann, S. van de Linde, M. Schuttpelz, R. Kasper, B. Seefeldt, A. Mukherjee, P. Tinnefeld, and M. Sauer. Subdiffraction-resolution fluorescence imaging with conventional fluorescent probes. *Angewandte Chemie (international Edition)*, 47:6172–6176, 2008. (Cited on pages 2 and 28.)
- [57] R. Heim, D. C. Prasher, and R. Y. Tsien. Wavelength mutations and posttranslational autoxidation of green fluorescent protein. *Proceedings of the National Academy of Sciences*, 91(26):12501–12504, 1994. (Cited on page 10.)
- [58] B. Hein, K. I. Willig, and S. W. Hell. Stimulated emission depletion (STED) nanoscopy of a fluorescent protein-labeled organelle inside a living cell. *Proceedings of the National Academy of Sciences*, 105(38):14271–14276, Sept. 2008. (Cited on page 35.)
- [59] R. Heintzmann, T. M. Jovin, and C. Cremer. Saturated patterned excitation microscopy - a concept for optical resolution improvement. *Optical Society of America. Journal A: Optics, Image Science, and Vision*, 19:1599–1609, 2002. 8. (Cited on pages 28 and 29.)
- [60] S. Hell. Increasing the resolution of far-field fluorescence light microscopy by point-spread-function engineering. In J. R. Lakowicz, editor, *Topics in Fluorescence Spectroscopy*, volume 5, pages 361–422. Plenum Press, New York, 1997. (Cited on page 35.)

- [61] S. Hell. Toward fluorescence nanoscopy. *Nature Biotechnology*, 21:1347–1355, 2003. 11. (Cited on pages 2, 27, 28, and 30.)
- [62] S. Hell, M. Schrader, and H. T. M. VanderVoort. Far-field fluorescence microscopy with three-dimensional resolution in the 100-nm range. *Journal of Microscopy*, 187:1–7, 1997. 1. (Cited on page 35.)
- [63] S. W. Hell. Far-field optical nanoscopy. *Science*, 316(5828):1153–1158, May 2007. (Cited on page 27.)
- [64] S. W. Hell. Microscopy and its focal switch. *Nature Methods*, 6(1):24–32, 2009. (Cited on pages 2, 27, and 30.)
- [65] S. W. Hell, M. Dyba, and S. Jakobs. Concepts for nanoscale resolution in fluorescence microscopy. *Current opinion in neurobiology*, 14(5):599–609, 2004. (Cited on pages 27 and 30.)
- [66] S. W. Hell, S. Jakobs, and L. Kastrup. Imaging and writing at the nanoscale with focused visible light through saturable optical transitions. *Applied Physics A: Materials Science & Processing*, 77(7):859–860, 2003. (Cited on pages 28 and 30.)
- [67] S. W. Hell and M. Kroug. Ground-state-depletion fluorescence microscopy: A concept for breaking the diffraction resolution limit. *Applied Physics B: Lasers and Optics*, 60(5):495–497, 1995. (Cited on page 29.)
- [68] S. W. Hell and J. Wichmann. Breaking the diffraction resolution limit by stimulated emission: stimulated-emission-depletion fluorescence microscopy. *Optics letters*, 19(11):780–782, 1994. (Cited on pages 2, 27, and 28.)
- [69] M. Hofmann. *RESOLFT-Microscopy with photoswitchable proteins*. PhD thesis, Ruperto-Carola University of Heidelberg, 2008. (Cited on page 33.)
- [70] M. Hofmann, C. Eggeling, S. Jakobs, and S. W. Hell. Breaking the diffraction barrier in fluorescence microscopy at low light intensities by using reversibly photoswitchable proteins. *Proceedings of the National Academy of Sciences of the United States of America*, 102(49):17565–17569, Dec. 2005. (Cited on pages 3, 28, and 29.)
- [71] P. Hoyer, T. Staudt, J. Engelhardt, and S. W. Hell. Quantum dot blueing and blinking enables fluorescence nanoscopy. *Nano Letters*, 11(1):245–250, Jan. 2011. (Cited on page 28.)

- [72] Y. S. Hu, M. Zimmerley, Y. Li, R. Watters, and H. Cang. Single-molecule super-resolution light-sheet microscopy. *ChemPhysChem*, 15(4):577–586, 2014. (Cited on page 19.)
- [73] B. Huang, H. Babcock, and X. Zhuang. Breaking the diffraction barrier: Super-resolution imaging of cells. *Cell*, 143(7):1047–1058, Dec. 2010. (Cited on page 28.)
- [74] B. Huang, W. Q. Wang, M. Bates, and X. W. Zhuang. Three-dimensional super-resolution imaging by stochastic optical reconstruction microscopy. *Science*, 319:810–813, 2008. (Cited on page 35.)
- [75] J. Huisken and D. Y. R. Stainier. Even fluorescence excitation by multi-directional selective plane illumination microscopy (mSPIM). *Optics letters*, 32(17):2608–2610, Sept. 2007. (Cited on page 23.)
- [76] J. Huisken and D. Y. R. Stainier. Selective plane illumination microscopy techniques in developmental biology. *Development*, 136(12):1963–1975, June 2009. (Cited on page 23.)
- [77] J. Huisken, J. Swoger, F. D. Bene, J. Wittbrodt, and E. H. K. Stelzer. Optical sectioning deep inside live embryos by selective plane illumination microscopy. *Science*, 305(5686):1007–1009, Aug. 2004. (Cited on pages 2, 10, 22, and 23.)
- [78] S. M. Hurlley and L. Helmuth. The future looks bright ... *Science*, 300(5616):75–75, Apr. 2003. (Cited on page 5.)
- [79] Invitrogen. Fluorescence-SpectraViewer, 2013. (Cited on page 8.)
- [80] S. Ivanchenko, W. J. Godinez, M. Lampe, H.-G. Kräusslich, R. Eils, K. Rohr, C. Bräuchle, B. Müller, and D. C. Lamb. Dynamics of HIV-1 assembly and release. *PLoS Pathogens*, 5(11):e1000652, Nov. 2009. (Cited on page 70.)
- [81] N. Jährling, K. Becker, and H.-U. Dodt. 3D-reconstruction of blood vessels by ultramicroscopy. *Organogenesis*, 5(4):227–230, 2009. (Cited on page 23.)
- [82] M. F. Juetten, T. J. Gould, M. D. Lessard, M. J. Mlodzianoski, B. S. Nagpure, B. T. Bennett, S. T. Hess, and J. Bewersdorf. Three-dimensional sub-100 nm resolution fluorescence microscopy of thick samples. *Nature Methods*, 5:527–529, 2008. 6. (Cited on page 35.)
- [83] H. P. Kao and A. S. Verkman. Tracking of single fluorescent particles in 3 dimensions - use of cylindrical optics to encode particle position. *Biophysical Journal*, 67:1291–1300, 1994. 3. (Cited on page 35.)

- [84] J. Keller. *Optimal de-excitation patterns for RESOLFT-Microscopy*. PhD thesis, Ruperto-Carola University of Heidelberg, 2007. (Cited on page 29.)
- [85] J. Keller, A. Schönle, and S. W. Hell. Efficient fluorescence inhibition patterns for RESOLFT microscopy. *Optics Express*, 15(6):3361–3371, Mar. 2007. (Cited on page 29.)
- [86] P. J. Keller. In vivo imaging of zebrafish embryogenesis. *Methods*, 62(3):268–278, Aug. 2013. (Cited on page 23.)
- [87] P. J. Keller, F. Pampaloni, G. Lattanzi, and E. H. Stelzer. Three-dimensional microtubule behavior in xenopus egg extracts reveals four dynamic states and state-dependent elastic properties. *Biophysical Journal*, 95(3):1474–1486, Aug. 2008. (Cited on page 23.)
- [88] P. J. Keller, A. D. Schmidt, A. Santella, K. Khairy, Z. Bao, J. Wittbrodt, and E. H. K. Stelzer. Fast, high-contrast imaging of animal development with scanned light sheet-based structured-illumination microscopy. *Nature Methods*, 7(8):637–642, 2010. (Cited on page 2.)
- [89] P. J. Keller, A. D. Schmidt, J. Wittbrodt, and E. H. K. Stelzer. Reconstruction of zebrafish early embryonic development by scanned light sheet microscopy. *Science*, 322(5904):1065–1069, Nov. 2008. (Cited on pages 2, 19, and 23.)
- [90] P. J. Keller and E. H. K. Stelzer. Quantitative in vivo imaging of entire embryos with digital scanned laser light sheet fluorescence microscopy. *Current opinion in neurobiology*, 18(6):624–632, Dec. 2008. (Cited on pages 21 and 22.)
- [91] A. Khodjakov and C. L. Rieder. Imaging the division process in living tissue culture cells. *Methods (San Diego, Calif.)*, 38(1):2–16, Jan. 2006. (Cited on page 8.)
- [92] P. Kirkpatrick and A. V. Baez. Formation of optical images by x-rays. *Journal of the Optical Society of America*, 38(9):766–773, Sept. 1948. (Cited on page 1.)
- [93] T. A. Klar and S. W. Hell. Subdiffraction resolution in far-field fluorescence microscopy. *Optics letters*, 24(14):954–956, 1999. (Cited on pages 2 and 27.)
- [94] T. A. Klar, S. Jakobs, M. Dyba, A. Egner, and S. W. Hell. Fluorescence microscopy with diffraction resolution barrier broken by stimulated emission. *Proceedings of the National Academy of Sciences*, 97(15):8206–8210, July 2000. (Cited on page 35.)

- [95] M. Knoll and E. Ruska. Das elektronenmikroskop. *Zeitschrift fuer Physik*, 78:318–339, 1932. (Cited on page 1.)
- [96] K. Kolmakov, C. A. Wurm, R. Hennig, E. Rapp, S. Jakobs, V. N. Belov, and S. W. Hell. Red-emitting rhodamines with hydroxylated, sulfonated, and phosphorylated dye residues and their use in fluorescence nanoscopy. *Chemistry - A European Journal*, 18(41):12986–12998, Oct. 2012. (Cited on page 9.)
- [97] U. Krzic, S. Gunther, T. E. Saunders, S. J. Streichan, and L. Hufnagel. Multiview light-sheet microscope for rapid in toto imaging. *Nature Methods*, 9(7):730–733, 2012. (Cited on pages 21 and 23.)
- [98] S. M. Kurtz and J. N. Devine. PEEK biomaterials in trauma, orthopedic, and spinal implants. *Biomaterials*, 28(32):4845–4869, Nov. 2007. (Cited on page 45.)
- [99] F. Lavoie-Cardinal, N. A. Jensen, V. Westphal, A. C. Stiel, A. Chmyrov, J. Bierwagen, I. Testa, S. Jakobs, and S. W. Hell. Two-color RESOLFT nanoscopy with green and red fluorescent photochromic proteins. *ChemPhysChem*, 15(4):655–663, Mar. 2014. (Cited on pages 11, 12, 35, and 83.)
- [100] J. Lippincott-Schwartz and G. H. Patterson. Development and use of fluorescent protein markers in living cells. *Science*, 300(5616):87–91, Apr. 2003. (Cited on page 9.)
- [101] B. Liu, S. Fletcher, M. Avadisman, P. T. Gunning, and C. C. Gradinaru. A photostable, pH-invariant fluorescein derivative for single-molecule microscopy. *Journal of Fluorescence*, 19(5):915–920, Sept. 2009. (Cited on page 9.)
- [102] K. A. Lukyanov, D. M. Chudakov, S. Lukyanov, and V. V. Verkhusha. Innovation: Photoactivatable fluorescent proteins. *Nature Reviews. Molecular Cell Biology*, 6(11):885–891, Nov. 2005. (Cited on page 11.)
- [103] K. A. Lukyanov, A. F. Fradkov, N. G. Gurskaya, M. V. Matz, Y. A. Labas, A. P. Savitsky, M. L. Markelov, A. G. Zaraisky, X. Zhao, Y. Fang, W. Tan, and S. A. Lukyanov. Natural animal coloration can be determined by a nonfluorescent green fluorescent protein homolog. *The Journal of Biological Chemistry*, 275(34):25879–25882, Aug. 2000. (Cited on page 11.)
- [104] T. Maimon, N. Elad, I. Dahan, and O. Medalia. The human nuclear pore complex as revealed by cryo-electron tomography. *Structure*, 20(6):998–1006, June 2012. (Cited on page 72.)

- [105] Max Born and Emil Wolf. *Principles of Optics*. Cambridge University Press, 2005. (Cited on pages 14 and 17.)
- [106] M. D. Miller, C. M. Farnet, and F. D. Bushman. Human immunodeficiency virus type 1 preintegration complexes: studies of organization and composition. *Journal of Virology*, 71(7):5382–5390, July 1997. (Cited on page 89.)
- [107] R. Milo. What is the total number of protein molecules per cell volume? A call to rethink some published values. *BioEssays*, 35(12):1050–1055, Dec. 2013. (Cited on page 5.)
- [108] M. Minsky. Microscopy apparatus US patent, 1961. (Cited on pages 2 and 17.)
- [109] M. Ormö, A. B. Cubitt, K. Kallio, L. A. Gross, R. Y. Tsien, and S. J. Remington. Crystal structure of the aequorea victoria green fluorescent protein. *Science (New York, N.Y.)*, 273(5280):1392–1395, Sept. 1996. (Cited on page 10.)
- [110] G. H. Patterson, S. M. Knobel, W. D. Sharif, S. R. Kain, and D. W. Piston. Use of the green fluorescent protein and its mutants in quantitative fluorescence microscopy. *Biophysical Journal*, 73(5):2782–2790, Nov. 1997. (Cited on pages 10 and 12.)
- [111] G. H. Patterson and J. Lippincott-Schwartz. A photoactivatable GFP for selective photolabeling of proteins and cells. *Science*, 297:1873–1877, 2002. 5588. (Cited on page 11.)
- [112] S. R. P. Pavani, M. A. Thompson, J. S. Biteen, S. J. Lord, N. Liu, R. J. Twieg, R. Piestun, and W. E. Moerner. Three-dimensional, single-molecule fluorescence imaging beyond the diffraction limit by using a double-helix point spread function. *Proceedings of the National Academy of Sciences of the United States of America*, 106:2995–2999, 2009. 9. (Cited on page 35.)
- [113] J. B. Pawley. *Handbook of biological confocal microscopy*. Springer, New York, 2nd edition, 2006. (Cited on page 17.)
- [114] T. A. Planchon, L. Gao, D. E. Milkie, M. W. Davidson, J. A. Galbraith, C. G. Galbraith, and E. Betzig. Rapid three-dimensional isotropic imaging of living cells using bessel beam plane illumination. *Nature Methods*, 8(5):417–423, 2011. (Cited on pages 26 and 79.)
- [115] S. Preibisch, S. Saalfeld, J. Schindelin, and P. Tomancak. Software for bead-based registration of selective plane illumination microscopy data. *Nature Methods*, 7(6):418–419, June 2010. (Cited on page 21.)

- [116] S. Quirin, S. R. P. Pavani, and R. Piestun. Optimal 3D single-molecule localization for superresolution microscopy with aberrations and engineered point spread functions. *Proceedings of the National Academy of Sciences*, Dec. 2011. (Cited on page 28.)
- [117] L. Rayleigh. Wave theory of light. *Scientific Papers*, page 235, 1903. (Cited on page 16.)
- [118] E. H. Rego, L. Shao, J. J. Macklin, L. Winoto, G. A. Johansson, N. Kamps-Hughes, M. W. Davidson, and M. G. L. Gustafsson. Non-linear structured-illumination microscopy with a photoswitchable protein reveals cellular structures at 50-nm resolution. *Proceedings of the National Academy of Sciences*, 109(3):E135–E143, 2012. (Cited on page 34.)
- [119] M. Reuss. *Simpler STED setups*. PhD thesis, Ruperto-Carola University of Heidelberg, 2011. (Cited on page 35.)
- [120] E. G. Reynaud, U. Krzic, K. Greger, and E. H. Stelzer. Light sheet-based fluorescence microscopy: more dimensions, more photons, and less photodamage. *HFSP Journal*, 2(5):266–275, Oct. 2008. (Cited on page 21.)
- [121] M. J. Rust, M. Bates, and X. W. Zhuang. Sub-diffraction-limit imaging by stochastic optical reconstruction microscopy (STORM). *Nature Methods*, 3:793–795, 2006. (Cited on page 28.)
- [122] P. Schacht, S. B. Johnson, and P. A. Santi. Implementation of a continuous scanning procedure and a line scan camera for thin-sheet laser imaging microscopy. *Biomedical optics express*, 1(2):598–609, 2010. (Cited on page 21.)
- [123] P. J. Scherz, J. Huisken, P. Sahai-Hernandez, and D. Y. R. Stainier. High-speed imaging of developing heart valves reveals interplay of morphogenesis and function. *Development*, 135(6):1179–1187, Feb. 2008. (Cited on page 23.)
- [124] L. Schäfer, G. Groenhof, A. Klingen, G. Ullmann, M. Boggio-Pasqua, M. Robb, and H. Grubmüller. Photoswitching of the fluorescent protein asFP595: Mechanism, proton pathways, and absorption spectra. *Angewandte Chemie*, 119(4):536–542, Jan. 2007. (Cited on page 11.)
- [125] B. Schmid, G. Shah, N. Scherf, M. Weber, K. Thierbach, C. P. Campos, I. Roeder, P. Aanstad, and J. Huisken. High-speed panoramic light-sheet microscopy reveals global endodermal cell dynamics. *Nature Communications*, 4, July 2013. (Cited on page 23.)

- [126] R. Schmidt, C. A. Wurm, S. Jakobs, J. Engelhardt, A. Egner, and S. W. Hell. Spherical nanosized focal spot unravels the interior of cells. *Nature Methods*, 5(6):539–544, June 2008. (Cited on page 35.)
- [127] T. A. Schüttrigkeit, T. v. Feilitzsch, C. K. Kompa, K. A. Lukyanov, A. P. Savitsky, A. A. Voityuk, and M. E. Michel-Beyerle. Femtosecond study of light-induced fluorescence increase of the dark chromoprotein asFP595. *Chemical Physics*, 323(2-3):149–160, Apr. 2006. (Cited on page 11.)
- [128] M. A. Schwentker, H. Bock, M. Hofmann, S. Jakobs, J. Bewersdorf, C. Eggeling, and S. W. Hell. Wide-field subdiffraction RESOLFT microscopy using fluorescent protein photoswitching. *Microscopy research and technique*, 70(3):269–280, Mar. 2007. (Cited on page 34.)
- [129] R. F. Service. Three scientists bask in prize's fluorescent glow. *Science*, 322(5900):361, 2008. (Cited on page 10.)
- [130] N. C. Shaner, R. E. Campbell, P. A. Steinbach, B. N. G. Giepmans, A. E. Palmer, and R. Y. Tsien. Improved monomeric red, orange and yellow fluorescent proteins derived from *discosoma* sp red fluorescent protein. *Nature Biotechnology*, 22:1567–1572, 2004. 12. (Cited on page 10.)
- [131] N. C. Shaner, G. H. Patterson, and M. W. Davidson. Advances in fluorescent protein technology. *Journal of Cell Science*, 120(24):4247–4260, Dec. 2007. (Cited on page 10.)
- [132] C. J. R. Sheppard and H. J. Matthews. Imaging in high-aperture optical systems. *Journal of the Optical Society of America A*, 4(8):1354–1360, Aug. 1987. (Cited on page 15.)
- [133] O. Shimomura, F. H. Johnson, and Y. Saiga. Extraction, purification and properties of aequorin, a bioluminescent protein from the luminous hydromedusan, *aequorea*. *Journal of Cellular and Comparative Physiology*, 59(3):223–239, June 1962. (Cited on page 10.)
- [134] G. Shtengel, J. A. Galbraith, C. G. Galbraith, J. Lippincott-Schwartz, J. M. Gillette, S. Manley, R. Sougrat, C. M. Waterman, P. Kanchanawong, M. W. Davidson, R. D. Fetter, and H. F. Hess. Interferometric fluorescent super-resolution microscopy resolves 3D cellular ultrastructure. *Proceedings of the National Academy of Sciences of the United States of America*, 106:3125–3130, 2009. 9. (Cited on pages 28 and 35.)
- [135] H. Siedentopf and R. Zsigmondy. Über Sichtbarmachung und Größenbestimmung ultramikroskopischer Teilchen, mit besonderer Anwendung auf Goldrubingläser. *Annalen der Physik*, 315(1):1–39, 1902. (Cited on page 21.)

- [136] C. S. Smith, N. Joseph, B. Rieger, and K. A. Lidke. Fast, single-molecule localization that achieves theoretically minimum uncertainty. *Nature Methods*, 7(5):373–375, May 2010. (Cited on page 28.)
- [137] F. Stahnisch. „Die Photographie als Hilfsmittel mikroskopischer Forschung“? Joseph von Gerlach (1820–1896) und die frühen anatomischen Mikrophotographien. *Berichte zur Wissenschaftsgeschichte*, 28(2):135–150, June 2005. (Cited on page 9.)
- [138] O. V. Stepanenko, O. V. Stepanenko, I. M. Kuznetsova, V. V. Verkhusa, and K. K. Turoverov. Chapter four - beta-barrel scaffold of fluorescent proteins: Folding, stability and role in chromophore formation. In Kwang W. Jeon, editor, *International Review of Cell and Molecular Biology*, volume Volume 302, pages 221–278. Academic Press, 2013. (Cited on page 10.)
- [139] A. C. Stiel, M. Andresen, H. Bock, M. Hilbert, J. Schilde, A. Schönle, C. Eggeling, A. Egner, S. W. Hell, and S. Jakobs. Generation of monomeric reversibly switchable red fluorescent proteins for far-field fluorescence nanoscopy. *Biophysical Journal*, 95(6):2989–2997, Sept. 2008. (Cited on pages 11 and 12.)
- [140] A. C. Stiel, S. Trowitzsch, G. Weber, M. Andresen, C. Eggeling, S. W. Hell, S. Jakobs, and M. C. Wahl. 1.8 angstrom bright-state structure of the reversibly switchable fluorescent protein Dronpa guides the generation of fast switching variants. *Biochemical Journal*, 402:35–42, 2007. 1. (Cited on pages 11 and 34.)
- [141] J. Swoger, M. Muzzopappa, H. López-Schier, and J. Sharpe. 4d retrospective lineage tracing using SPIM for zebrafish organogenesis studies. *Journal of Biophotonics*, 4(1-2):122–134, Jan. 2011. (Cited on page 23.)
- [142] J. Swoger, F. Pampaloni, and E. H. K. Stelzer. Light-sheet-based fluorescence microscopy for three-dimensional imaging of biological samples. *Cold Spring Harbor protocols*, 2014(1), 2014. (Cited on page 21.)
- [143] J. Swoger, P. Verveer, K. Greger, J. Huisken, and E. H. K. Stelzer. Multi-view image fusion improves resolution in three-dimensional microscopy. *Optics express*, 15(13):8029–8042, June 2007. (Cited on page 23.)
- [144] A. Szymborska, A. de Marco, N. Daigle, V. C. Cordes, J. A. G. Briggs, and J. Ellenberg. Nuclear pore scaffold structure analyzed by super-resolution microscopy and particle averaging. *Science*, 341(6146):655–658, July 2013. (Cited on page 82.)

- [145] I. Testa, N. T. Urban, S. Jakobs, C. Eggeling, K. I. Willig, and S. W. Hell. Nanoscopy of living brain slices with low light levels. *Neuron*, 75(6):992–1000, Sept. 2012. (Cited on pages 3 and 34.)
- [146] R. E. Thompson, D. R. Larson, and W. W. Webb. Precise nanometer localization analysis for individual fluorescent probes. *Biophysical Journal*, 82(5):2775–2783, May 2002. (Cited on page 28.)
- [147] R. Tomer, K. Khairy, F. Amat, and P. J. Keller. Quantitative high-speed imaging of entire developing embryos with simultaneous multiview light-sheet microscopy. *Nature Methods*, 2012. (Cited on pages 21 and 23.)
- [148] R. Y. Tsien. The green fluorescent protein. *Annual review of biochemistry*, 67(1):509–544, 1998. (Cited on page 10.)
- [149] R. Y. Tsien, L. Ernst, and A. Waggoner. Fluorophores for confocal microscopy: Photophysics and photochemistry. In J. B. Pawley, editor, *Handbook of biological confocal microscopy*, pages 338–352. Springer, New York, 3 edition, 2006. (Cited on page 19.)
- [150] A. H. Voie, D. H. Burns, and F. A. Spelman. Orthogonal-plane fluorescence optical sectioning: three-dimensional imaging of macroscopic biological specimens. *Journal of microscopy*, 170(Pt 3):229–236, June 1993. (Cited on page 21.)
- [151] R. Welker, H. Hohenberg, U. Tessmer, C. Huckhagel, and H.-G. Krausslich. Biochemical and structural analysis of isolated mature cores of human immunodeficiency virus type 1. *Journal of Virology*, 74(3):1168–1177, Feb. 2000. (Cited on pages 61 and 79.)
- [152] V. Westphal and S. W. Hell. Nanoscale resolution in the focal plane of an optical microscope. *Physical Review Letters*, 94:143903, 2005. (Cited on page 30.)
- [153] D. Wildanger, R. Medda, L. Kastrup, and S. W. Hell. A compact STED microscope providing 3D nanoscale resolution. *Journal of Microscopy*, 236:35–43, 2009. (Cited on page 35.)
- [154] D. Wildanger, B. R. Patton, H. Schill, L. Marseglia, J. P. Hadden, S. Knauer, A. Schönle, J. G. Rarity, J. L. O’Brien, S. W. Hell, and J. M. Smith. Solid immersion facilitates fluorescence microscopy with nanometer resolution and sub-angstrom emitter localization. *Advanced Materials*, 2012. (Cited on page 34.)
- [155] Y. Wu, A. Ghitani, R. Christensen, A. Santella, Z. Du, G. Rondeau, Z. Bao, D. Colón-Ramos, and H. Shroff. Inverted selective plane illumination microscopy (iSPIM) enables coupled cell identity lineaging

- and neurodevelopmental imaging in *caenorhabditis elegans*. *Proceedings of the National Academy of Sciences*, 108(43):17708–17713, Oct. 2011. (Cited on page 23.)
- [156] C. A. Wurm, K. Kolmakov, F. Göttfert, H. Ta, M. Bossi, H. Schill, S. Berning, S. Jakobs, G. Donnert, V. N. Belov, and others. Novel red fluorophores with superior performance in STED microscopy. *Optical Nanoscopy*, 1(1):1–7, 2012. (Cited on page 9.)
- [157] K. Xu, H. P. Babcock, and X. Zhuang. Dual-objective STORM reveals three-dimensional filament organization in the actin cytoskeleton. *Nature Methods*, 9(2):185–188, Jan. 2012. (Cited on page 35.)
- [158] P. Zhang, P. M. Goodwin, and J. H. Werner. Fast, super resolution imaging via besel-beam stimulated emission depletion microscopy. *Optics Express*, 22(10):12398, May 2014. (Cited on page 36.)

Acknowledgments

I would like to take the opportunity to thank all the people who have contributed to this thesis in many different ways and made the last years an unforgettable experience for me:

First and foremost, I would like to thank my supervisor Prof. Dr. Stefan W. Hell for the opportunity to work in the very interesting and interdisciplinary field of optical nanoscopy and for the outstanding and highly motivating scientific environment. He continuously supported this work with fruitful ideas and good advice.

Many thanks to Prof. Dr. Wolfgang Petrich for agreeing to be the second referee of this thesis, and to PD Dr. Karsten Rippe for being a member of the Thesis Advisory Committee and helpful comments.

I am especially thankful to Dr. Johann Engelhardt for his expert knowledge in optics and electronics. He was a great source of help in every aspect and whenever needed.

I would like to express my very sincere gratitude to Dr. Lars Hufnagel at EMBL for introducing me to the principle of light-sheet microscopy and for hosting me in his laboratory during the collaboration. His continuous inspiring support has significantly contributed to the success of this work.

I am grateful to my collaboration partners Prof. Dr. Hans-Georg Kräusslich and Janina Hanne for providing me with HIV samples and Dr. Jan Ellenberg and Dr. Anna Szymborska for their support on the nuclear pore complex experiment. I thank all of them for helpful discussions.

I cannot find words to express my gratitude to Dr. Christina Besir, Dr. Jasmin Zahn, Dr. Tim Grotjohann, and Tatjana Schneidt for their patience, support and practical training on cell culture work.

I would like to thank the mechanical and electronic workshops at DKFZ and EMBL for manufacturing various components of the setup and their expert advice, as well as the Cell Sorting and Protein Expression and Purification facilities at EMBL.

I would like to thank Dr. Matthias Henrich, Dr. Lars Hufnagel, Dr. Tim Grotjo-

hann, and Dr. Johann Engelhardt for proofreading of this thesis.

My gratitude is also addressed to all my colleagues at MPI in Göttingen, especially Prof. Dr. Stefan Jakobs, Dr. Tim Grotjohann, and Dr. Ilaria Testa for their helpful advise on reversibly switchable fluorescent proteins.

Special gratitude is addressed to all my former and present colleagues at DKFZ and EMBL for creating an enjoyable atmosphere in and outside the lab, especially Marvin Albert, Balint Balasz, Fabian Bergermann, Dr. Christina Besir, Dr. Pit Bingen, Dr. Franziska Curdt, Dr. Lucia Durrieu, Melanie Feldmann, Dr. Joachim Fischer, Frederik Görlitz, Dr. Stefan Guenther, Janina Hanne, Dr. Matthias Henrich, Simon Herr, Dimitri Kromm, Dr. Uros Krzic, Jonas Marquard, Gustavo Quintas Glasner de Medeiros, Dr. Nils Norlin, Aldona Nowicka, Julia Peukes, Dr. Matthias Reuss, Dr. Jale Schneider, Dr. Petr Strnad, Dr. Jasmin Zahn.

I am deeply grateful to my girlfriend Natalie for her unbounded patience, love, and understanding throughout the entire project.

Finally, I would like to thank my parents and my sister for their unconditional support and encouragement at all times.